ABSTRACT

Title of dissertation: NUMERICAL SIMULATIONS OF
MAGNETOROTATIONAL TURBULENCE
IN THE LABORATORY

Wilson Andrew Tillotson, Doctor of Philosophy, 2007

Dissertation directed by: Professor William Dorland
Department of Physics

When threaded by a weak magnetic field, a differentially rotating electrically conducting fluid may exhibit the Magnetorotational Instability (MRI), a likely mechanism for enhanced angular momentum transport in accretion disks. In this thesis, we investigate the MRI and its role in the transition to magnetohydrodynamic turbulence in laboratory liquid metal flows. In addition to presenting a basic WKB local linear analysis, we use two independently developed, global, nonlinear codes to study the problem of MRI in cylindrical geometry. We verify both codes by demonstrating their ability to simulate well-known nonlinear fluid phenomena, such as the development of Taylor vortices in unstable viscous Taylor-Couette flow. In the presence of magnetic fields, we demonstrate that both codes reproduce the correct MRI stability threshold.

Our numerical simulations predict the nonlinear saturation amplitude of excited MRI modes for a range of P_m, and results indicate that in laboratory liquid metal investigations, these magnetic excitations saturate at a low level when compared to the background field strength. We address the characteristics of saturated MRI excitations, and investigate their susceptibility to secondary instabilities, such as tearing modes. Finally, we predict the phenomenology of MRI near threshold in realistic cylindrical liquid metal experiments, including the effects of adding a toroidal field in the presence of endcaps. We comment on how the tools created during this research can be used to aid in the design of future experiments to investigate this transition region to magnetic turbulence.

Numerical Simulations of Magnetorotational Turbulence in the Laboratory

by

Wilson Andrew Tillotson

Dissertation submitted to the Faculty of the Graduate School of the
University of Maryland, College Park in partial fulfillment
of the requirements for the degree of
Doctor of Philosophy
2007

Advisory Committee:

Professor William Dorland, Chair/Advisor
Professor Daniel P. Lathrop
Professor Jian-Guo Liu
Professor Chuan Sheng Liu
Professor Richard F. Ellis

Acknowledgements

Even though this PhD dissertation grants the title of "doctor" to only one person, it has involved the support of many people, to whom I owe a debt of sincere gratitude. First, I would like to say an enormous thanks to my advisor, Bill Dorland. I could not imagine having a better mentor. His constant enthusiasm for my topic, his encouragement of my work and, of course, his"cracking of the whip" always provided the motivation, the encouragement and, most importantly, the excitement to propel me forward. Even though his teaching and research schedules were incredible demands on his time, I never felt like I had to fight my way into his office. To the contrary - I always felt welcome and comfortable whenever I had even what must have been the most tedious questions. Besides being a source of inspiration, he has also been a good friend, and what I have learned from him goes well beyond the bounds of doing good research.

I would like to say a huge thank you to Tomoyo Tatsuno for developing an outstanding code, working with me to fit it to this problem, and for so patiently going through my thesis with a fine tooth comb to make sure I got it right. Many thanks to Dan Lathrop for helping me connect the world of computation to the world of experiment and for helping to make sure that the project made practical sense. Thanks to Adil Hassam and Yi-Min Huang for the many helpful discussions about MHD, computation, and figuring out what to keep and what to throw away.

And then there are all the other people who have made Maryland a very special place for me over all those years: Jonathan King, Brian Tighe, "Mike" Ng Sheung Wah, Jonathan Ozik, Joseph Crenshaw, Mike Ricci, the cats (Coo, Gio and Ji), and all the others that I know I will slap myself later for not having mentioned. For providing me with excellent distraction, special thanks to my bandmates: Tim McCaskey, Aaron Geller, and Luis Nasser. For her love, encouragement and support, thanks to my wife, Elisabeth, who I had the great fortune to meet in graduate school, and who managed to put up with me through its completion.

Finally, I would like to thank my parents, who have been constantly supportive through not just the various phases of my academic life, but at all points in between. This thesis is dedicated to them.

TABLE OF CONTENTS

LIST OF TABLES

LIST OF FIGURES

Chapter 1

Introduction

1.1 Astrophysical Context

A question of considerable interest in the astrophysical community involves the mechanism of angular momentum transport through accretion disks. Many astrophysical flows, such as those surrounding planetary nebulae, stellar accretion disks, compact X-ray objects, and galaxies, are nearly inviscid. For matter to accrete onto a central object, gravitational contraction has to beat the centrifugal barrier, but on a global scale, this requires a transfer rate of angular momentum from one fluid element to another that is orders of magnitude higher than hydrodynamic shear viscosity can provide [1]. However, if the disk were turbulent, the effective "eddy viscosity" caused by the interaction of turbulent eddies at various length scales could be the source of the required accretion rates [2].

If it is true, as has become the general consensus among astrophysicists, that these accretion disks are turbulent, the important question becomes, what drives the turbulence? If the gas is warm enough to become partially ionized, accretion disks become magnetohydrodynamic fluids. The pervasive weak magnetic fields in these partially ionized disks can cause a linear instability which can lead directly to fluid turbulence. This is known as the Magnetorotational Instability (MRI) [1].

The MRI was discovered in 1959 by Velikhov [3] and further explained by Chandrasekhar [4] in 1960, but the discovery was not applied to accretion flows until 1991 [1]. As a mechanism for transporting orbital angular momentum, the MRI has far-reaching astrophysical implications. Its influence most likely regulates the rate of accretion in a wide range of astrophysical objects. Described simply, the MRI is a linear instability triggered by threading a partially ionized differentially rotating system with a weak magnetic field, the effect of which is to couple neighboring

fluid elements via magnetic tension. On a global scale, the MRI is orders of magnitude more effective in transporting angular momentum than viscous dissipation, and it can lead directly to disk turbulence. It has no hydrodynamic analog. [1].

Four important dimensionless parameters characterize the MRI: the magnetic Prandtl number, $P_m = \nu/\eta$, Lundquist number, $S = B_0 L/[\eta(\rho\mu)^{1/2}]$, and the magnetic Reynolds number, $R_m = \Omega L^2/\eta$. Here, B_0 is the magnitude of the weak background magnetic field, L is a typical length scale in the system, Ω is a characteristic orbital angular frequency, ν is the fluid viscosity, and η is the resistivity. In an accretion disc, the Prandtl number can vary orders of magnitude, as it depends on temperature and particle density: $P_m \approx 10^{-5}T^4/n$. However, if we assume $T \approx 10^5$ K and $n \approx 10^{15}$ cm^{-3} (typical stellar accretion disk values), P_m is of order unity [5].

1.2 An introduction to MRI

1.2.1 An instructive analog

Balbus and Hawley [1] helped qualitatively characterize the MRI by investigating a physical system in which two equal point masses orbit a central object with an angular velocity profile of the form $\mathbf{v}(r) = r\Omega(r)\hat{\mathbf{e}}_\theta$, where $\Omega(r)$ is the rotational frequency of an object at a radius r. They are coupled by a massless spring with spring constant k. Let $\underline{\xi} = (\xi_r, \xi_\theta, 0)$ be the vector characterizing the separation of the masses. It is easiest to derive the equations of motion for ξ_r and ξ_θ in the rotating frame, M, defined by the axes $(\hat{r}, \hat{\theta})$. The origin of M will be defined as the physical location of the inner mass. Let the vector from the fixed frame (F) origin to the origin of the moving frame be $\underline{R}$ and the vector from the fixed frame origin to the outer mass be $\underline{\xi}_F$. This system is summarized in Figure 1.1.

$\ddot{\underline{\xi}}_M$, the acceleration of the displacement vector as measured in the rotating frame is given by:

$$\ddot{\underline{\xi}}_M = \ddot{\underline{\xi}}_F - \ddot{\underline{R}} - \underline{\Omega} \times (\underline{\Omega} \times \underline{\xi}_M) - 2\underline{\Omega} \times \dot{\underline{\xi}}_M - \dot{\underline{\Omega}} \times \underline{\xi}_M \tag{1.1}$$

The first term on the RHS of equation 1.1 represents the acceleration of the outer mass measured

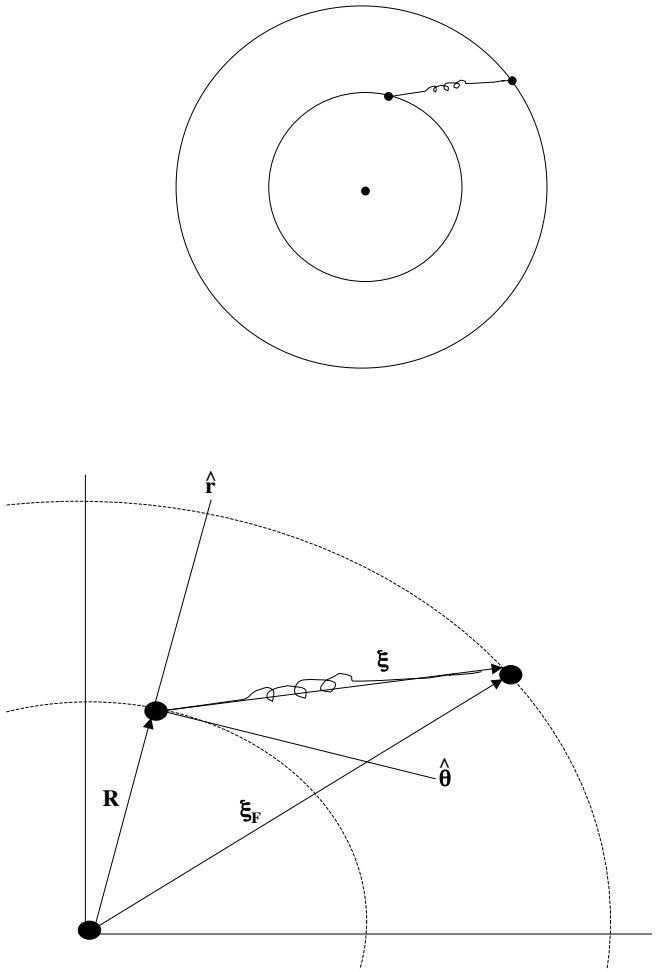

Figure 1.1: Simple physical analog of the magnetorotational instability: a runaway process in which angular momentum transferred between two fluid elements by a weak spring causes increased element separation, spring tension and angular momentum transport.

in the fixed frame. The second term is the acceleration of the rotating frame's origin with respect to the fixed frame origin. The third and fourth terms are accelerations due to the appearence of "effective" forces in the non-inertial rotating frame, specifically the centrifugal and Coriolis forces. The final term comes from the angular acceleration of the rotating frame itself. For a detailed derivation of equation 1.1, see [6], section 4-10.

$\ddot{\underline{\xi}}_F$ and $\ddot{\underline{R}}$ are quantified as follows:

$$m\ddot{\underline{\xi}}_F = -|F_g(r_2)|\hat{\xi}_F - \frac{1}{2}k\underline{\xi}_M \tag{1.2}$$

$$m\ddot{\underline{R}} = -|F_g(r_1)|\hat{r} + \frac{1}{2}k\underline{\xi}_M \tag{1.3}$$

Where r_1 and r_2 are the radial coordinates of the inner and outer masses measured in the fixed frame and $F_g(r)$ is the central force due to, say, a gravitational potential. To simplify this, we make the observation that

$$\hat{\underline{\xi}}_F = \frac{\underline{\xi}_F}{\xi_F} = \frac{\underline{R} + \underline{\xi}_M}{r_2} = \frac{r_1 + \xi_r}{r_2}\hat{r} + \frac{\xi_\theta}{r_2}\hat{\theta} \approx \hat{r} + \frac{\xi_\theta}{r_1}\hat{\theta} \tag{1.4}$$

where $r_2 = \sqrt{(r_1 + \xi_r)^2 + \xi_\theta^2}$, and the approximation is that $r_1 \approx r_2$ (radial separation is small compared to r_1). For a circular orbit, $|F_g(r)| = mr\Omega^2(r)$. For a Keplerian orbit, $\Omega(r) \propto 1/r^{3/2}$, but in general, we will leave this profile unspecified. Thus, equations 1.2 and 1.3 become:

$$\ddot{\underline{\xi}}_F = -r_2\Omega^2(r_2)\hat{\xi}_F - \frac{k}{2m}\underline{\xi}_M \tag{1.5}$$

$$\ddot{\underline{R}} = -r_1\Omega^2(r_1)\hat{r} + \frac{k}{2m}\underline{\xi}_M \tag{1.6}$$

Substituting into equation 1.1 and dropping the M subscripts:

$$\ddot{\underline{\xi}} = r_1\Omega^2(r_1)\hat{r} - r_2\Omega^2(r_2)\hat{\xi}_F - \frac{k}{m}\underline{\xi} + \Omega^2\underline{\xi} - (2\Omega\dot{\xi} - \dot{\Omega}\xi)(\hat{z} \times \hat{\xi}) \tag{1.7}$$

Now, we make the additional assumption that $\dot{\Omega} << \Omega^2$, which is reasonable for infinitesimal displacements ($\xi << R$). This allows us to drop the last term in the above equation which depends on $\dot{\Omega}$. We also make the following observation, which helps to simplify the first two terms

on the left hand side of equation 1.7:

$$r_1\Omega^2(r_1)\hat{r} - r_2\Omega^2(r_2)\hat{\xi}_F = \Big[r_1\Omega^2(r_1) - (r_1+\xi_r)\Omega^2(r_1+\xi_r)\Big]\hat{r} - r_2\Omega^2(r_2)\hat{\theta} \tag{1.8}$$

$$\approx -\frac{d(r\Omega^2)}{dr}\Big|_{r_1}\xi_r\hat{r} - r_1\Omega^2(r_1)\hat{\theta} = -(2\zeta+1)\Omega^2\xi_r\hat{r} - r_1\Omega^2(r_1)\hat{\theta} \tag{1.9}$$

where

$$\zeta \equiv \frac{r}{\Omega}\frac{d\Omega}{dr} \tag{1.10}$$

Equation 1.7 then reduces to the following equations of motion for the components of $\underline{\xi}$:

$$\ddot{\xi}_r - 2\Omega\dot{\xi}_\theta = -(2\Omega^2\zeta + \frac{k}{m})\xi_r \tag{1.11}$$

$$\ddot{\xi}_\theta + 2\Omega\dot{\xi}_r = -\frac{k}{m}\xi_\theta \tag{1.12}$$

If $\zeta < 0$ and the spring constant is weak ($k/m < -2\Omega^2\zeta$), then the system goes unstable (RHS of equation 1.11 is positive). For this to be true, note that ζ must be negative, but this is not at all uncommon in astrophysical disks; for example, a laminar Keplerian disk has a constant $\zeta = -3/2$ (see section 4.1).

The physical picture of the weak spring destabilizing the 2-mass system can be qualitatively understood as follows (see figure 1.1). The spring exerts a tension force on both masses, transferring angular momentum from the inner element to the outer. This causes the inner element to fall into a smaller, faster moving orbit, while the outer is forced into a higher, slower moving orbit (Note: this is contingent on the angular momentum increasing as a function of radius - we will address this issue in section 4.2). The instability arises as element separation increases, causing increased spring tension and outwardly directed angular momentum transport.

1.2.2 MHD version

The similarity of the spring system described above to a magnetized disk can be understood as follows. Imagine looking at a accretion disk from the side, as in figure 1.2. A uniform background

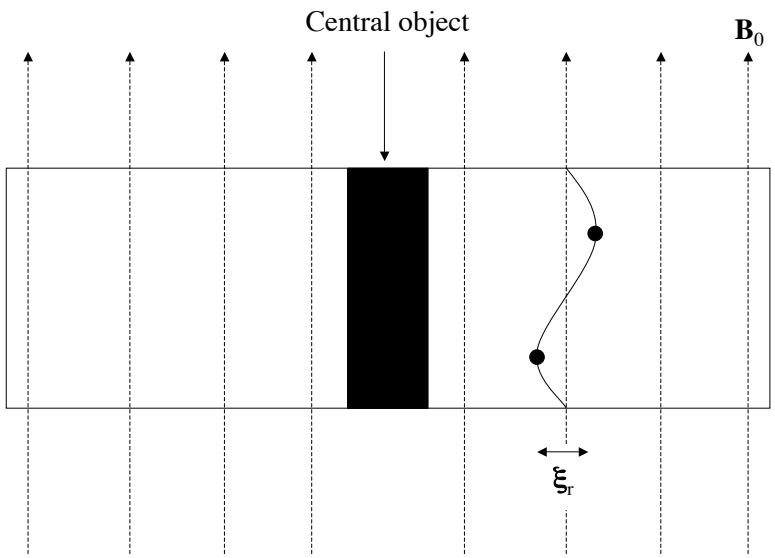

Figure 1.2: Cartoon side view of a accretion disk. A uniform background field of magnitude B_0 is oriented axially. If two fluid elements are located along a field line that is sinusoidally perturbed, then the tension in the field line exerts a restoring force on the fluid elements.

field of magnitude B_0 is oriented axially. If two fluid elements are located along a field line that is sinusoidally perturbed, then the tension in the field line exerts a restoring force on the fluid elements. The frequency associated with this restoring force is $(\mathbf{k} \cdot \mathbf{V}_A)$, where k is the vertical wavenumber of the perturbation and $V_A = B_0/\sqrt{\mu_0 \rho}$ is the Alfvén velocity associated with the magnetic field. Consequently, the analysis of the previous section can be used here with $(\mathbf{k} \cdot \mathbf{V}_A)^2$ substituted for k/m.

Equations 1.11 and 1.12 then become

$$\ddot{\xi}_r - 2\Omega\dot{\xi}_\theta = -(2\Omega^2\zeta + k^2 V_A^2)\xi_r \tag{1.13}$$

$$\ddot{\xi}_\theta + 2\Omega\dot{\xi}_r = -k^2 V_A^2 \xi_\theta \tag{1.14}$$

These are exactly the equations that Velikhov [3] and Balbus and Hawley [1] obtained by analyzing

an incompressible, axisymmetric, inviscid ($\nu = 0$), non-diffusive ($\eta = 0$) disk permeated by a weak axially oriented background field. A more detailed analysis of MRI in this context will be examined in the next chapter.

1.3 Laboratory context

The idea of observing the MRI in a laboratory setting was largely pioneered by Hantao Ji and Jeremy Goodman at Princeton University [7]. Significant advances have been made in observing MRI (see [8], [9], [10], [11]), but a completely convincing observation is difficult to achieve.

It is the magnetic Prandtl number that makes the MRI so difficult to observe in a laboratory setting. In an accretion disk, P_m is of order unity, while in a typical liquid metal with high magnetic resistivity, such as Sodium or Gallium, P_m is of order 10^{-5} or 10^{-6}. Classical MRI sets in typically around $R_m = 100$ [12], which would not necessarily be a problem, except for the low viscosity of liquid metals. Even at modest rotation rates in a liquid metal Couette flow experiment (for liquid sodium and an inner radius of 10 cm, the required rotation rate is around 8 Hz), the ratio of the rotation frequency to the viscous damping frequency, quantified by the hydrodynamic Reynolds number, $Re = \Omega L^2/\nu = R_m/P_m$, can be of order 10^7 to 10^8 if MRI is to be observed. This represents an enormous separation in timescales, and at these rotation rates, one cannot expect to have the laminar base state typically assumed in analytical calculations. (We will see in Chapters 3 and 5 that it is also this separation of timescales that makes laboratory MRI difficult to simulate numerically). For example, in a cylindrical Couette flow experiment, stationary endcaps will drive Ekman circulation, which disrupts the required laminar base state for MRI onset (see Figure 1.3, showing simulation results of Ekman circulation generated by the FD code, to be described in Chapter 5). This effect has been described in [13] and [14].

Despite these difficulties, an experiment conducted by Dan Sisan (UMD), *et al* involving the flow of liquid sodium between differentially rotating concentric spheres in the presence of an axially oriented background magnetic field shows strong evidence of the MRI. See Figure 1.4 for a depiction of the experimental apparatus.

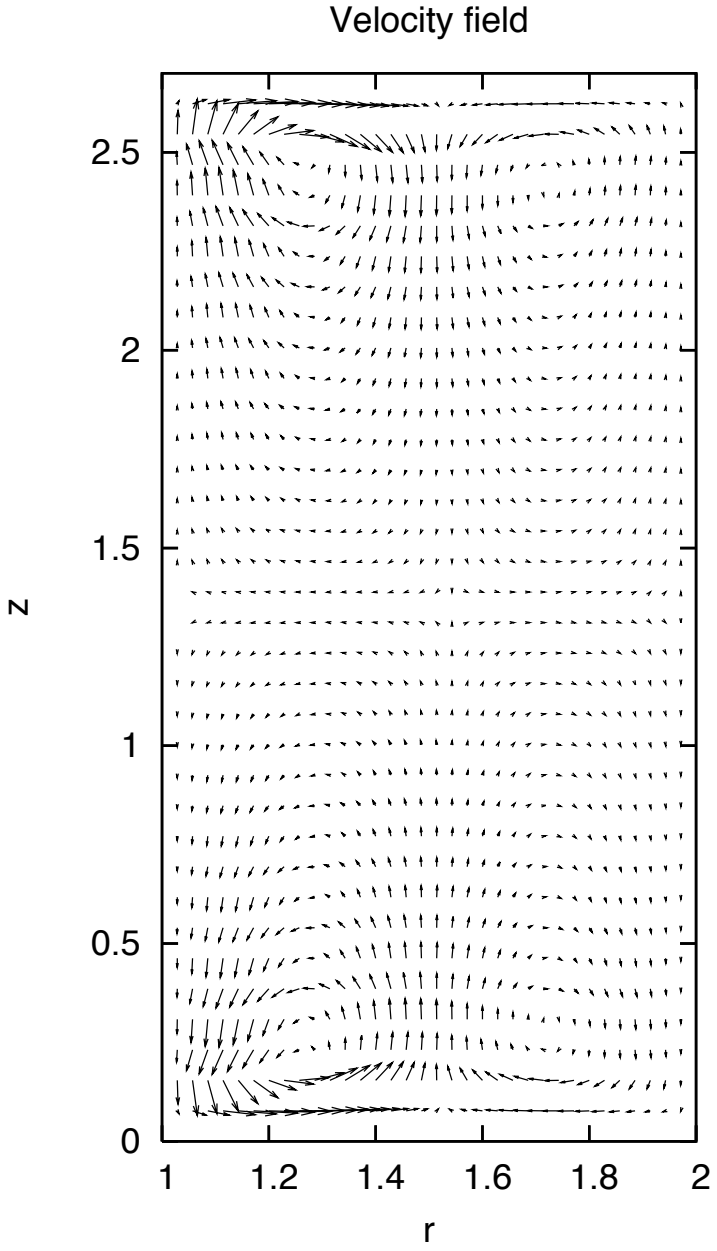

Figure 1.3: Ekman circulation disrupting the equilibrium flow profile near the endcaps.

To determine the hydrodynamic characteristics of the base state (no applied field) in this experiment, ultrasound velocimetry measurements were made on the sodium. Figure 1.6 shows the base background rotational profile, $\Omega(r)$ plotted against r. The condition on this radial profile for potential MRI instability is simply that it decrease with radius, $d\Omega/dr < 0$ (see section 1.1).

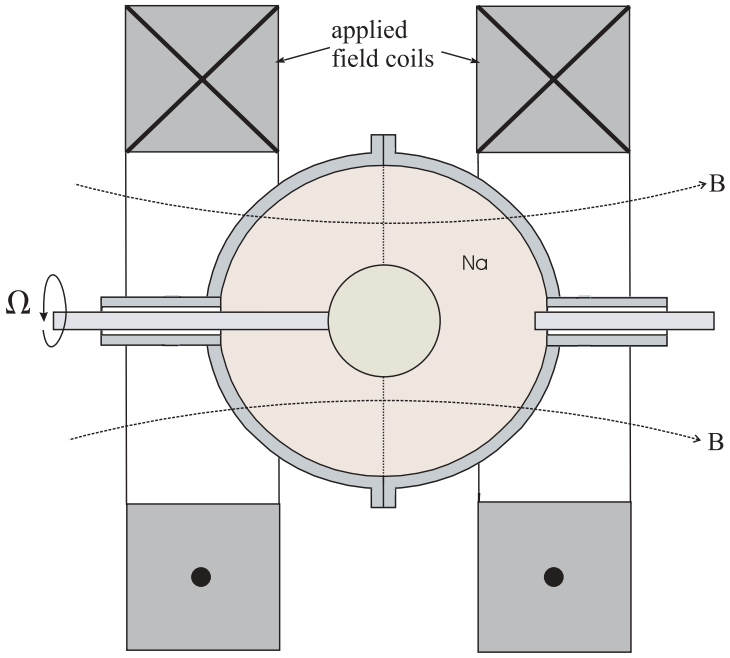

Figure 1.4: Experimental apparatus to study the flow of liquid sodium between differentially rotating concentric spheres (radii a and b in the presence of an axially oriented background magnetic field, B_0).

The condition for hydrodynamic Rayleigh stability is that the angular momentum must increase with radius, $d(r^2\Omega)/dr > 0$ (see Chapter 4 for complete details). Plotted in the inset of Figure 1.6 is the stability criteria for MRI (left axis). The bulk of the fluid is potentially MRI *unstable* and centrifugally *stable*, with the possible exception of boundary layer effects close to the surface of the spheres. Consequently, while the background velocity profile is not laminar, the *time averaged* background flow profile is ideal for MRI ($\Omega(r) \propto r^{-3/2}$).

Since the time averaged velocity profile is laminar, observing MRI fluctuations becomes more likely, since the growth rate of MRI is slow compared to the short timescale of the fluid turbulence. In other words, MRI is slow and big compared to the small scale hydrodynamic fluctuations. We will see more explicit evidence of this in Chapter 2, when we discuss MRI growth rates.

When an external magnetic field was applied to the sodium, beyond a certain threshold, small magnetic fluctuations were amplified. Accompanying this onset of magnetic field amplifi-

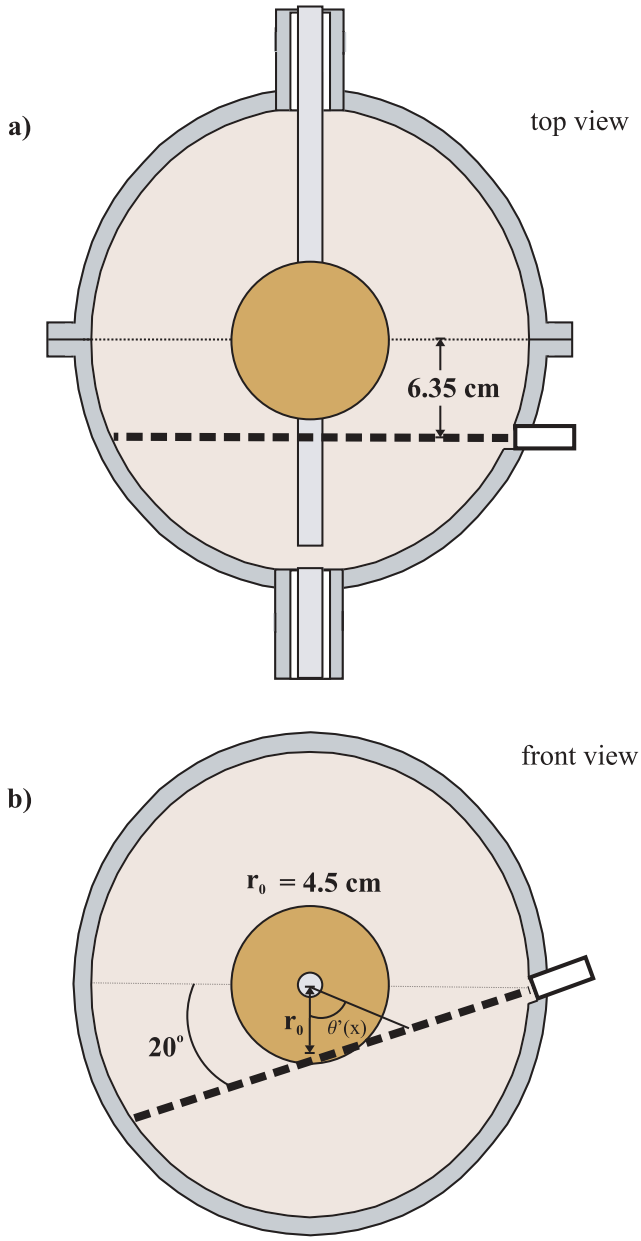

Figure 1.5: Ultrasound velocity measurements were taken along a single chord just outside the tangent cylinder in the apparatus, shown above.

cation was an increased torque of the fluid on the outer sphere, indicating an outward transport of angular momentum, consistent with the predictions of MRI (see figure 1.7). Finally, a map of the boundaries of these fluctuation onsets in the Ω, B_0 plane agrees with the local linear stability boundaries of MRI (see Chapter 2). All of this indicates that this field amplification could be a

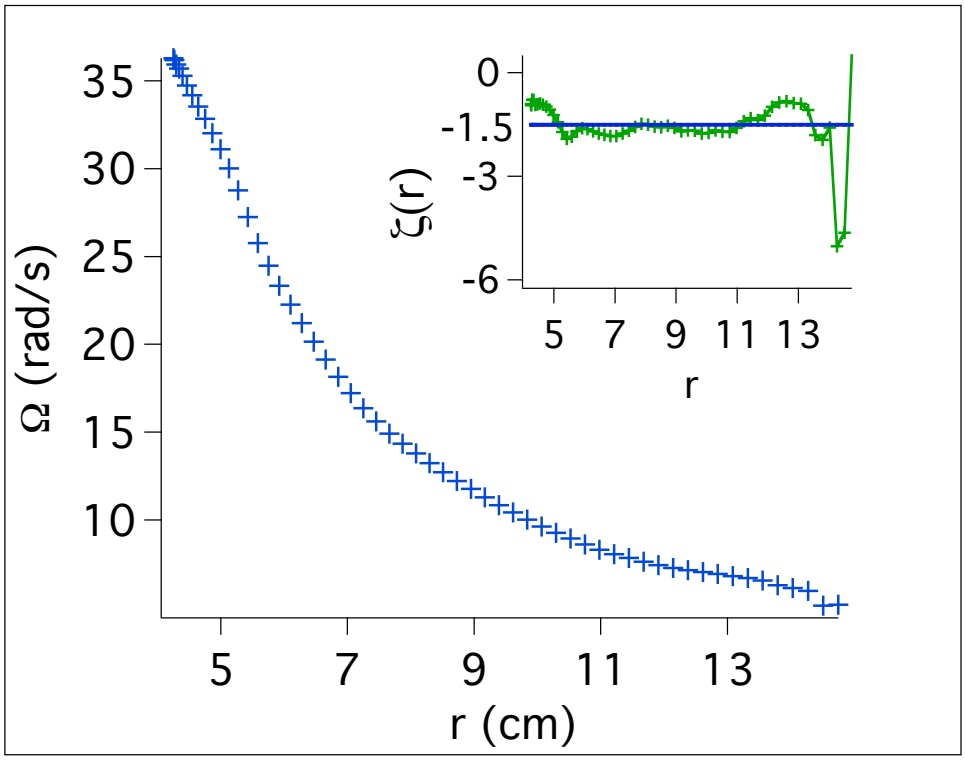

Figure 1.6: Experimentally measured radial profile, $\Omega(r)$. Inset left axis: MRI stability condition. Inset right axis: Rayleigh stability condition, ξ. An interesting aspect of this plot is that the average value of $\frac{d\log\Omega}{d\log r}$ is $-1.51 \simeq -\frac{3}{2}$, a feature true of a typical Keplerian profile.

result of the MRI.

Despite this agreement with the local theory, the experiment raises a number of interesting questions. For example, there are unexpected symmetries, in that the first excitation observed in the sphere is non-axisymmetric, in contrast to analytical predictions and analogous cylindrical perturbations. The observations in the experiment are of strictly nonlinear phenomena, despite MRI being a fundamentally linear instability (For 15 Hz rotation inner sphere rotation rate, the linear phase of the instability passes in less than a second). The instability arises from a turbulent base state, the excitations saturate at a relatively low level, and the observed patterns are not very turbulent. There is some evidence that the sharp boundary layers in the experiment have profound effects on the flow profile over the course of the experiment, although it not well understood what these effects are. Some of these questions can be addressed, but all of this necessitates nonlinear theory/simulations in addition to a comprehensive understanding of the linear MRI physics.

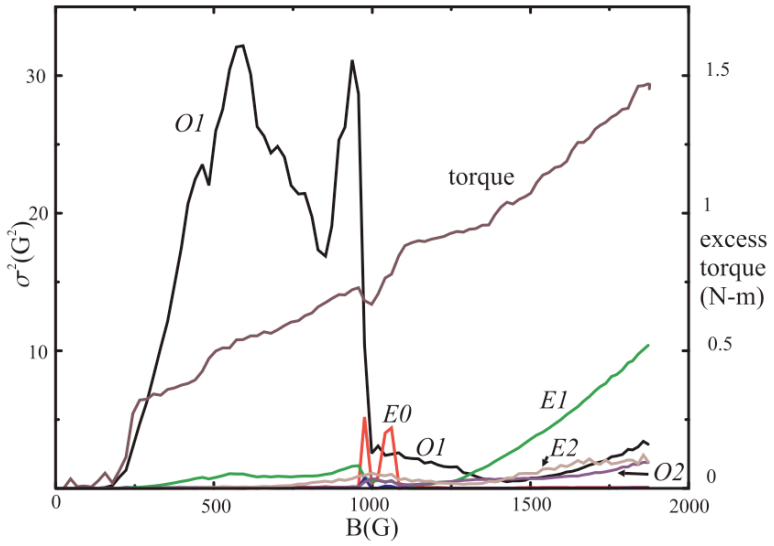

Figure 1.7: Accompanying the onset of magnetic field amplification (O1 representing the coefficient of amplification of the mode observed to be excited by the weakest background field) is an increased torque of the fluid on the outer sphere, indicating an outward transport of angular momentum, consistent with the predictions of MRI.

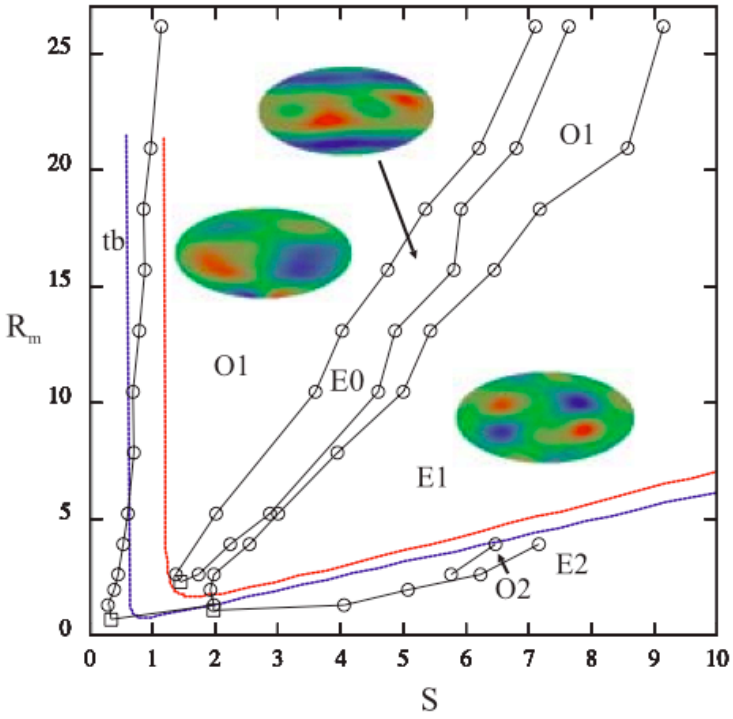

Figure 1.8: Marginal stability curves in both an analytic WKB approximation (solid) and an experiment involving liquid sodium flowing between concentric, differentially rotating spheres (markers).

Chapter 2

MRI Physics

2.1 Dispersion Relation - Local Linear Analysis

Let us consider more carefully the resistive, incompressible ($\nabla \cdot \mathbf{v} = 0$ and $\nabla \cdot \mathbf{B} = 0$) MHD equations:

$$\frac{\partial \mathbf{B}}{\partial t} + \mathbf{v} \cdot \nabla \mathbf{B} - \mathbf{B} \cdot \nabla \mathbf{v} = \eta \nabla^2 \mathbf{B} \tag{2.1}$$

$$\frac{\partial \mathbf{v}}{\partial t} + \mathbf{v} \cdot \nabla \mathbf{v} + \frac{1}{\rho} \nabla P - \frac{\mathbf{B} \cdot \nabla \mathbf{B}}{\mu_0 \rho} = \nu \nabla^2 \mathbf{v} \tag{2.2}$$

We wish to determine the evolution of perturbations under the influence of equations 2.1 and 2.2 in cylindrical curvilinear coordinates (r, θ, z). For now, the background magnetic field is only allowed to have an axial component (in Chapter 6 we will discuss the effects of a toroidal component), and the background velocity field is purely azimuthal with an as yet undetermined radial structure, $\Omega(r)$:

$$\mathbf{B} = B_0 \mathbf{e}_z + \delta \mathbf{B}, \quad \mathbf{v} = r\Omega(r) \mathbf{e}_\theta + \delta \mathbf{v} \tag{2.3}$$

Here r_0 is some characteristic radius, which we will further specify later in the section. We wish to perturb equations 2.1 and 2.2 about this background state. Writing out each equation explicitly component by component and dropping terms nonlinear in the perturbation amplitudes, we arrive

at the following set of coupled equations:

$$\delta\dot{B}_r - B_0\partial_z\delta v_r = \eta[\partial_r\partial_r^\dagger + \partial_z^2]\delta B_r \tag{2.4}$$

$$\delta\dot{B}_\theta - \delta B_r(r\Omega') - B_0\partial_z\delta v_\theta = \eta[\partial_r\partial_r^\dagger + \partial_z^2]\delta B_\theta \tag{2.5}$$

$$\delta\dot{B}_z - B_0\partial_z\delta v_z = \eta[\partial_r^\dagger\partial_r + \partial_z^2]\delta B_z \tag{2.6}$$

$$\delta\dot{v}_r + \partial_r\frac{\delta P}{\rho} - 2\Omega\delta v_\theta - \frac{B_0}{\mu_0\rho}\partial_z\delta B_r = \nu[\partial_r\partial_r^\dagger + \partial_z^2]\delta v_r \tag{2.7}$$

$$\delta\dot{v}_\theta + \delta v_r\partial_r^\dagger(r\Omega) - \frac{1}{\mu_0\rho}B_0\partial_z\delta B_\theta = \nu[\partial_r\partial_r^\dagger + \partial_z^2]\delta v_\theta \tag{2.8}$$

$$\delta\dot{v}_z - \frac{1}{\mu_0\rho}B_0\partial_z\delta B_z + \partial_z\frac{\delta P}{\rho} = \nu[\partial_r^\dagger\partial_r + \partial_z]\delta v_z \tag{2.9}$$

$$\partial_r^\dagger\delta B_r + \partial_z\delta B_z = 0 \tag{2.10}$$

$$\partial_r^\dagger\delta v_r + \partial_z\delta v_z = 0 \tag{2.11}$$

Here, $\partial_r^\dagger = \partial_r + \frac{1}{r}$. Equations 2.10 and 2.11 are the additional constraints imposed by divergence free magnetic and velocity fields. We will consider axisymmetric ($m = 0$) perturbations to these equations with periodic z dependence, in much the same way as the method introduced by Goodman and Ji [7]:

$$\delta V_{Ar} = \beta_r(r)\cos(kz)e^{\gamma t}, \quad \delta v_r = \varphi_r(r)\sin(kz)e^{\gamma t} \tag{2.12}$$

$$\delta V_{A\theta} = \beta_\theta(r)\cos(kz)e^{\gamma t}, \quad \delta v_\theta = \varphi_\theta(r)\sin(kz)e^{\gamma t} \tag{2.13}$$

$$\delta V_{Az} = \beta_z(r)\sin(kz)e^{\gamma t}, \quad \delta v_r = \varphi_z(r)\cos(kz)e^{\gamma t} \tag{2.14}$$

where $\delta V_A = \frac{\delta B}{\sqrt{\mu_0\rho}}$. Eliminating pressure via the divergence-free conditions reduces equations 2.4 - 2.11 to the following form:

$$\begin{pmatrix} \gamma - \eta D^2 & 0 & -\omega_A & 0 \\ -\zeta\Omega & \gamma - \eta D^2 & 0 & -\omega_A \\ (2 + \frac{D^2}{k^2})\omega_A & 0 & \gamma - \nu D^2 - \frac{1}{k^2}(D^2 + k^2)(\gamma + \nu D^2) & -2\Omega \\ 0 & \omega_A & \xi\Omega & \gamma - \nu D^2 \end{pmatrix} \begin{pmatrix} \beta_r \\ \beta_\theta \\ \varphi_r \\ \varphi_\theta \end{pmatrix} = 0 \tag{2.15}$$

where $D^2 = \partial_r \partial_r^\dagger - k^2$, $\zeta = \frac{r\Omega'}{\Omega}$, $\xi = \zeta + 2$, and $\omega_A = kV_A = k\frac{B_0}{\sqrt{\mu_0 \rho}}$. We consider a "local" approximation to this result, where we focus our attention at a region just around a characteristic r_0. Around this region, we assume $\Omega(r_0)$ has a constant characteristic value, as does its radial derivative $\Omega'(r_0)$. We assume that the radial perturbation wavelength is long compared to local area of investigation ($k_r \epsilon << 1$), where ϵ is the approximate width of the selected region). This assumption is dramatic, but it allows us to neglect temporarily the nonlocal effects of radial derivatives ($\partial_r \to 0$). Figure 2.1 summarizes this approximation.

2.1.1 Marginal stability - qualitative description

We will now qualitatively explore some fundamental MRI features. Consider the inviscid limit, $\nu = 0$, at marginal stability, $\gamma = 0$. In these limits, equation 2.15 yields the following dispersion relation:

$$2k^4\eta^2\xi\Omega^2 - 2(2-\xi)\Omega^2\omega_A^2 + \omega_A^4 = 0 \tag{2.16}$$

It is helpful to put this expression in terms of the dimensionless variables introduced in section 1.1: $R_m \equiv \frac{\Omega_0 L^2}{\eta}$, $S \equiv \frac{B_0 L}{\eta\sqrt{\mu_0\rho}} = \frac{V_A L}{\eta}$, and kL, where L is the system size in the z-direction. We use L here as the normalizing length, as the vertical height is the only length scale that exists in this local approximation. After this change of variables, equation 2.16 becomes:

$$2\xi(kL)^2 R_m^2 - 2(2-\xi)R_m^2 S^2 + (kL)^2 S^4 = 0 \tag{2.17}$$

Solving for R_m reveals the parameter space for which a system is unstable to MRI:

$$R_m = \frac{S(kL)}{\sqrt{2}} \frac{1}{\sqrt{(2-\xi) - \frac{(kL)^2\xi}{S^2}}} \tag{2.18}$$

One can simply read off the minimum allowed value for S:

$$S_{min} = (kL)\sqrt{\frac{\xi}{2-\xi}} \tag{2.19}$$

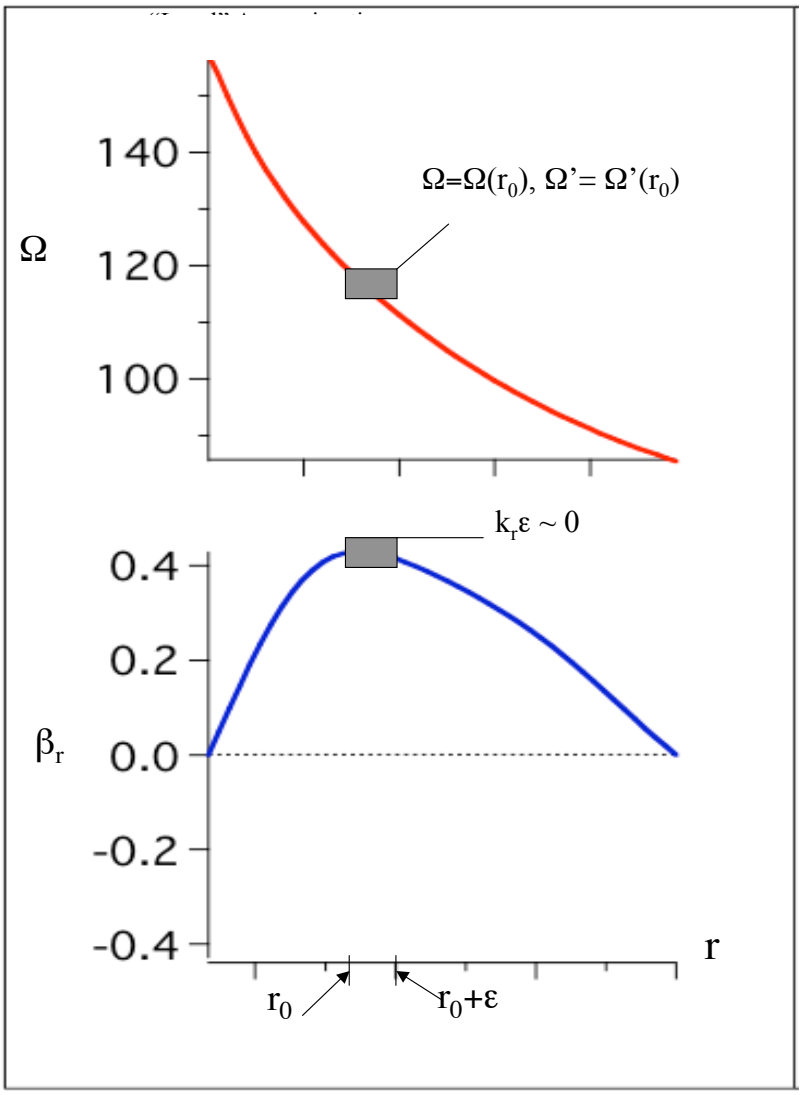

Figure 2.1: The "local" approximation. The upper curve depicts a typical Keplerian ($\Omega \propto r^{-3/2}$) flow profile as a funtion of r. The lower curve is a hypothetical depiction of the radial eigenfunction, $\beta_r(r)$. The assumption is that the radial perturbation wavelength is long compared to local area of investigation ($k_r\epsilon << 1$).

For large S, equation 2.18 reduces to an equation linear in S:

$$R_m = S\frac{(kL)}{\sqrt{2(2-\xi)}} \tag{2.20}$$

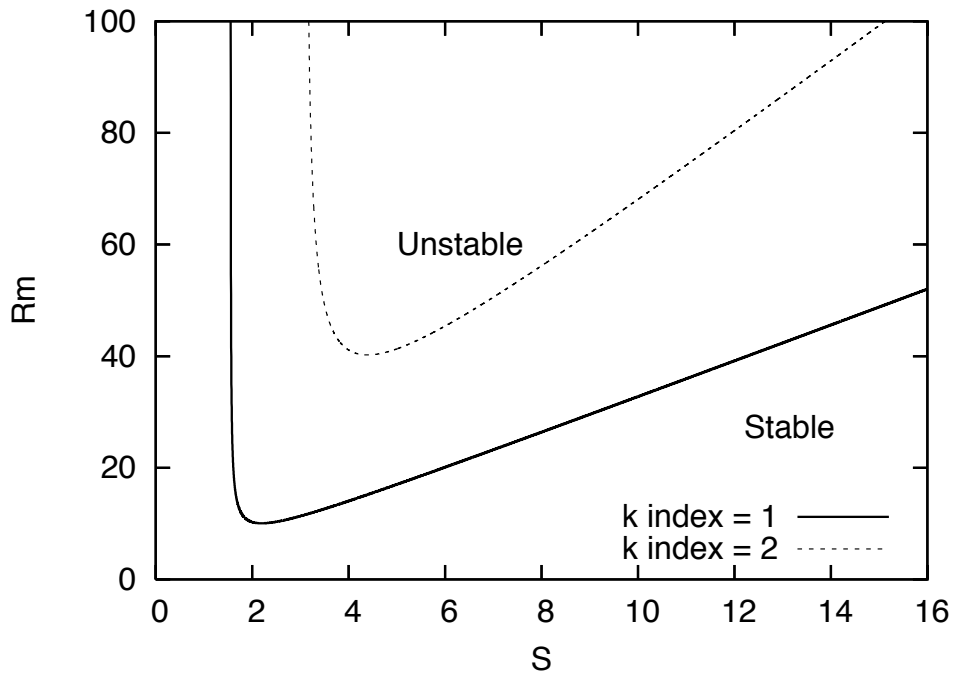

Figure 2.2: Qualititative structure of MRI marginal stability curves. The red curve is for $kL = 2\pi$, the blue curve is for $kL = 4\pi$, where L is the system height.

Equation 2.18 is plotted in Figure 2.2 for 2 different values of kL. For a fixed value of R_m above the critical value, MRI is manifest for a range of applied magnetic field strengths, $B_{min} < B_0 < B_{max}$. The lower bound comes from finite diffusion damping away the instability, and the upper bound is due to finite system size. We will explore this more in the next section.

2.1.2 Some comments on the linear MHD modes susceptible to MRI

Backing up a step or two, consider a compressible, homogeneous, non-rotating plasma threaded by an axially oriented magnetic field. Basic MHD theory tells us there are three standard waves present in such a plasma: the Alfvén wave, the slow magnetosonic wave and the fast magnetosonic wave. Applying an $e^{i(kz-\omega t)}$ disturbance to equations 2.1-2.2 yields a dispersion relation describing the propagation of these standard MHD modes (See [15] for a good discussion of these waves).

$$\omega_A^2 = k^2 V_A^2 \tag{2.21}$$

$$\omega_+^2 = k^2(V_A^2 + c_s^2) \tag{2.22}$$

$$\omega_-^2 = \frac{k^2 V_A^2 c_s^2}{c_s^2 + V_A^2} \tag{2.23}$$

where $c_s = \sqrt{\frac{\Gamma P}{\rho}}$ is the plasma sound speed. Note that if $c_s >> V_A$, as is the case in nearly incompressible, high β plasmas, the slow mode frequency becomes degenerate with the Alfvén frequency.

This incompressibile limit, also known as the Boussinesq approximation ($\frac{c_s}{V_A} = \frac{\sqrt{\Gamma P \mu_0}}{B_z} >> 1$), effectively allows us to ignore the propagation of the fast mode, ie. $\frac{\omega_+}{\omega_-} \sim \frac{\omega_+}{\omega_A} >> 1$ [1]. More generally, if the effects of finite viscosity, ν, and magnetic diffusivity, η, are included, the Alfvén frequency is adjusted, and a damping rate, γ, is introduced.

It is useful to examine the effects finite viscosity, diffusivity and rotation have on these MHD waves. Plotted in Figure 2.3 are the real (colored) and imaginary (red) roots of the dispersion relation found in section 2.1. Equations 2.15 assume incompressibility, so the behavior of fast magnetosonic waves cannot be inferred, but it is able to demonstrate the behavior of the slow and Alfvén modes. Starting in the top left panel of Figure 2.3, it is clear that these modes are degenerate. This is expected of a homogeneous, nonrotating plasma. This degeneracy can be broken by increasing ν or η, as can be seen in the top right curve. More interesting, if the plasma is allowed to rotate (bottom left), the slow mode becomes destabilized for a range of V_{Az}. This is the heart of MRI, and was demonstrated explicitly by Balbus and Hawley in 1991. In the ideal, inviscid and nondiffusive limit, no matter how small the seed magnetic field, this simple linear instability emerges. That is, to a slow disturbance, no arbitrarily weak field is negligible [1]. Even though the magnetic energy density is much less than the average thermal energy, any small perturbation grows initially unchecked. Increasing ν suppresses the physical MRI growth rate. The effect of increasing η is that a lower bound is placed on the seed field strength, meaning

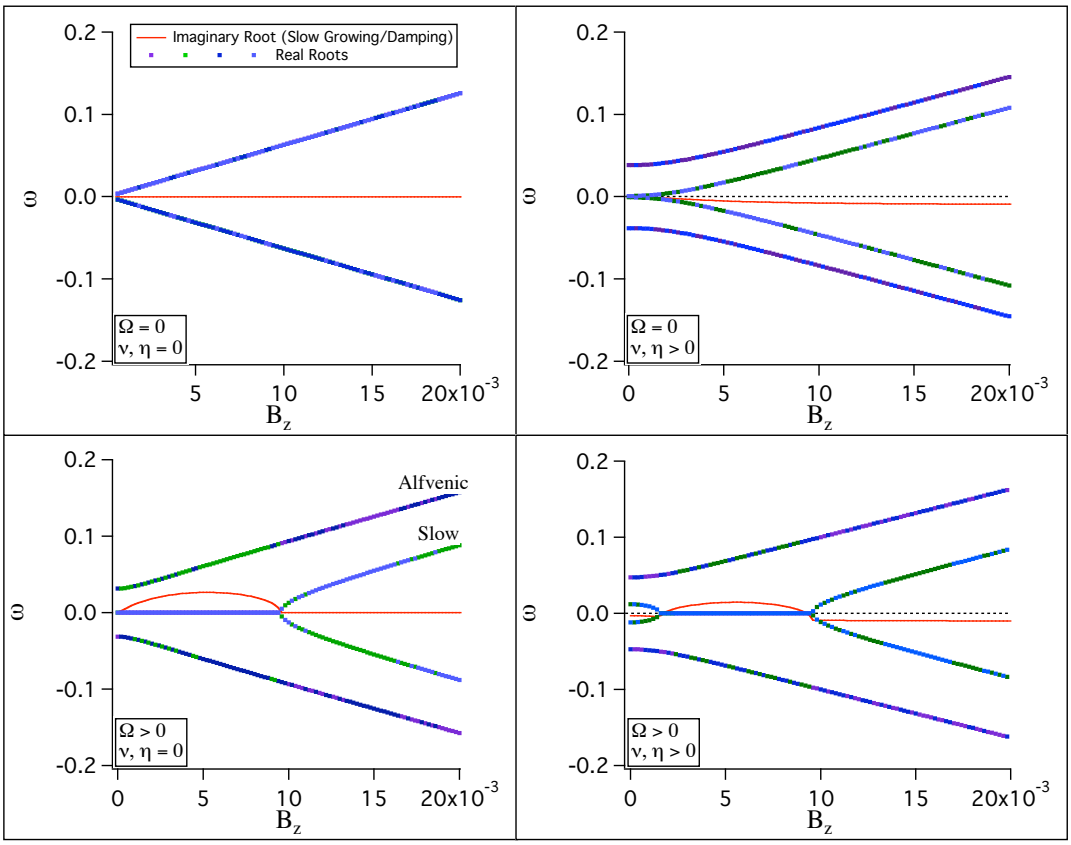

Figure 2.3: Real frequencies of slow and Alfvén modes (colored dots), and imaginary frequencies of the slow mode (solid red curve). MRI, the destabilization of the slow mode, emerges as Ω is increased, as can be seen by the positive values of the red curve in the bottom left panel. A finite value of η has the effect of placing a lower bound on the seed field strength required to destabilize the slow mode.

that no longer can an arbitrarily small field generate MRI. These effects can be seen in the bottom right of figure 2.3. Qualitatively, these curves agree well with Sharma, *et. al.* [16].

2.2 Global Calculation

The problem on which we will focus in this document is the manifestation of MRI in a system of differentially rotating coaxial cylinders. The electrically conducting flow being studied resides between the two cylinders, whose radii and angular rotation rates are a, b and Ω_1, Ω_2, respectively. The system is diagrammed in Figure 2.4.

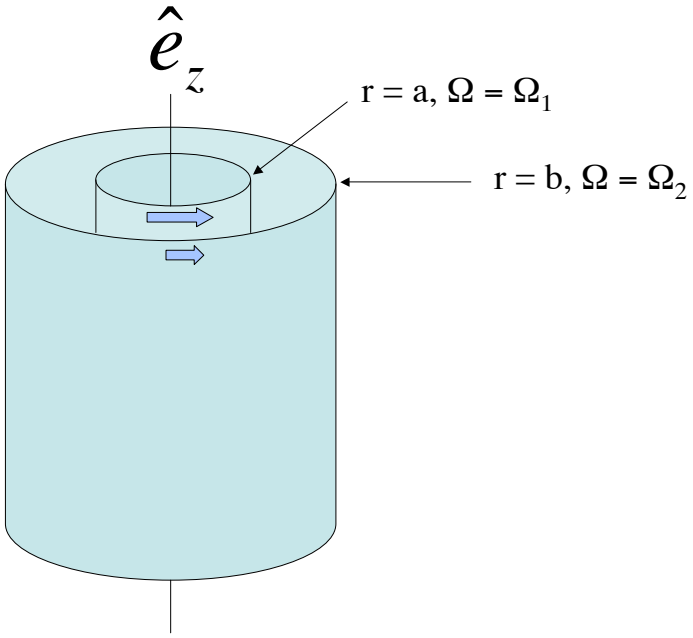

Figure 2.4: Plasma is contained in the region between the cylinders of radii and angular rotation rates a, b and Ω_1, Ω_2, respectively.

2.2.1 Taylor-Couette flow

Free of any magnetic fields, the flow of a uniformly viscous fluid between such cylinders is known as Taylor-Couette flow, a subject which has been extensively studied in the field of hydrodynamics (see, for example, Koschmeider, 1993 [17]). The Navier-Stokes equation has a surprisingly simple solution for the velocity field (see section 4.3):

$$\mathbf{v}(r,\theta,z) = (C_1 r + \frac{C_2}{r})\mathbf{e}_\theta \tag{2.24}$$

$$C_1 = \frac{\Omega_2 b^2 - \Omega_1 a^2}{b^2 - a^2}, \quad C_2 = \frac{(\Omega_2 - \Omega_1)a^2 b^2}{b^2 - a^2} \tag{2.25}$$

Note the absence of v_r and v_z velocity components. Such a flow profile will be used as the primary background field for the global calculations discussed in this document.

In the zero viscosity limit, Rayliegh's criterion on specific angular momentum, $r^2\Omega(r)$, de-

termines the stability of such a flow:

$$\xi \equiv \frac{(r^2\Omega)'}{r\Omega} > 0 \rightarrow \text{stable} \tag{2.26}$$

Put another way, specific angular momentum must increase as a function of radius. More details on Taylor-Couette flow, including the effects of destabilizing it, will be investigated in Chapter 4.

2.2.2 Conducting walls

If we introduce magnetic fields into Taylor-Couette flow, we must specify the magnetic boundary conditions at the inner and outer walls, $r = a, b$. They differ depending on whether the walls are made of conducting or insulating material. We will deal exclusively with the case of conducting walls in this document. For a discussion on the effects of insulating walls on Global MRI modes, see [7].

In the case of perfectly conducting walls, the magnetic boundary conditions are:

$$\mathbf{n} \cdot \mathbf{B} = 0, \quad \mathbf{n} \times \mathbf{j} = 0 \tag{2.27}$$

where $\mathbf{n}$ is a unit vector normal to the wall. Any axial and azimuthal current densities at the edge of the fluid are effectively "absorbed" into the perfect conductor, since the fluid is a more resistive medium than the wall. The conditions in 2.27 imply the following for the axisymmetric case (at $r = a, b$):

$$B_r = 0, \quad \frac{\partial(rB_\theta)}{\partial r} = 0 \tag{2.28}$$

Chapter 3

Numerical Methods

In this chapter, we describe the three numerical methods we implemented to model MRI. These methods include a local linear dispersion relation, a finite difference code, and a pseudo-spectral code.

3.1 Local linear dispersion relation (DR)

In Chapter 2, section 2.1.1, we made approximations to the matrix equation (2.15) and came up with a qualitative description of the MRI stability boundaries. However, to get a more complete picture from the local linear dispersion relation (DR), it is useful to find the eigenvalues of matrix 2.15 to find growth rates and real frequencies of the various system eigenmodes. To this end, we will apply the local approximation (section 2.1) to 2.15, which results in a 4th order polynomial in $\frac{\gamma}{\omega_d}$ of the form:

$$A(\frac{\gamma}{\omega_d})^4 + B(\frac{\gamma}{\omega_d})^3 + C(\frac{\gamma}{\omega_d})^2 + D(\frac{\gamma}{\omega_d}) + E = 0 \tag{3.1}$$

where we have normalized the frequencies in the system to a diffusive frequency, $\omega_d = \frac{\eta}{L^2}$. The coefficients $A - E$ are in terms of the following set of 6 dimensionless parameters: $R_m = \frac{\Omega L^2}{\eta}, S = \frac{V_A L}{\eta}, kL, \frac{L}{r_0}, \xi = \frac{(r^2\Omega)'}{r\Omega}$ and $P_m = \frac{\nu}{\eta}$. Recall that in the local approximation, Ω is evaluated at a characteristic radius, r_0, and ξ is a constant determined by the derivative of $\Omega(r)$ evaluated at r_0. Thus $\frac{r_0}{L}$ and ξ are movable fit parameters, and will be used to match the DR results with the more complete global calculations. These are the dimensionless coefficients:

$$A = 1 \tag{3.2}$$

$$B = 2(kL)^2(1 + P_m) \tag{3.3}$$

$$C = (kL)^4(1 + 4P_m + P_m^2) + 2(kL)^2S^2 + 2R_m^2\xi \tag{3.4}$$

$$D = 2(kL)^2[(kL)^4P_m(1 + P_m) + (kL)^2(1 + P_m)S^2 + 2R_m^2\xi \tag{3.5}$$

$$E = (kL)^2[(kL)^6P_m^2 + 2(kL)^4P_mS^2 + 2R_m^2S^2(\xi - 2) + (kL)^2(S^4 + 2R_m^2\xi)] \tag{3.6}$$

Note that in the limits $P_m \to 0$ and $\gamma \to 0$, equation 3.1 reduces to $E = 0$, which is the same as equation 2.17. To combat the rather daunting algebra, we implemented a numerical complex rootfinder in Fortran 90 to solve for the roots of equation 3.1. The 6 dimensionless parameters need only be defined, and the output of the DR code is 4 complex roots. Note that since $A - E$ are real coefficients, these roots come in complex conjugate pairs. $Re[\gamma_{1-4}]$ are the growth or decay rates of the 4 eigenmodes, and $Im[\gamma_{1-4}]$ are their frequencies. Figure 3.1 shows the DR results for a sample scan along the S line with the remaining 5 parameters fixed. (All figures appear at the end of this chapter).

Plotted in Figure 3.2 is a comparison of our DR code results with the results published in Goodman and Ji's 2002 paper, which inspired the local linear analysis presented here [7]. They performed a similar WKB approximation to approximate the linear MRI stability boundaries, and this plot demonstrates that our results agree with their results exactly for the set of parameters that they published.

3.2 Finite Difference algorithm (FD)

To perform numerical MRI simulations, we adopted, improved, and documented a finite difference MHD initial value code in cylindrical geometry. We will from this point on refer to this code as the "FD code". The implementation is based on a finite difference algorithm with a fixed mesh

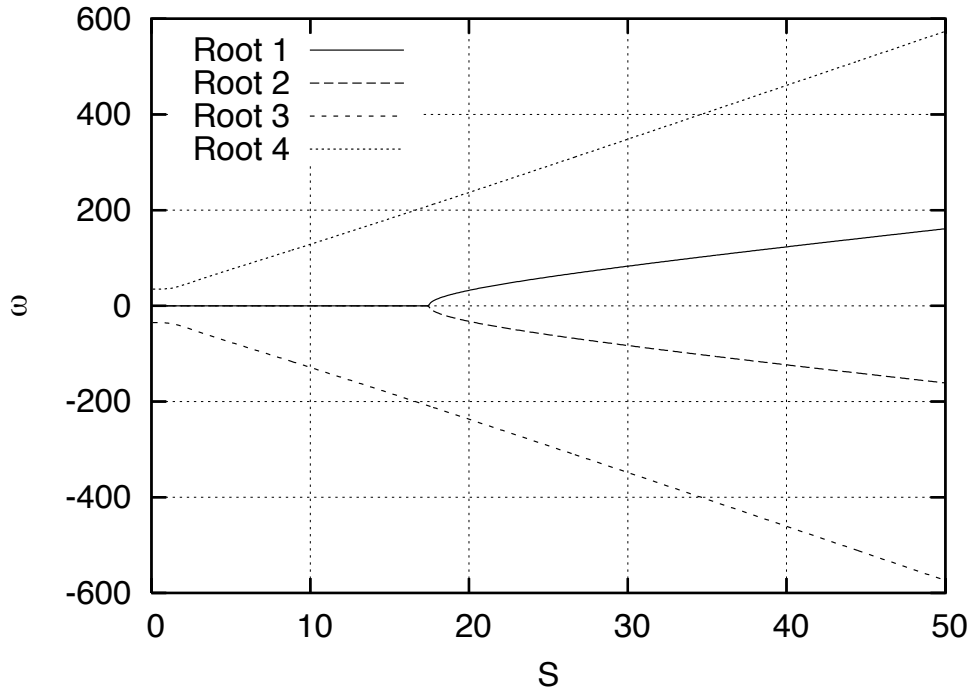

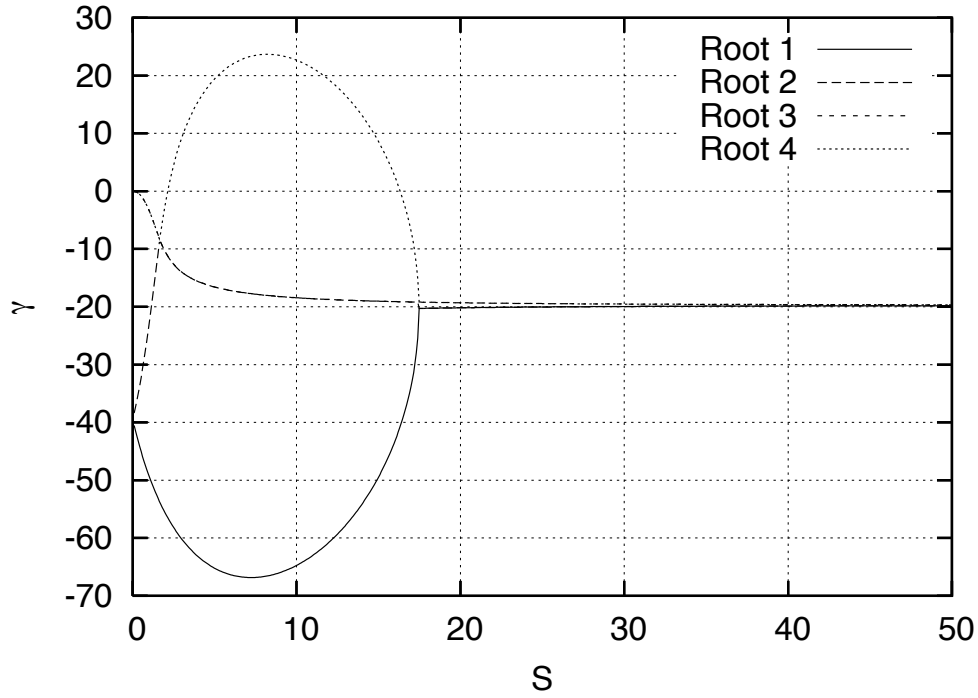

Figure 3.1: Dispersion relation output for the following input parameters: $R_m = 45, P_m = 10^{-5}, \frac{L}{r_0} = 1.64, kL = -2\pi, \xi = 0.3$, and $\beta = 4$.

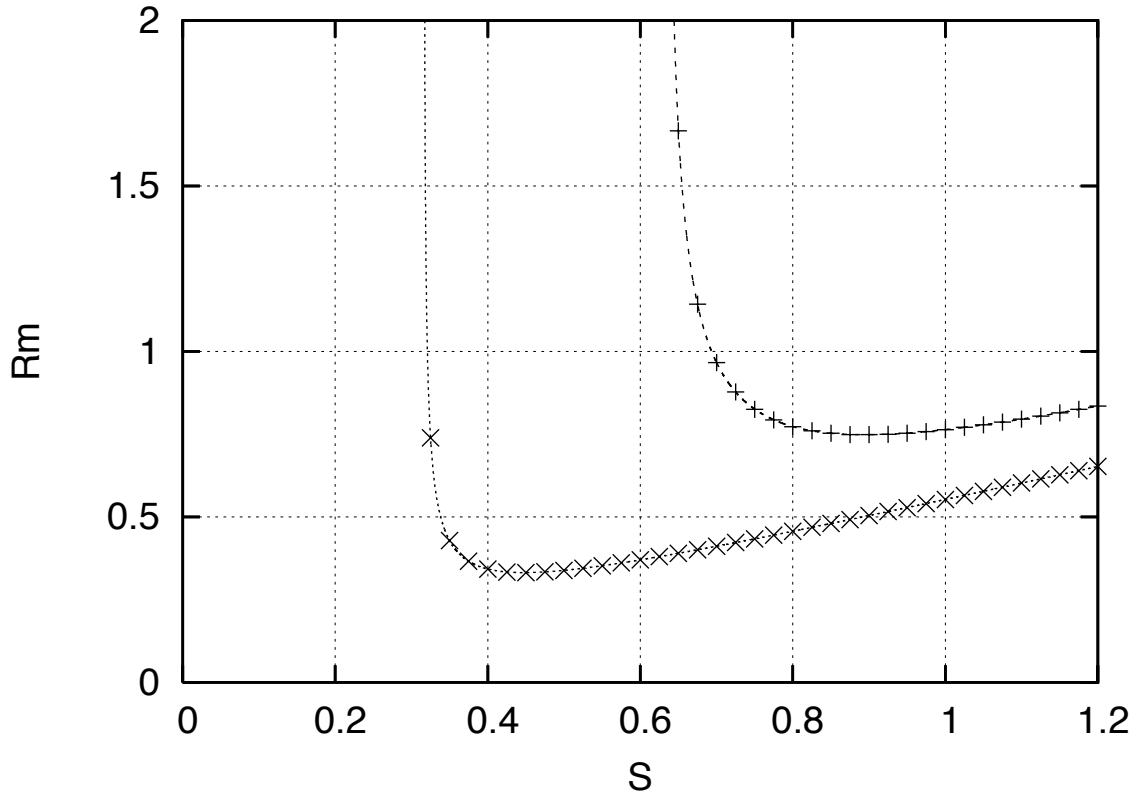

Figure 3.2: Dashed line: Local linear dispersion relation. Markers: Results from Goodman and Ji's 2002 paper, [7]. Upper curves corresponds to $\xi = \frac{4}{7}$, lower for $\xi = \frac{2}{11}$.

in the (r, z) plane. The explicit time-stepping scheme is the trapezoidal leapfrog algorithm, which stably advances wave equations, even with zero viscosity and diffusion [18].

The modular structure of this University of Maryland code is depicted diagrammatically in Figure 3.3. We have added to the code a suite of diagnostics for convenient data analysis and have integrated the FFTW (Fastest Fourier Transform in the West, [19]) library for complete spectral analysis capability.

The code solves the equations of compressible MHD (equations 3.7 - 3.10), but by forcing the temperature of the plasma high, the code simulates an incompressible fluid. This is because the sound speed of the plasma, $c_s = \sqrt{2\gamma T}$, becomes large, so all of the relevent dynamics of the system propagate at sub-mach velocities. A simple diagnostic which calculates $\nabla \cdot \mathbf{u}$ at various times during a run has helped to verify the approximate incompressibility of the code.

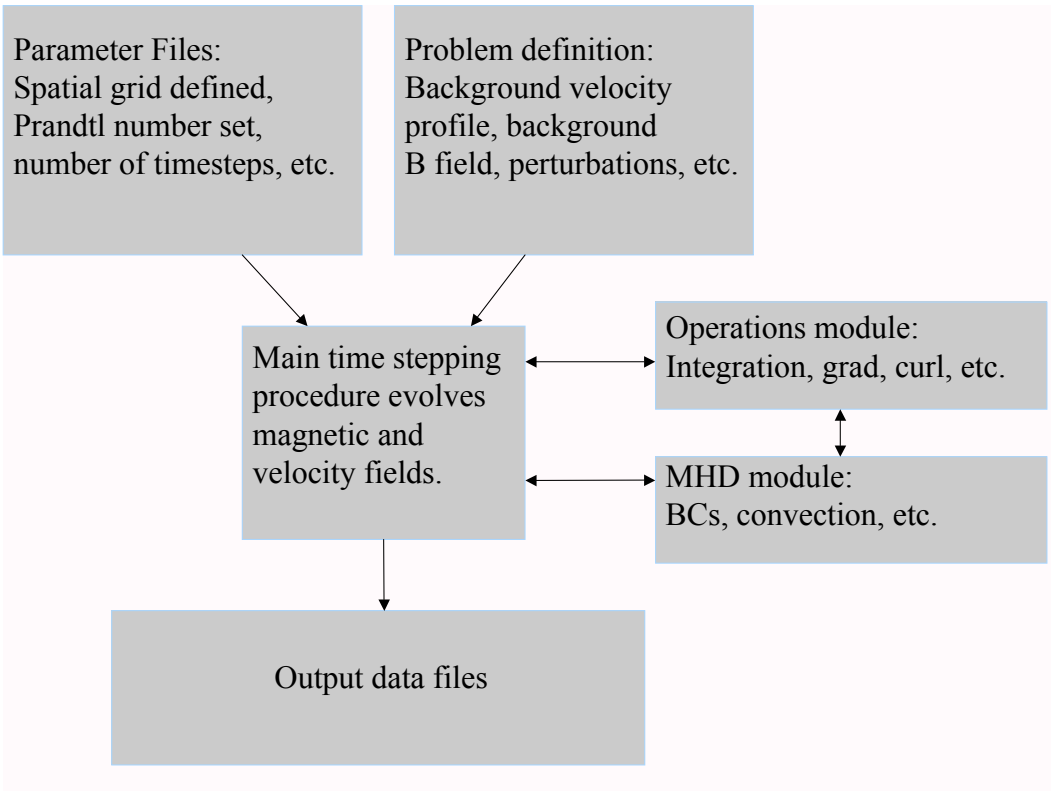

Figure 3.3: Block diagram of FD code's modularity.

3.2.1 Dimensionality Considerations

Consider the compressible MHD equations with diffusion:

$$\frac{\partial \rho}{\partial t} + \nabla \cdot (\rho \mathbf{u}) = 0 \tag{3.7}$$

$$\rho \frac{\partial \mathbf{u}}{\partial t} + \rho \mathbf{u} \cdot \nabla \mathbf{u} + \nabla P = \frac{1}{\mu_0} \nabla \times \mathbf{B} \times \mathbf{B} + \rho \nu \nabla^2 \mathbf{u} \tag{3.8}$$

$$\frac{\partial}{\partial t}(\frac{P}{\rho^\gamma}) + \mathbf{u} \cdot \nabla (\frac{P}{\rho^\gamma}) = 0 \tag{3.9}$$

$$\frac{\partial \mathbf{B}}{\partial t} = \nabla \times \mathbf{u} \times \mathbf{B} + \eta \nabla^2 \mathbf{B} \tag{3.10}$$

We non-dimensionalize these equations very generally by replacing all the variables and differential operators with a dimensionless set (denoted by the prime notation):

$$\rho = \rho_0 \rho', \quad P = P_0 P' \tag{3.11}$$

$$\mathbf{B} = B_0 \mathbf{B}', \quad \mathbf{u} = u_0 \mathbf{u}' \tag{3.12}$$

$$\frac{\partial}{\partial t} = \frac{1}{t_0}\frac{\partial}{\partial t'}, \quad \nabla = \frac{\nabla'}{L} \tag{3.13}$$

Substituting into equations 3.7-3.10 results in a dimensionless "primed" set of MHD equations:

$$\frac{\partial \rho'}{\partial t'} + [\frac{t_0 u_0}{L}]\nabla' \cdot (\rho' \mathbf{u}') = 0 \tag{3.14}$$

$$\rho' \frac{\partial \mathbf{u}'}{\partial t'} + [\frac{t_0 u_0}{L}]\rho' \mathbf{u}' \cdot \nabla' \mathbf{u}' + [\frac{P_0 t_0}{\rho_0 u_0 L}]\nabla' P' = [\frac{B_0^2 t_0}{\mu_0 \rho_0 u_0 L}]\nabla' \times \mathbf{B}' \times \mathbf{B}' + [\frac{\nu t_0}{L^2}]\rho' \nabla'^2 \mathbf{u}' \tag{3.15}$$

$$\frac{\partial}{\partial t'}(\frac{P'}{\rho'^{\gamma}}) + [\frac{t_0 u_0}{L}]\mathbf{u}' \cdot \nabla'(\frac{P'}{\rho'^{\gamma}}) = 0 \tag{3.16}$$

$$\frac{\partial \mathbf{B}'}{\partial t'} = [\frac{t_0 u_0}{L}]\nabla' \times \mathbf{u}' \times \mathbf{B}' + [\frac{\eta t_0}{L^2}]\nabla'^2 \mathbf{B}' \tag{3.17}$$

In front of each term in this "primed" set is a dimensionless parameter, contained in brackets. This set of parameters consists of the following:

$$p_1 \equiv \frac{t_0 u_0}{L}, \quad p_2 \equiv \frac{P_0 t_0}{\rho_0 u_0 L} \tag{3.18}$$

$$p_3 \equiv \frac{B_0^2 t_0}{\mu_0 \rho_0 u_0 L}, \quad p_4 \equiv \frac{\nu t_0}{L^2} \tag{3.19}$$

$$p_5 \equiv \frac{\eta t_0}{L^2} \tag{3.20}$$

The code itself is solving the dimensionless set of equations 3.14 - 3.17, and the specific selections of the dimensionless parameters reveals how things are normalized. The first three dimensionless parameters, p_1, p_2, and p_3 are normalized to unity in the code. This means

$$\sqrt{p_1 p_3} = \frac{B_0}{\sqrt{\mu_0 \rho_0}}\frac{t_0}{L} = \frac{V_A}{u_0} = 1 \tag{3.21}$$

So all velocities in the code are scaled with the Alfven speed. This also means that

$$t_0 = \frac{L}{V_A} \tag{3.22}$$

Now, since $P = 2nT$, p_2 can be rewritten

$$p_2 = \frac{2T_0 t_0}{mV_A^2} = 1 \tag{3.23}$$

So temperatures in the problem are normalized to $T_0 = \frac{1}{2}mV_A^2$. After this, the user is free to select any normalizing B_0, ρ_0 and L to fit the problem.

For example, assume the code outputs a quantity which grows exponentially at some rate, γ_c. This corresponds to the dimensionless quantity $\gamma_p t_0$, where γ_p is the real physical growth rate. So one can solve for γ_p depending on the selections of B_0, ρ_0 and L (which are contained in the timescale t_0).

3.2.2 Verification - Alfvén waves

As we did in section 2.1.2, we consider a nonrotating homogeneous plasma threaded by a magnetic field oriented in the z-direction, $\mathbf{B_0} = B_0\hat{\mathbf{z}}$. Applying an $e^{i(k_z z - \omega t)}$ disturbance to equations 3.7 - 3.10 yields a dispersion relation describing the propagation of standard MHD modes, specifically an Alfvén mode, a fast magnetosonic mode and a slow mode:

$$\omega_A^2 = k_z^2 V_A^2 \tag{3.24}$$

$$\omega_+^2 = k_z^2(V_A^2 + c_s^2) \tag{3.25}$$

$$\omega_-^2 = \frac{k_z^2 V_A^2 c_s^2}{c_s^2 + V_A^2} \tag{3.26}$$

where $c_s = \sqrt{\frac{\Gamma P}{\rho}}$ is the plasma sound speed. Note that if $c_s >> V_A$, as is the case in nearly incompressible, high β plasmas, then the slow and Alfvén modes become degenerate. In this incompressibile limit, we are effectively allowed to ignore the propagation of the fast mode, *ie.*

$\frac{\omega_+}{\omega_-} \sim \frac{\omega_+}{\omega_A} >> 1$ [1]. More generally, if we consider the effects of finite viscosity, ν, and magnetic diffusivity, η, the Alfvén frequency is adjusted, and a damping rate, γ, is introduced (this result is derived from the dispersion relation introduced in Chapter 2):

$$\omega_A = \pm\frac{k_z^2}{2}\sqrt{4\frac{V_A^2}{k_z^2} - (\nu-\eta)^2} \approx \pm k_z V_A, \quad \gamma = k_z^2(\nu+\eta) \tag{3.27}$$

To verify the performance of the FD code, we first applied initial perturbations of the form $B_r(r,z) = B_p \sin k_z z$ and $V_\theta(r,z) = V_p \sin k_z z$, where $B_p << B_0$ and $\frac{k_z L}{2\pi} = 1$ (one wavelength in the box). In addition, although the code is in cylindrical coordinates, the inner cylinder radius, a, was made 1000 times larger than the gap width, $b-a$, so as to generate a nearly Cartesian homogeneous plasma. Plotted in figure 3.4 are the real Alfvén frequency and the damping rate of the resulting single standing Alfvén wave as a function of increasing $(\nu+\eta)$ (for a fixed value of $\frac{k_z \nu}{V_A} = 3.14 \times 10^{-3}$). The solid curves are equations 3.27 and the markers are the observed frequencies from the output of the initial value code. As expected, in the inviscid, non-diffusive limit, the damping is cut off and the real frequency $\omega_A = k_z V_A$. This verification exercise indicated that the FD code was well equipped to accurately simulate the behavior of MHD modes, which include the potentially MRI unstable mode in the rotating case.

3.3 Spectral Algorithm

In addition to the FD code described in the previous section, we also employed a pseudospectral algorithm to model magnetized cylindrical Couette flow. It is a two-dimensional incompressible MHD code, with periodic boundary conditions in the z direction. The radial structure of the field variables is expanded in a series of N Chebyshev basis functions, $T_n(x)$. These polynomial functions have the property $T_n(cos[\theta]) = cos(n\theta)$, where $\theta = \pi/(n-1)$ and $n \in [1, N]$ [20]. The N radial collocation points are consequently distributed evenly in θ, such that:

$$r_n = r_0 + \frac{(b-a)}{2} cos[(n-1)\theta] \tag{3.28}$$

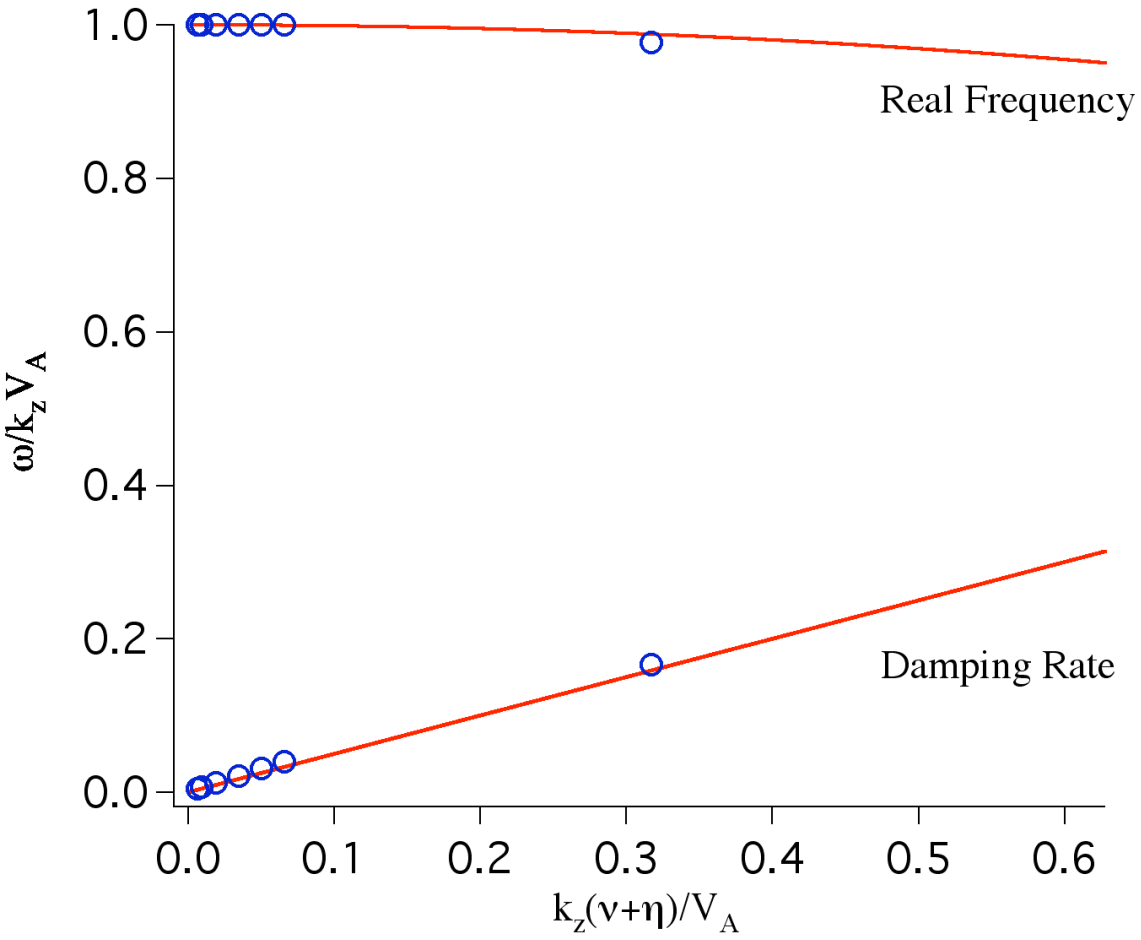

Figure 3.4: Alfven frequencies – real (oscillatory) and -imag(damping)

where r_0 is the distance from the origin to the center of the gap between the cylinders, and a and b are the cylinders' radii, as usual. The locations of these collocation points are shown in Figure 3.5 for $N = 40, r_0 = 1$ and $b - a = 1$. Note how the gridpoints are naturally clustered near the inner and outer walls - this will prove to be advantageous in modeling MRI, as sharp boundary layers can emerge in these regions for lower P_m flows.

The four field variables evolved are the theta component of the vorticity, ω, the azimuthal velocity v_θ, the magnetic flux function, ψ, and the azimuthal magnetic field component, B_θ. We

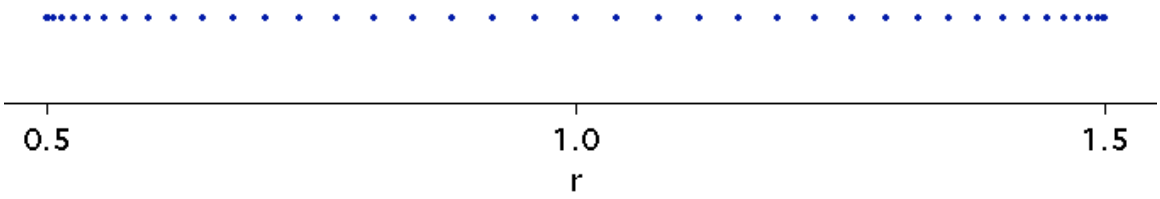

Figure 3.5: Clustering of gridpoints at boundaries in the spectral code.

will now derive the evolution equations for these variables. First, let

$$\boldsymbol{v} = \nabla \times [\phi(r,z)\nabla\theta] + r v_\theta(r,z)\nabla\theta = \begin{pmatrix} -\partial_z\phi/r \\ v_\theta \\ (\partial_r\phi)/r \end{pmatrix} \tag{3.29}$$

$$\boldsymbol{B} = \nabla \times [\psi(r,z)\nabla\theta] + r B_\theta(r,z)\nabla\theta = \begin{pmatrix} -\partial_z\psi/r \\ B_\theta \\ (\partial_r\psi)/r \end{pmatrix}, \tag{3.30}$$

Note that this naturally imposes divergence free velocity and magnetic fields (since axisymmetry is assumed), conditions necessary for incompressible MHD. Their curls are:

$$\nabla \times \boldsymbol{v} = \begin{pmatrix} -\partial_z v_\theta \\ -\partial_r[(\partial_r\phi)/r] - \partial_z^2\phi/r \\ [\partial_r(r v_\theta)]/r \end{pmatrix} \tag{3.31}$$

$$\nabla \times \boldsymbol{B} = \begin{pmatrix} -\partial_z B_\theta \\ -\partial_r[(\partial_r\psi)/r] - \partial_z^2\psi/r \\ [\partial_r(r B_\theta)]/r \end{pmatrix}. \tag{3.32}$$

Next, we will define vorticity and current density:

$$\omega = -(\nabla \times \boldsymbol{v})_\theta = \partial_r \left(\frac{1}{r}\partial_r \phi\right) + \frac{1}{r}\partial_z^2 \phi \equiv \nabla_*^2 \phi \tag{3.33}$$

$$j = -(\nabla \times \boldsymbol{B})_\theta = \partial_r \left(\frac{1}{r}\partial_r \psi\right) + \frac{1}{r}\partial_z^2 \psi = \nabla_*^2 \psi, \tag{3.34}$$

We make the following observation:

$$[\nabla \times \{\boldsymbol{v} \times (\nabla \times \boldsymbol{v})\}]_\theta = \left[\phi, \frac{\omega}{r}\right] + \partial_z \left(\frac{v_\theta^2}{r}\right), \tag{3.35}$$

$$[\nabla \times \{\boldsymbol{B} \times (\nabla \times \boldsymbol{B})\}]_\theta = \left[\psi, \frac{j}{r}\right] + \partial_z \left(\frac{B_\theta^2}{r}\right), \tag{3.36}$$

where we have used the normal Poisson bracket formalism:

$$[f, g] = \partial_r f \partial_z g - \partial_z f \partial_r f. \tag{3.37}$$

Since

$$\nabla^2 \boldsymbol{v} = \begin{pmatrix} -\partial_z(r\omega)/r \\ (\partial_r D_r + \partial_z^2) v_\theta \\ [\partial_r(r\omega)]/r \end{pmatrix} \tag{3.38}$$

and

$$[\nabla \times (\nabla^2 \boldsymbol{v})]_\theta = -\left\{\partial_r \left[\frac{1}{r}\partial_r(r\omega)\right] + \frac{1}{r}\partial_z^2(r\omega)\right\} = -\nabla_*^2(r\omega) \tag{3.39}$$

$$(\nabla^2 \boldsymbol{v})_\theta = \nabla_*^2(r v_\theta) \tag{3.40}$$

we arrive at the first 2 equation to evolve, the θ-component of the vorticity equation:

$$\partial_t \omega + \left[\phi, \frac{\omega}{r}\right] + \partial_z \left(\frac{v_\theta^2}{r}\right) = \left[\psi, \frac{j}{r}\right] + \partial_z \left(\frac{B_\theta^2}{r}\right) + \nu \nabla_*^2(r\omega) \tag{3.41}$$

and the θ-component of the equation of motion:

$$\partial_t v_\theta + \frac{1}{r^2}[\phi, r v_\theta] = \frac{1}{r^2}[\psi, r B_\theta] + \nu \nabla_*^2 (r v_\theta) \tag{3.42}$$

Also, since

$$\nabla \times (\boldsymbol{v} \times \boldsymbol{B}) = \begin{pmatrix} \frac{1}{r^2}\partial_z[\phi, \psi] \\ \left[\psi, \frac{v_\theta}{r}\right] - \left[\phi, \frac{B_\theta}{r}\right] \\ -\frac{1}{r}\partial_r \left(r \cdot \frac{1}{r^2}\,[\phi, \psi] \right), \end{pmatrix} \tag{3.43}$$

we obtain

$$\partial_t \psi + \frac{1}{r}[\phi, \psi] = \eta r j \tag{3.44}$$

and

$$\partial_t B_\theta + \left[\phi, \frac{B_\theta}{r}\right] - \left[\psi, \frac{v_\theta}{r}\right] = \eta \nabla_*^2 (r B_\theta) \tag{3.45}$$

from the induction equation. Equations 3.41, 3.42, 3.44, and 3.45 are the ones that are evolved by the spectral code.

3.4 Code comparison and Benchmarking

Finite difference algorithms use a sequence of overlapping polynomials to interpolate a solution over a set of gridpoints. The spatial derivatives of the solution are computed from these locally interpolated values, and their degree of accuracy is dependent on the number of gridpoints used to approximate the derivative. The highest order derivatives used in the FD code are fourth order, so the error in the approximation to the solution goes like $(1/N)^4$, where N is number of gridpoints used. The pseudospectral algorithm, on the other hand, uses one high order polynomial to approximate the solution over the entire domain, and the error goes like $(1/N)^N$. This exponential convergence to the solution is the primary advantage to pseudospectral algorithms.

The pseudospectral algorithm has the additional advantage of memory efficiency. Problems that require high resolution, such has high Reynolds number flow, can often be done by spectral

methods when a finite difference code solving the same problem would fail because of the need for many more grid points [20]. This is why for most problems involving high Reynolds number we will employ the spectral code.

The last advantage to the spectral code is the fact that it is based on a set of incompressible equations. Because the FD code is compressible, the temperature must be increased to clearly separate the timescales of the fast magnetosonic mode and the Alfvénic modes. This in turn increases the restriction on the allowable timestep, because the code must be able to resolve the high frequency sound wave perturbations. The spectral code can take a considerably longer timestep to observe the same Alfvénic phenomenon.

Even though it seems like the spectral code is the clear winner, we have used the FD code for several important reasons. The primary advantage of the FD code is that it has flexibility to extend to three dimensions, and we will address the many interesting consequences of MRI in 3D in Chapter 7. The FD code has also been extremely useful in benchmarking the 2D simulation results of $P_m \sim 1$ flows.

Since we will be using both codes to solve similar problems, it is important to determine that they are arriving at comparable solutions. Figure 3.6 shows the growth rates of an unstable mode as a function of applied field strength for a fixed set of parameters, as calculated by all three of the methods described in this chapter. This plot demonstrates that both global simulations can predict the growth rate of an MRI mode as predicted by the linear theory. The agreement between both codes and the local linear MRI dispersion relation is excellent. This simulation will be discussed more in the next chapter, which deals with global MRI simulation in particular.

To verify that both codes are predicting the same global spatial behavior, we have plotted B_r in the r-z plane in the nonlinear state using both codes (figure 3.7). The results from the two codes are almost identical, save a small phase difference in the z-direction, primarily due to the random initial conditions.

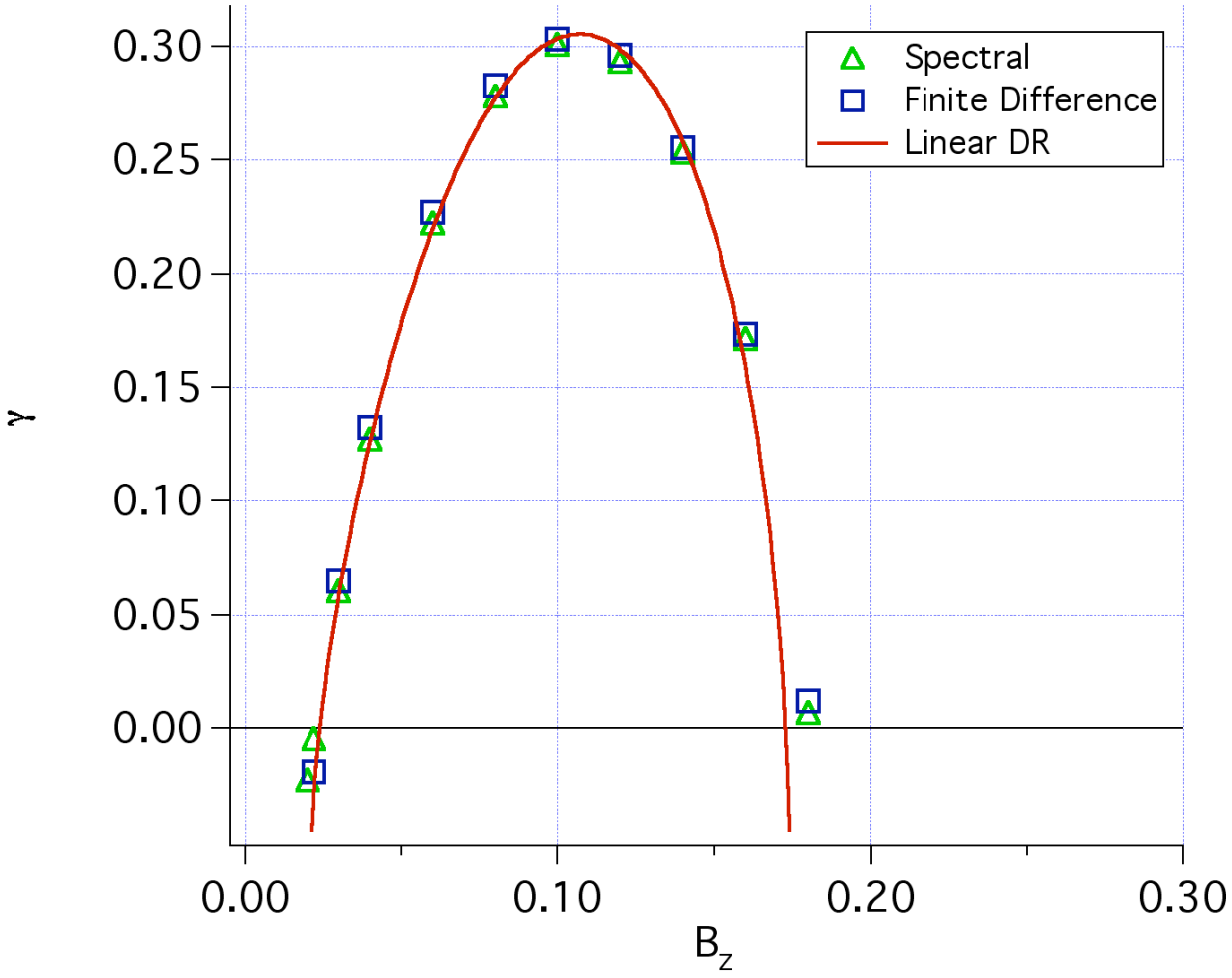

Figure 3.6: Three simulations at the following parameters: $a = 0.5, b = 1.5, \Omega_1 = 0.8, \mu = 0.27, L = 1, P_m = 0.1$. Results indicate good agreement between the Spectral code, FD code and local linear dispersion relation.

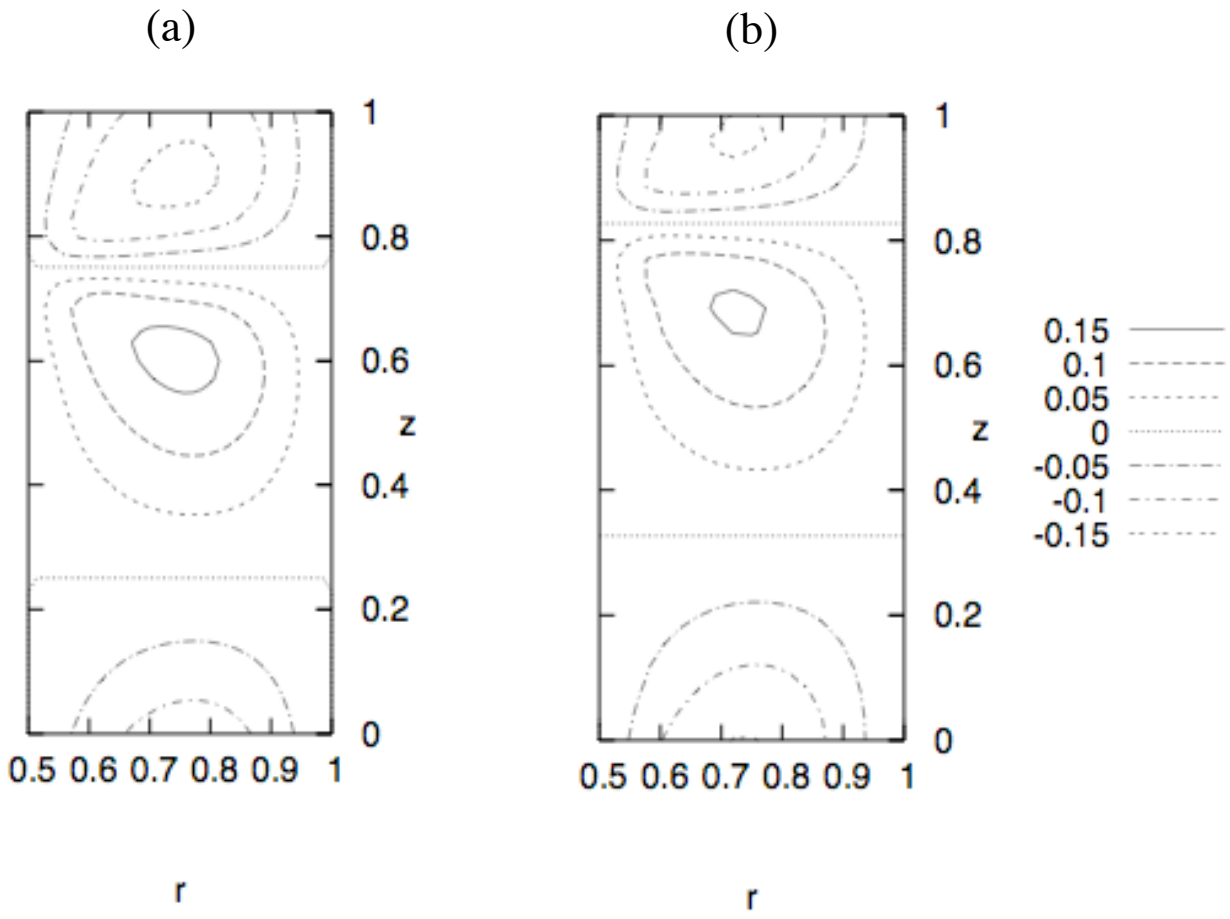

Figure 3.7: (a) Finite difference algorithm for the following parameters: $a = 0.5, b = 1, \Omega_1 = 2, \mu = 0.35, B_0 = 0.2, L = 1, P_m = 1$, and $\nu = 7 \times 10^{-4}$. (b) Spectral algorithm using the same parameters. The phase shift in the axial direction is only an artifact of random initial conditions.

Chapter 4

Hydrodynamic Stability of Shear Flows

4.1 Keplerian laminar flow

The most fundamental accretion flow is one which is feuled only by gravitation. A fluid bound by a gravitational potential will exhibit differential rotation simply because those fluid elements further from the central object feel less gravitational force. A very simple balancing of forces can determine the nature of this shear flow. Equating gravitational and centripetal forces for a given fluid element of mass m circularly orbiting a distance r away from an object of mass M:

$$G\frac{mM}{r^2} = m\frac{v^2}{r} \tag{4.1}$$

where G is Newton's gravitational constant. Solving for v:

$$v = \frac{\sqrt{GM}}{r^{1/2}} \propto \frac{1}{r^{1/2}} \tag{4.2}$$

Consequently, orbital angular frequency $\Omega(r) = \frac{v}{r} \propto \frac{1}{r^{3/2}}$ and angular momentum density $L = \rho v r \propto r^{1/2}$. Such is the nature of laminar Keplerian flow. It is important to note that while $\Omega(r)$ and $v(r)$ both decrease with increasing radius, the angular momentum increases. Plotted in Figure 4.1 are these functional dependencies of Ω, v and L on r.

4.2 Stability consideration for differential rotation

That $L(r)$ should increase with radius is a requirement for stable differential rotation. This can be understood clearly by invoking an energy argument. Consider a flat accretion disk differentially rotating as described above, though not necessarily Keplerian. Let us focus on two orbiting rings of width dr centered at R_1 and R_2, respectively. Fluid elements in these rings are moving about

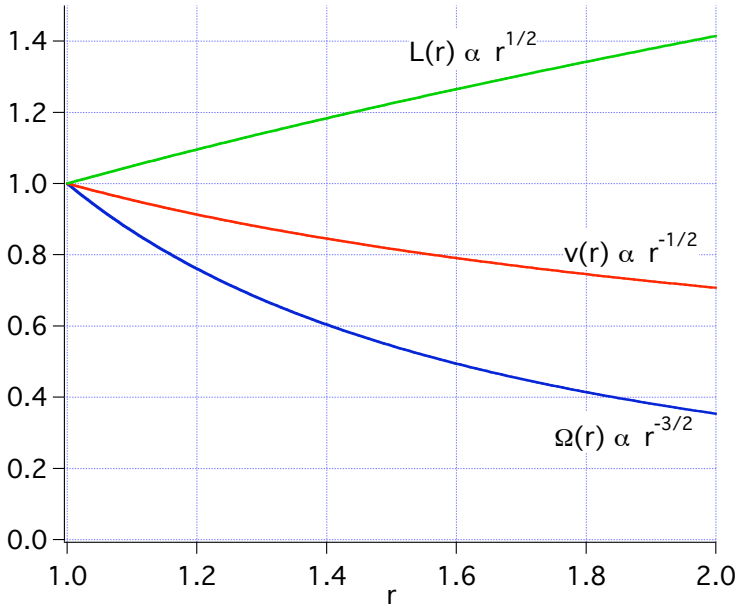

Figure 4.1: Flow profile dependencies for a typical Keplerian accretion disk. Note how angular momentum, $L(r)$ increases with radius, while orbital angular frequency, $\Omega(r)$, and velocity, $v(r)$ both decrease.

the central object according to thier angular momentum profiles, $L_1 \equiv L(R_1)$ and $L_2 \equiv L(R_2)$. One can calculate the total energy density carried by the fluid in these rings:

$$E = E_1 + E_2 = \int_0^{2\pi} \frac{1}{\rho}(\frac{L_1^2}{R_1} + \frac{L_2^2}{R_2})d\theta = 2\pi\frac{1}{\rho}\frac{L_2^2}{R_2}(1 + \frac{L_1^2}{L_2^2}\frac{R_2}{R_1}) \tag{4.3}$$

Now, imagine that we are able to force the rings to trade places - that is, we force the ring centered at R_1 to carry specific angular momentum L_2 and the ring centered at R_2 to carry L_1. If we do the same energy calculation after the rings are switched, we get:

$$E_{new} = \int_0^{2\pi} \frac{1}{\rho}(\frac{L_2^2}{R_1} + \frac{L_1^2}{R_2})d\theta = 2\pi\frac{1}{\rho}\frac{L_2^2}{R_2}(\frac{L_1^2}{L_2^2} + \frac{R_2}{R_1}) \tag{4.4}$$

Comparing the "old" energy with the "new":

$$\frac{E_{old}}{E_{new}} = \frac{1 + (\frac{L_1}{L_2})^2\frac{R_2}{R_1}}{(\frac{L_1}{L_2})^2 + \frac{R_2}{R_1}} \tag{4.5}$$

Equation 4.5 has the property that if $L_1 < L_2$, $E_{old} < E_{new}$. If $L_1 > L_2$, $E_{old} > E_{new}$, and if $L_1 = L_2$ (flat profile), the energy remains unchanged. It can then be deduced that if the specific angular momentum in a disk decreases with radius, the system could relax to a lower energy state by transporting angular momentum *outward*. This is the nature of the centrifugal instability. While many accretion disks are not susceptible to such an instabilty due to their near Keplerian orbits, Taylor-Couette flow profiles can easily be set up with an increasing $L(r)$, as we will see in the next section.

4.3 Taylor-Couette flow

Taylor-Couette flow refers to the flow between 2 coaxial cylinders of radii a and b rotating with angular frequencies Ω_1 and Ω_2. The system is assumed to be periodic in the axial (z) direction. One can show that $v_\theta = v_\theta(r)$ is an equilibrium solution of the Navier-Stokes equations. In the presence of viscosity and in the absence of turbulence, the radial profile of the flow can be determined from the azimuthal component of the steady-state momentum equation

$$\nu \nabla^2 v_\theta = \nu \left[\frac{d^2 v_\theta}{dr^2} + \frac{1}{r}\frac{dv_\theta}{dr} - \frac{v_\theta}{r^2} \right] = 0. \tag{4.6}$$

The solution to this equation is:

$$v_\theta(r) = C_1 r + \frac{C_2}{r}. \tag{4.7}$$

The boundary conditions are no slip at the walls: $v_\theta(a) = a\Omega_1$ and $v_\theta(b) = b\Omega_1$. Solving for C_1 and C_2:

$$C_1 = \frac{\Omega_2 b^2 - \Omega_1 a^2}{b^2 - a^2}, \quad C_2 = \frac{(\Omega_2 - \Omega_1) a^2 b^2}{b^2 - a^2} \tag{4.8}$$

We will parametrize Couette flow using 2 parameters: $\mu = \Omega_2/\Omega_1$ and a/b, the aspect ratio of the coaxial cylinder radii. Some sample cylindrical Couette flow profiles are shown in Figure 4.2.

If we assume that $v_r = v_z = 0$ in the bulk of the fluid (we are only interested in the time behavior of the v_θ profile), the tendency of an arbitrarily initialized v_θ profile in a viscous fluid

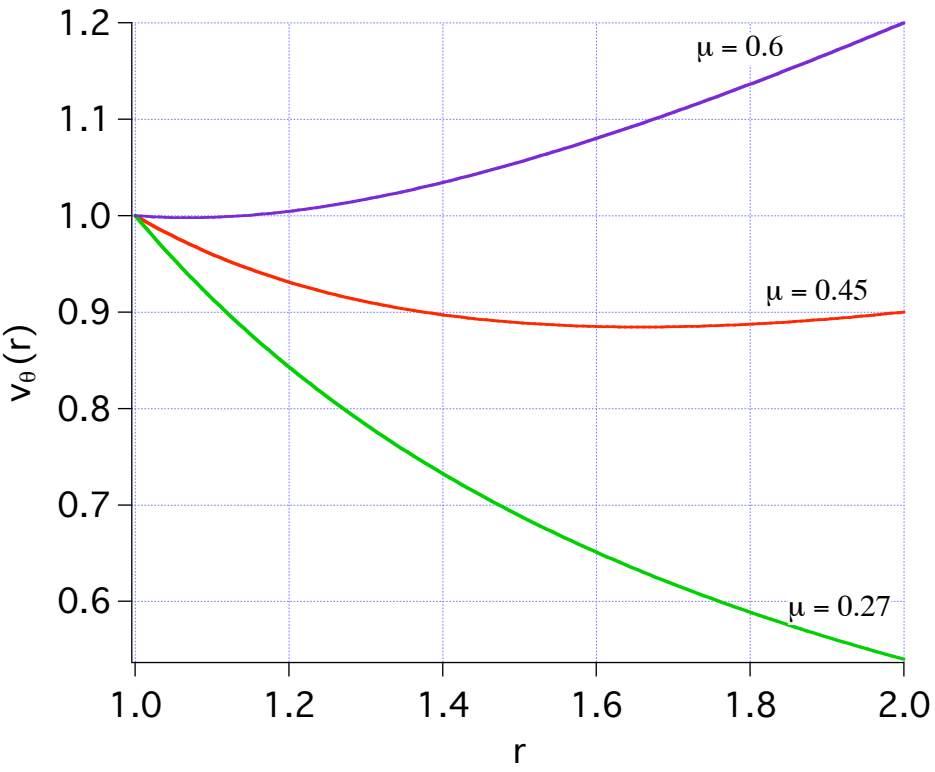

Figure 4.2: Sample cylindrical Couette flow profiles for 3 values of $\mu = \frac{\Omega_2}{\Omega_1}$. For the purposes of this illustration, $a = 1, b = 2$ and $\Omega_1 = 1$.

is to relax to this Taylor-Couette solution. As a demonstration of this, see Figure 4.3. Using the axisymmetric finite-difference algorithm described in Chapter 3, we initialized a flow profile far from the system's equilibrium Couette flow. The upper half of Figure 4.3 shows periodic time snapshots of the flow profile evolving over time, and it can be clearly seen that the system is relaxing to Taylor-Couette flow. The lower half of the figure plots the magnitude of deviation of the fluid velocity at center of the gap from the corresponding Couette flow solution, and we observed that this deviation exponentially decays over a timescale determined by the fluid viscosity, ν. One may guess that the structure of such an exponential dependence would be:

$$A(t) = A_0 e^{-\nu k_r^2 t} \tag{4.9}$$

The fit in the lower half of Figure 4.3 is $A(t) = A_0 e^{-11\nu t}$ ($\nu = 0.001$ during this run), so the approximate value of k_r^2 must be 11. Given that the half wavelength of the initialized structure

is roughly 1, the width of the gap, a good guess at k_r^2 would be $\pi^2 \approx 10$, so the hypothesized structure of the exponential dependence (equation 4.9) is reasonable.

4.4 Centrifugal instability in Taylor-Couette flow

In his 1923 experiments, Sir Geoffrey Ingram Taylor discovered the centrifugal instability in the context of this flow constrained by concentric cylinders. He observed that a linear axisymmetric instability would destabilize his laminar flow when the outer cylinder was fixed and the angular velocity of the inner cylinder exceeded a critical value. This instability would cause radial and axial velocity field components to grow and saturate into a series of stacked vortices, now known as Taylor vortices, consisting of outward and inward radial flows [21].

A useful tool in characterizing the hydrodynamic stability of Couette flow is the dimensionless function introduced in chapter 2 which expresses the gradient of specific angular momentum: $\xi = \frac{1}{r\Omega}\frac{d(r^2\Omega)}{dr}$. For Keplerian flow (and indeed for any flow profile which obeys a simple power law), ξ is independent of r ($\xi = 1/2$). However, for Couette flow, ξ generally depends on radius, and if $b^2\Omega_2 < a^2\Omega_1$, then $\xi(r) < 0$ over the whole domain. As was noted in the previous section, if specific angular momentum decreases with radius ($\xi(r) < 0$) anywhere in the fluid, the differential rotation could be subject to this centrifugal instability.

Figure 4.4 helps to characterize this property of Taylor-Couette flows in the space of our dimensionless parameters, μ and a/b. Plotted in the figure is the centrifugal stability criterion, $\xi(r_0)$, where r_0 is selected to be the halfway point between the cylinders. The bottom right portion of the plot is the centrifugally unstable region ($\xi < 0$). If $\xi = 2$, the cylinders' angular frequencies are synchronized (solid body rotation).

To observe the emergence of Taylor vortex flow, we used the FD code to initialize an unstable flow ($\mu = 0$), and we injected low level white noise into the v_r and v_z profiles. Our first goal was to verify that the system is destabilized as the inner cylinder rotation rate exceeds a threshold value.

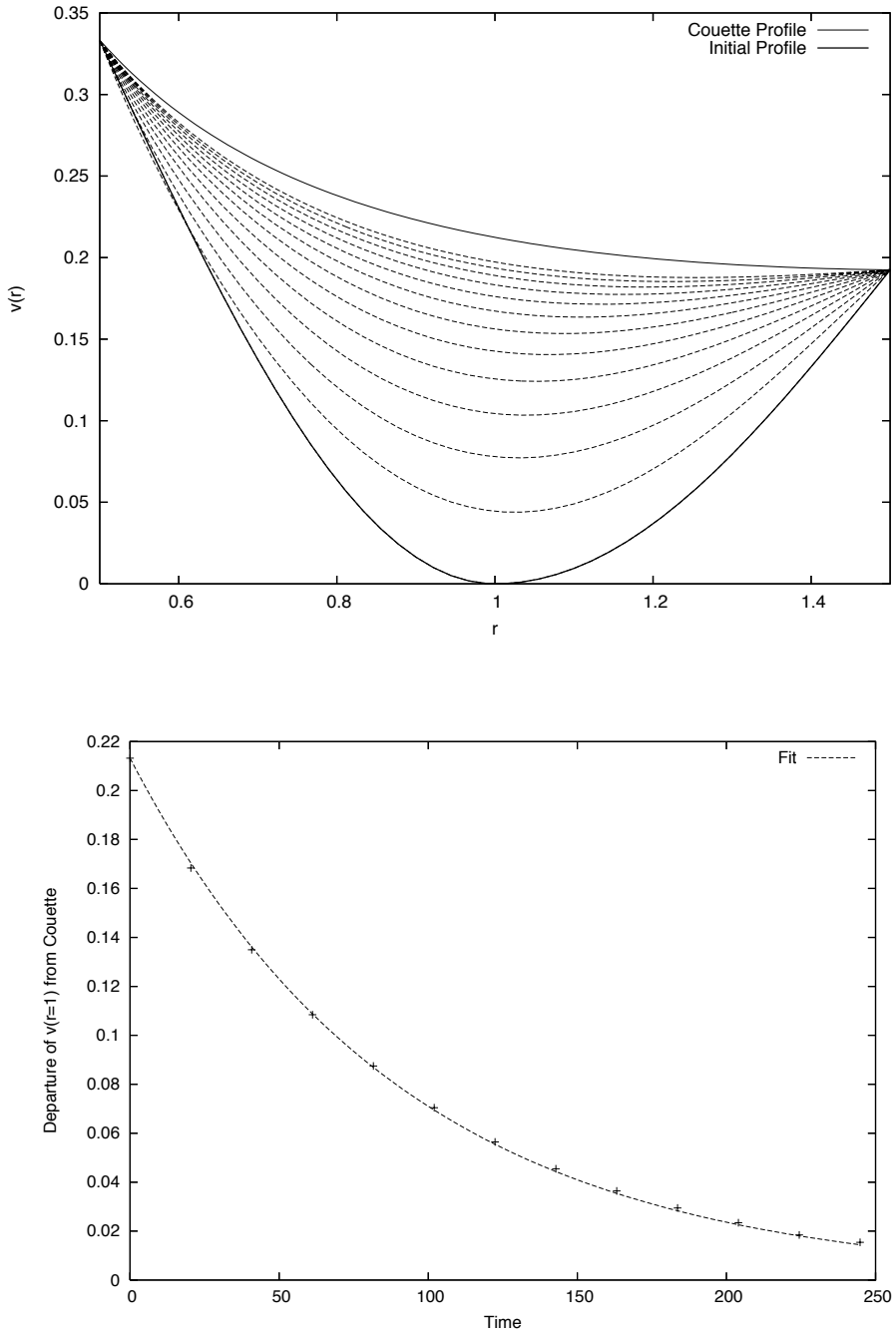

Figure 4.3: Upper: Time snapshots capturing the relaxation of $v_\theta(r)$ to the Taylor-Couette solution. Lower: The magnitude of deviation of the $v(r=1)$ from $v_{Couette}(r=1)$ as a function of time. The fit function is $A(t) = A_0 e^{-\nu k_r^2 t}$, with $k_r^2 = 11$ and $\nu = 0.001$.

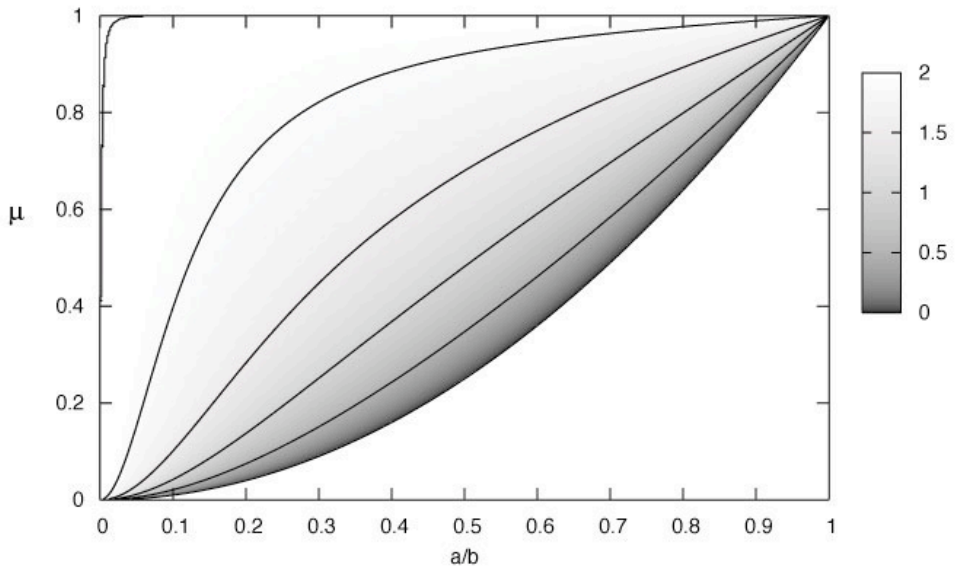

Figure 4.4: Characterization of Taylor-Couette flow profiles. Plotted is $\xi(r_0)$, where $r_0 = a + \frac{(b-a)}{2}$ (middle of the gap) and $\xi(r) = \frac{1}{r\Omega}\frac{d(r^2\Omega)}{dr}$. The contours (from bottom to top) are for $\xi(r_0) = 0, 0.5, 1, 1.5, 1.9, 2$. The system is centrifugally unstable for $\xi < 0$ (bottom right of the plot, in the white space), and potentially MRI unstable for $\xi < 2$ (the bulk of the plotted region).

For an $m = 0$ disturbance, this threshold value is:

$$R_e^* \equiv \frac{\Omega_1 H^2}{\nu} = 68, \quad H \equiv [a(b-a)]^{1/2} \tag{4.10}$$

Plotted in Figure 4.5 is a plot of the growth rates of the most unstable mode vs R_e^*, and it is clear that the $m = 0$ centrifugal instability emerges as R_e^* reaches the critical value of 68. Focusing on a Couette profile with $R_e^* = 350$ and $\mu = 0$, we observed that in the saturated state, stacked Taylor vortices in the (r, z) plane formed. These are shown in Figure 4.6.

By the time the instability saturated, the flow profile had been modified to one closer to marginal stability. This can be seen in Figure 4.7, which shows $\Omega(r)$ and $\xi(r)$ before and after

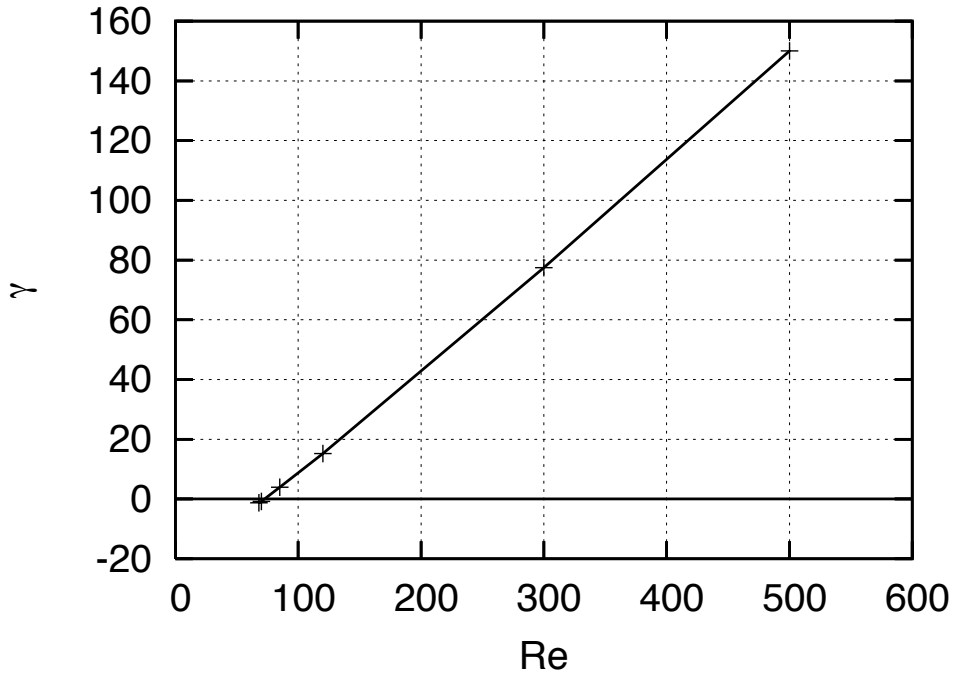

Figure 4.5: Growth rate of the most unstable mode vs. $R_e^* = \frac{\Omega_1 H^2}{\nu}$. Centrifugal instability ($m = 0$) emerges as R_e^* reaches the critical value of 68.

saturation. Initially, $\xi(r)$ was everywhere less than zero, but after saturation, $\xi(r)$ approached 0 except near the walls (located at $r = 1$ and $r = 2$). Evidently, the Taylor vortices serve to transport the angular momentum outward in such a way as to tend the system to marginal stability.

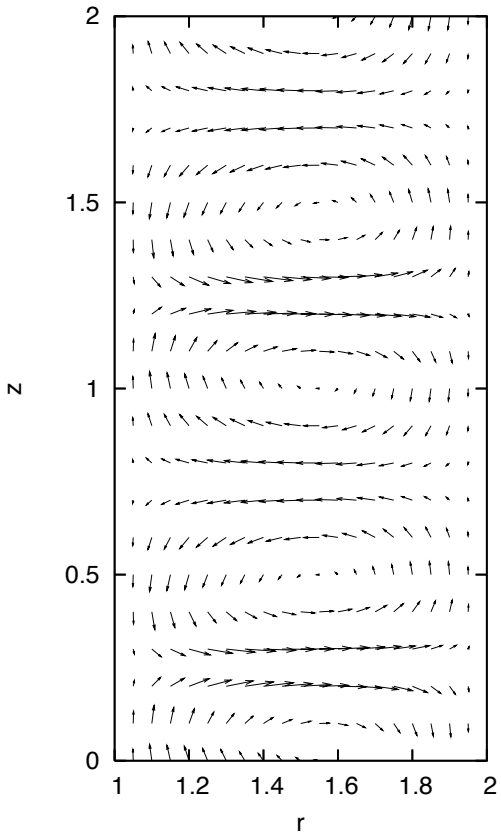

Figure 4.6: The saturated velocity field in the (r, z) plane of a destabilized couette profile. Note the presence of stacked Taylor vortices.

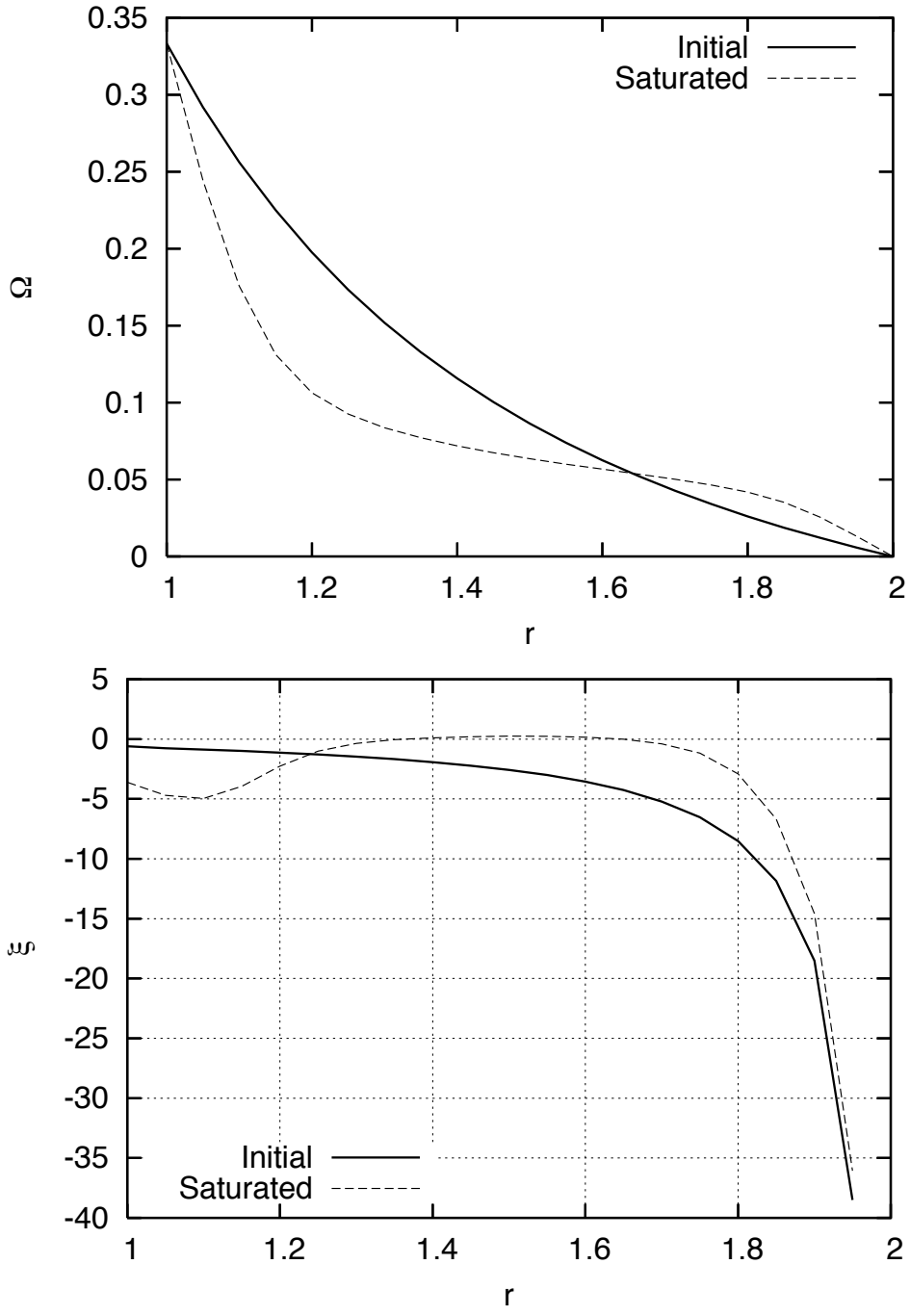

Figure 4.7: Upper: $\Omega(r)$ before and after saturation of a centrifugal instability in Taylor-Couette flow. The initialized profile was the Taylor-Couette solution, equation 4.7. Lower: $\xi(r)$ before and after. Note how the saturated flow profile is closer to marginal stability ($\xi(r) = 0$ in the fluid bulk) than the original.

Chapter 5

Axisymmetric Global MRI simulations

5.1 Computational Considerations

As discussed in Chapter 1, the most significant challenge for computationally modeling liquid metal flows is the vast separation of the viscous and diffusive timescales. For typical liquid metals, $P_m = \frac{\nu}{\eta} \approx 10^{-6}$, so if the observation of MRI requires $R_m \approx 10 - 100$, the corresponding Reynolds number of the flow is enormous: $R_e \approx 10^7$. At such a Reynolds number, resolution of the incredibly small and short timescale fluid phenomena would demand orders of magnitude more computational muscle than is currently available.

Let us investigate this resolution problem more concretely. The Reynolds number is an approximate relation of the largest length scale in the system, L, to the smallest, often referred to as the Kolmogorov length, l_k: $Re^{3/4} = L/l_k$ [9]. In fully developed turbulence, system scale perturbations have cascaded into eddies over a range of wavelengths, and l_k is the approximate size of the very smallest eddy. To study MRI at moderate Prandtl numbers, say $P_m = 1$, one must at least resolve the fluid dynamics at the critical Reynolds number, $R_e = R_m P_m \approx 10$ to 100. Thus the number of required gridpoints in 3 dimensions is quite modest: $(L/l_k)^3 \approx 8000$. Such a calculation can certainly be managed by a desktop machine. However, for more realistic Prandtl numbers, say $P_m = 10^{-5}$, the resolution required becomes staggering: $(L/l_k)^3 \approx 10^{15}$. Accompanying this increased resolution comes an even tighter restriction on the allowable timestep. The relationship between the Reynolds number and the shortest timescale, the Kolmogorov timescale (τ_k) is: $R_e^{1/2} = (1/\tau_k)(U/L)$. The Kolmogorov timescale is roughly the turnover time for the smallest eddy, and U/L is the longest timescale, the turnover time for the system wide fluctuations. To witness the evolution of a fully nonlinear state for one complete system turnover time at $P_m = 10^{-5}$, we would need to step the MHD equations 10^4 times. Consequently, the complete calculation would require

N computations, where N = (6 field components)(10^4 timesteps)(10^{15} gridpoints) $\approx 10^{20}$. Even on a 100 Teraflop supercomputer, such as IBM's Blue Gene/L, this calculation would take months.

Fortunately, the situation is not hopeless. First of all, most of the time it is not imperative to resolve every timescale in the system. Nonlinear features of the bulk system behavior can be acquired without complete knowledge of microturbulence. For example, the magnetic fluctuations that are characteristic of MRI in low Prandtl number flows are too large and slow to sense the behavior of the tiny fluid fluctuations. Rather, they are more than likely coupled to the time-averaged bulk fluid flow. Thus, it may not be necessary to resolve seperate timescales completely. Second, as will be seen in this chapter, fully 3D simulations are not always necessary to model global behavior; sometimes the fundamentals can be captured in 2D. Third, the brute force method described in the preceding paragraph is not very sophisticated. Numerical techniques, such as adaptive mesh refinement, the use of hyperdiffusivities, global spectral and pseudospectral methods, etc, can dramatically reduce the number of required calculations. Finally, one can intelligently use limiting techniques to extrapolate from fully resolved calculations to partially resolved calculations. For example, the change in dynamics between an MHD fluid at $P_m = 0.1$ and $P_m = 0.01$ may be similar to the change between $P_m = 0.01$ and $P_m = 0.001$.

One can also make reasonable predictions of the types of specific numerical difficulties that may occur. In the context of MRI, these Reynolds number issues crop up in certain characteristic ways. Ekman circulation in MRI with endcaps is particularly difficult to resolve, as are the sharp boundary layers that develop near the walls due to the low fluid viscosity. We can estimate how the size of such boundary layers may scale with P_m. In a fully nonlinear stage, the smallest magnetic perturbations will be roughly of size $\Delta_b \sim (\frac{\eta}{\omega})^{1/2}$, where ω is some characteristic frequency in the system, such as the Alfvén frequency. Similarly, the smallest velocity perturbations will be of size $\Delta_v \sim (\frac{\nu}{\omega})^{1/2}$. If we keep η fixed and vary ν, Δ_v decreases while Δ_b stays the same. Thus we can roughly say that the approximate width of the smallest velocity fluctuation, such as in a boundary layer, scales like $P_m^{1/2}$. Figure 5.1 verifies this claim. Average nonlinearly driven radial profiles of V_θ over several values of P_m were generated using the spectral algorithm discussed in section 3.3,

and the boundary layer widths do exhibit this scaling.

In this chapter, we will present results obtained using the FD and spectral codes (see Chapter 3) to model axisymmetric (2D) MRI. Linear, quasilinear and fully nonlinear results will be discussed.

5.2 Linear Results

Armed with the dispersion relation described in Chapter 2, we were able to do a systematic search of the (R_m, S) plane to verify our two global codes' ability to model the linear phase of the MRI. In the case of the finite difference algorithm, we first applied initial low amplitude random perturbations to $B_{r,\theta,z}(r,z)$ and $V_{r,\theta,z}(r,z)$ with fixed background fields $\mathbf{B}_0 = B_z\hat{\mathbf{e}}_z$ and $\mathbf{V}_0 = r\Omega(r)\hat{\mathbf{e}}_\theta$. The system was allowed to evolve, and at each desired timestep, we performed a spatial decomposition of the perturbed fields into individual k_z-modes using the FFTW library [19]. We then were able to measure the growth rates of the perturbations by looking at a time trace of each mode amplitude separately and fitting them to an exponential. A sample time trace of three sample vertical eigenmode amplitudes, emergent under the appropriate conditions for expecting MRI, is shown in Figure 5.2. Note how the MRI is most unstable for the longest wavelength perturbation.

For four values of R_m, we swept across many values of S and measured growth rates. A sample scan is shown in figure 5.3 for $R_m = 360$. At this rotation rate, MRI destabilizes both the $kL/(2\pi) = 1$ and 2 eigenmodes. The solid curve is the dispersion relation's prediction for these modes' growth rates, and the markers were measurements from the initial value code output. The local dispersion relation prediction was fit to most accurately describe the behavior of the 2 longest wavelength perturbations simultaneously. It is likely that having made the local approximation causes the over- and underestimations of the growth rates. Better fits can be obtained when attempting to predict the behavior of a single mode.

Finally, from the measured onset and cutoff S values for each R_m sweep, we generated a stability boundary curve for $kL/(2\pi) = 1$, plotted in figure 5.4. Even with the local approximation, the local linear dispersion relation does a good job predicting the the global linear MRI behavior.

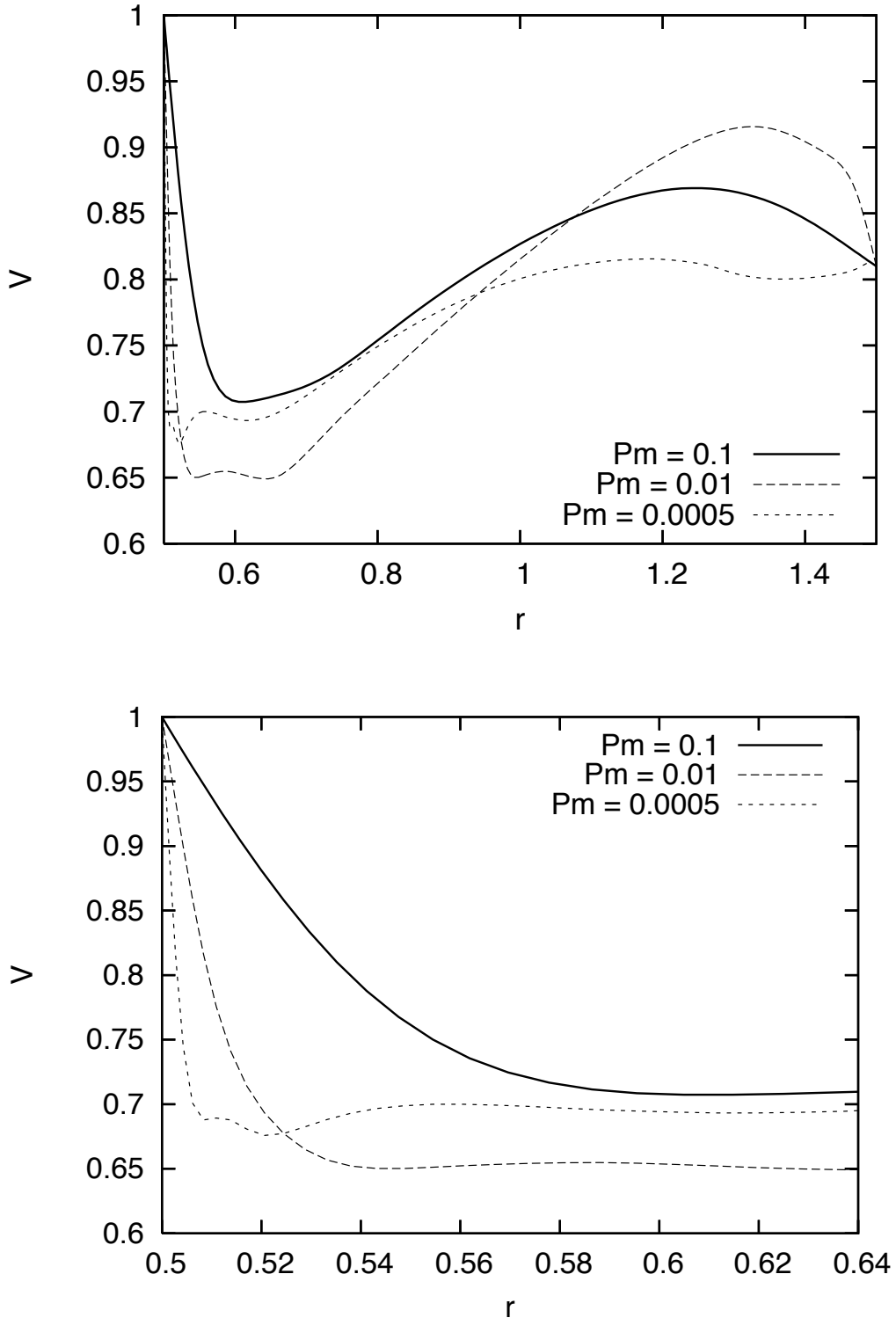

Figure 5.1: Upper: Profiles of $V_\theta(r)$ in a saturated MRI state for three different P_m values. Inner cylinder velocities normalized to unity, and $\mu = 0.27$. Below: Close-up near the inner wall shows resolution of boundary layers. The width of the velocity boundary layer, Δ_v, scales like $P_m^{1/2}$.

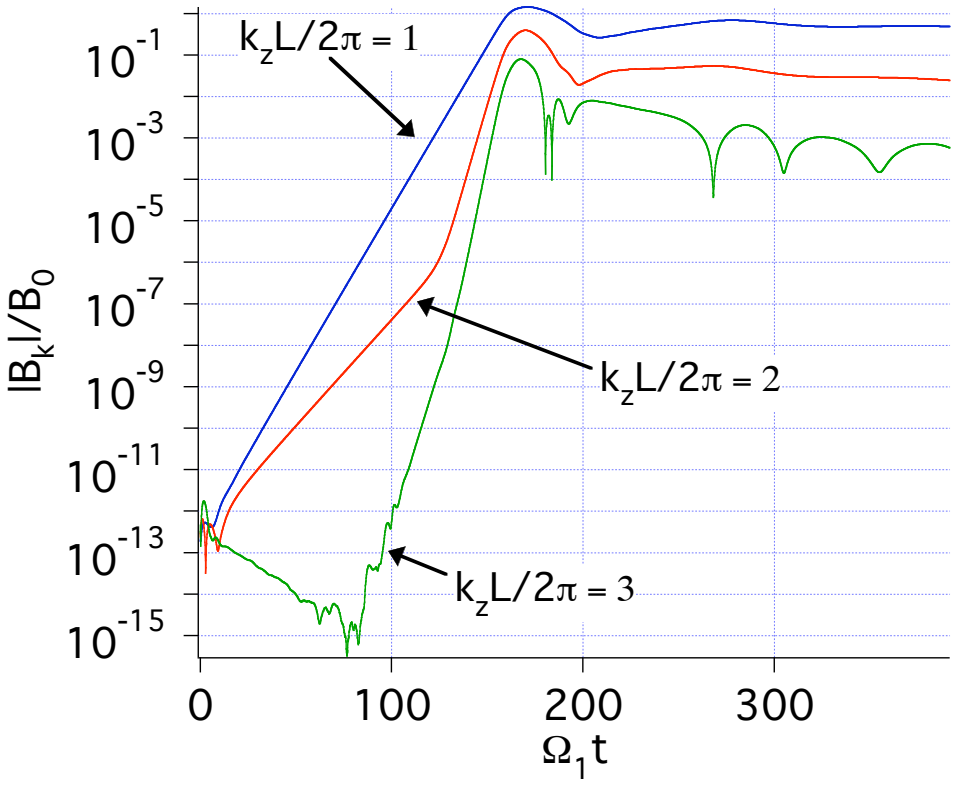

Figure 5.2: The 3 lowest vertical eigenmode amplitudes ($\frac{kL}{2\pi} = 1, 2$, and 3) are plotted versus time using the finite difference initial value code. The parameters in this run were $R_m = 360$, $S = 30$, $P_m = 0.1$, $a = 0.5$, $b = 1.5$, $L = 1$. Notice how k_1 and k_2 are both unstable for this set of parameters - the rotation rate of the inner cylinder is high enough to destabilize higher wavelength perturbations.

Also note that in benchmarking tests, the spectral code agreed with the FD result to within a percent.

5.3 Quasi-Linear Analysis

5.3.1 Review of Continuity equation

To gear ourselves up for a more complicated look at the transport properties within an MHD fluid, we will review the basic properties of the mass continuity equation (see Lighthill [22] for a more complete description). If we imagine a cube of volume $V = \delta x\, \delta y\, \delta z$ located at a fixed point in space inside a fluid, we observe that the net change in the mass enclosed by the cube is equal to the sum of the mass fluxes entering and leaving each face (see Figure 5.5). If we consider first just

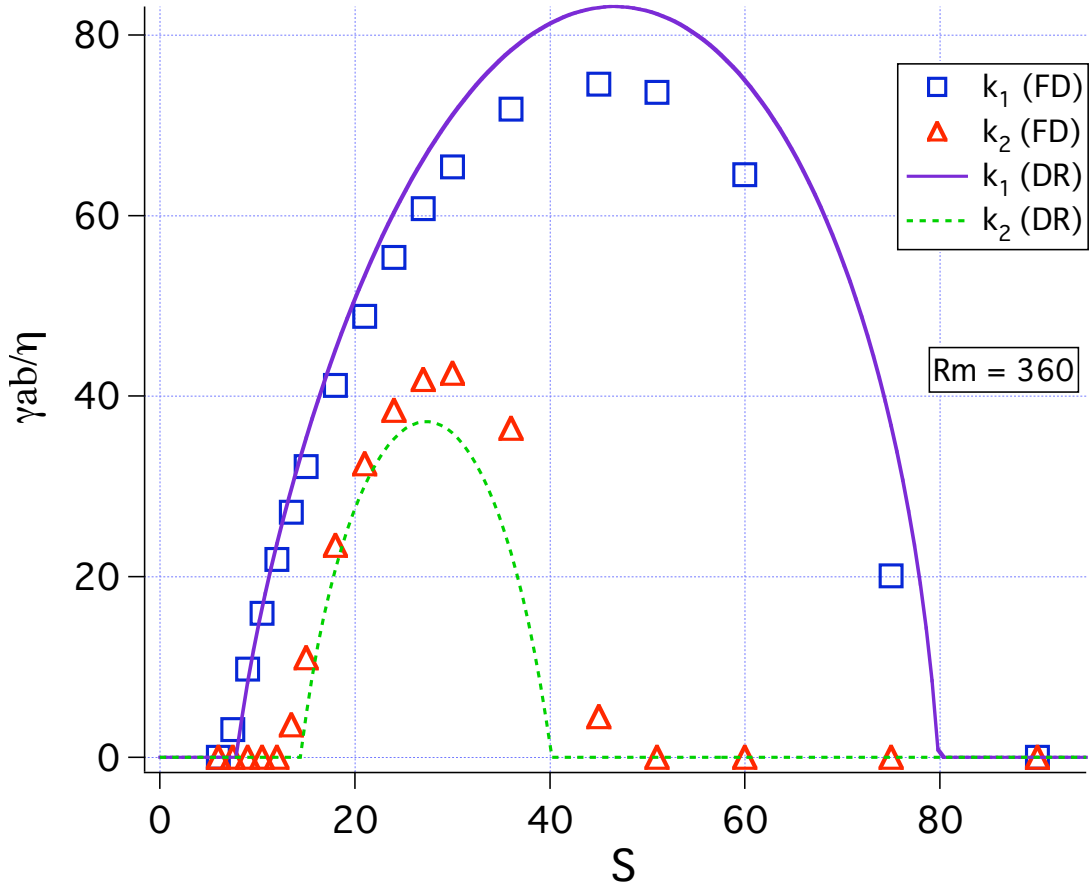

Figure 5.3: A sample sweep of S for a fixed R_m. The solid and dashed curves correspond to the full dispersion relation's prediction, using fit parameters $r_0 = 0.86$ and $\xi = 0.61$. These fit parameters were chosen to yield the best fit for both modes. The fit parameters were designed to yield a best fit for k_1 only.

one dimensional fluid flow in the x direction:

$$\frac{\partial m}{\partial t} = (\rho u_x)\,\delta y\,\delta z - (\rho u_{x+\delta x})\,\delta y\,\delta z \tag{5.1}$$

Since $m = \rho\,\delta x\,\delta y\,\delta z$, we can rewrite this as:

$$\frac{\partial \rho}{\partial t} = \frac{(\rho u_x) - (\rho u_{x+\delta x})}{\delta x} \tag{5.2}$$

Or, as $\delta x \to 0$,

$$\frac{\partial \rho}{\partial t} = -\frac{\partial(\rho u_x)}{\partial x} \tag{5.3}$$

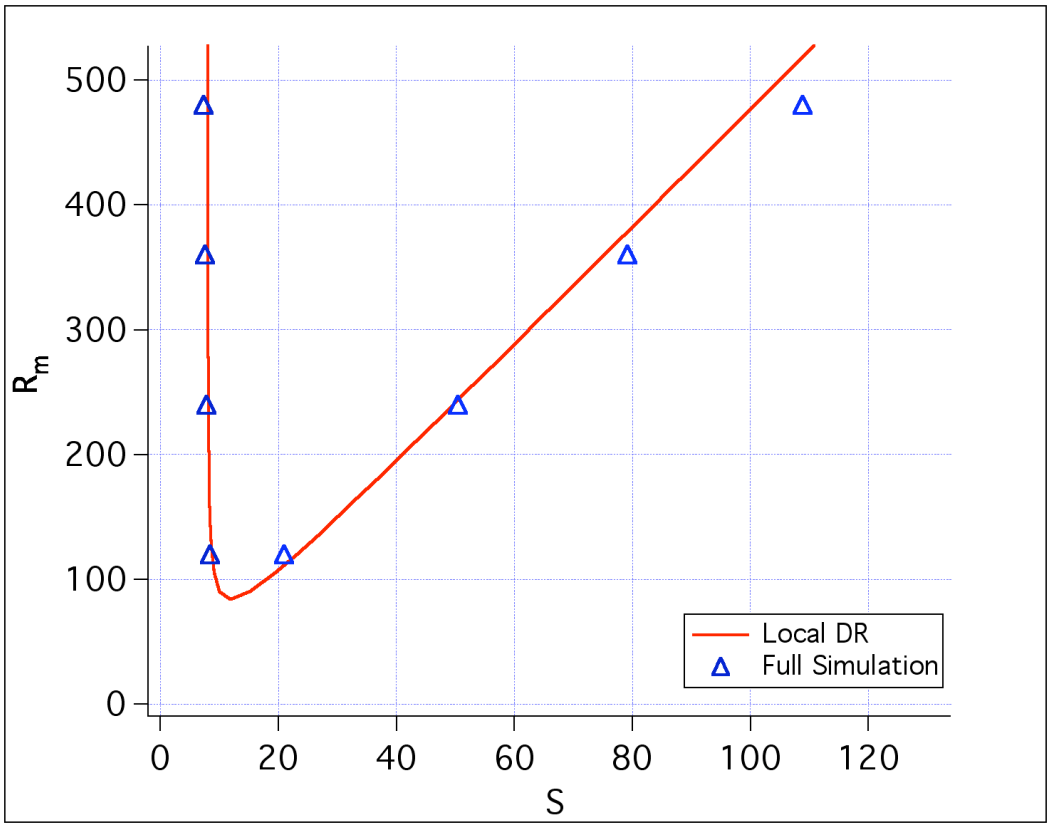

Figure 5.4: Marginal stability measurements. Solid curve is the dispersion relation.

A simple extension to three dimensions yields:

$$\frac{\partial \rho}{\partial t} = -\nabla \cdot (\rho \mathbf{u}) \tag{5.4}$$

This is commonly known as the mass continuity equation, or simply the continuity equation. In an incompressible fluid with constant density, *ie* $\nabla \cdot (\rho \mathbf{u}) = 0$, as the fluids we are analyzing in this document typically are, this equation becomes trivial. However, when we analyze the transport of angular momentum in an ideal magnetized fluid (next section), we will arrive at an equation with the same structural form as 5.4, so it is useful to understand its implications.

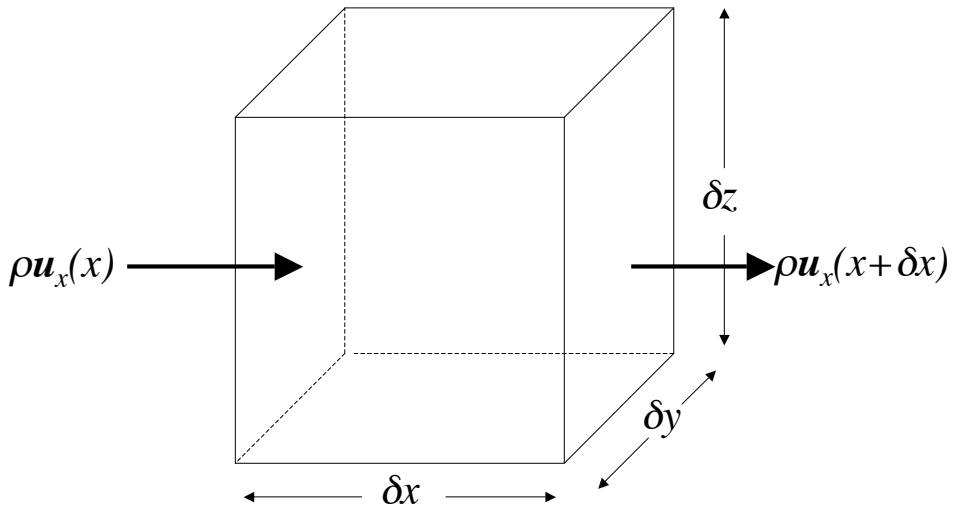

Figure 5.5: Simple model of the mass continuity equation. The change in density inside the box is equal to the total mass flux in and out the box.

5.3.2 $R-\theta$ stresses and Angular momentum transport

Consider the momentum equation for an incompressible fluid in the presence of a background magnetic field (negligible viscosity, $\nu = 0$) [23]:

$$\frac{\partial(\rho\mathbf{U})}{\partial t} + \nabla \cdot [\rho\mathbf{U}\mathbf{U} + \underline{\underline{\mathbf{P}}} + \frac{1}{2\mu_0}B^2\underline{\underline{\mathbf{I}}} - \frac{1}{\mu_0}\mathbf{B}\mathbf{B}] = 0 \tag{5.5}$$

We want to manipulate this to be an equation defining the evolution of angular momentum ($L_z = \rho U_\theta$). To do this, take $\hat{z} \cdot \mathbf{r} \times$(Equation 5.5). I will also take this opportunity to define the Reynolds and Maxwell stress tensors, $\underline{\underline{\mathbf{T}}}_{Rey}$ and $\underline{\underline{\mathbf{T}}}_{Max}$:

$$\frac{\partial L_z}{\partial t} + \hat{z} \cdot \mathbf{r} \times \nabla \cdot [\underline{\underline{\mathbf{T}}}_{Rey} + \underline{\underline{\mathbf{T}}}_{Max}] = 0 \tag{5.6}$$

To complete this equation, we need only know only the theta-components of the stress tensor divergences.

$$\frac{1}{\rho}[\nabla \cdot \underline{\underline{\mathbf{T}}}_{Rey}]_\theta = \frac{1}{r}\frac{\partial}{\partial r}(rU_rU_\theta) + \frac{1}{r}\frac{\partial U_\theta^2}{\partial \theta} + \frac{\partial U_zU_\theta}{\partial z} + \frac{1}{\rho r}\frac{\partial P}{\partial \theta} + \frac{U_rU_\theta}{r} \tag{5.7}$$

or, put more simply:

$$\frac{1}{\rho}[\nabla \cdot \underline{\underline{\mathbf{T}}}_{Rey}]_\theta = \nabla \cdot \mathbf{U}U_\theta + \frac{1}{\rho r}\frac{\partial P}{\partial \theta} + \frac{U_rU_\theta}{r} \tag{5.8}$$

A similar calculation for the Maxwell stress tensor yields:

$$\mu_0[\nabla \cdot \underline{\underline{\mathbf{T}}}_{Max}]_\theta = -\nabla \cdot \mathbf{B}B_\theta + \frac{1}{r}\frac{\partial}{\partial \theta}\frac{B^2}{2} - \frac{B_rB_\theta}{r} \tag{5.9}$$

Combining these calculations with equation 5.6:

$$\frac{\partial L_z}{\partial t} + \nabla \cdot [\rho r U_\theta \mathbf{U} - \frac{r}{\mu_0}B_\theta \mathbf{B} + r(\frac{B^2}{2\mu_0} + P)\hat{\theta}] = 0 \tag{5.10}$$

This can be viewed as a continuity equation for L_z, similar to the mass continuity equation, 5.4. We are primarily interested in the total radial flux of angular momentum, so we wish to average equation 5.10 over z and θ. For convenience, let us also define the vector

$$\overrightarrow{\phi} \equiv \rho r^2 \Omega \mathbf{U} - \frac{r}{\mu_0}B_\theta \mathbf{B} + r(\frac{B^2}{2\mu_0} + P)\hat{\theta}. \tag{5.11}$$

Integrating equation 5.10:

$$\begin{aligned}\int\int r\,d\theta\,dz\frac{\partial L_z}{\partial t} &= -\int\int r\,d\theta\,dz\nabla \cdot \overrightarrow{\phi} \\ &= -\int\int r\,d\theta\,dz\left\{\frac{1}{r}\frac{d}{dr}(r\phi_r) + \frac{1}{r}\frac{d}{d\theta}\phi_\theta + \frac{d}{dz}\phi_z\right\}\end{aligned} \tag{5.12}$$

The last term in equation 5.12 is a perfect derivative in z, so it vanishes upon integration. The azimuthal derivative before it vanishes if we assume axisymmetry. Therefore,

$$\begin{aligned}\int\int r\,d\theta\,dz\frac{\partial L_z}{\partial t} &= -\int\int r\,d\theta\,dz\,\frac{1}{r}\frac{d}{dr}(r\phi_r)\\ &= -\frac{d}{dr}\int\int d\theta\,dz\,(r\phi_r)\\ &= -\frac{d}{dr}\int\int r\,d\theta\,dz\left\{\rho r(U_\theta U_r) - (V_{A\theta}V_{Ar})\right\}\end{aligned} \tag{5.13}$$

Defining a column averaged density, $\Sigma \equiv \rho L 2\pi r$ (where L is the system height, not to be confused with L_z), we can finally write:

$$\frac{\partial < L_z >_{z,\theta}}{\partial t} = -\frac{d}{dr}\left\{\frac{r\Sigma}{2\pi L}(< U_\theta U_r >_{z,\theta} - < V_{A\theta}V_{Ar} >_{z,\theta}\right\} \tag{5.14}$$

We can interpret the quantity inside the braces in the above equation to be the radial flux of angular momentum as a function of r alone:

$$\Phi_r(r) \equiv r\frac{\Sigma}{2\pi L}(< U_\theta U_r >_{z,\theta} - < V_{A\theta}V_{Ar} >_{z,\theta}) \tag{5.15}$$

This quantity can be used as a diagnostic to measure the rate of angular momentum transported through the fluid, and the relative degree to which the fluid and magnetic fluctuations are responsible for this transport. We implemented this diagnostic in the FD code, and in Figure 5.6, we plotted multiple snapshots of $< V_{A\theta}V_{Ar} >_{z,\theta}$ profiles (the Maxwell stress tensor component of angular transport). Loosely, this can be understood as the rate of angular momentum transport via magnetic perturbations. Note how for all times, this quantity is negative, which from equation 5.15 can be understood as outward transport. The interpretation that the MRI perturbations serve to transport angular momentum outward in the bulk of a differential flow is consistent with this analysis.

$\Phi_r(r)$, however, represents the radial flux of angular momentum for an idealized system, free of dissipation. If we include the effects of dissipation, we must add a term to the RHS of

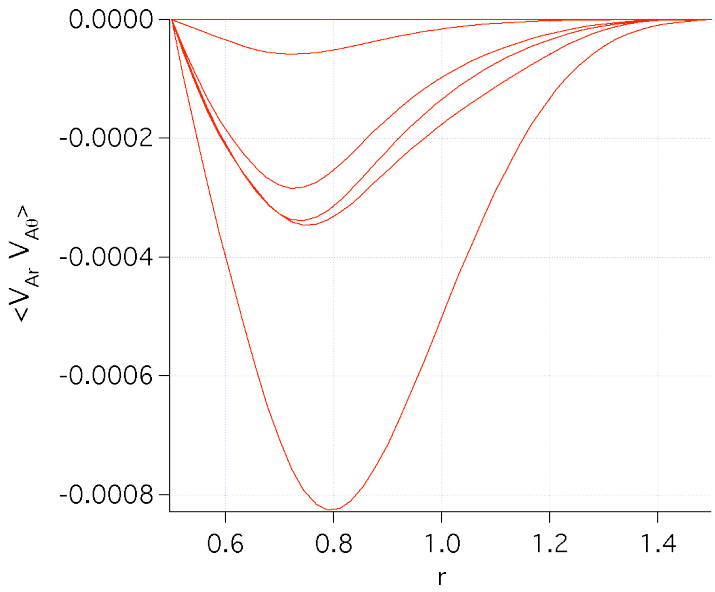

Figure 5.6: Snapshots of the radial flux of angular momentum via magnetic perturbations, taken at various times in the linear and nonlinear stages of a flow destabilized to MRI. That the Maxwell stress contribution to $\Phi_r(r)$, $< V_{A\theta} V_{Ar} >_{z,\theta}$ (equation 5.15), is negative at all times indicates that MRI magnetic pertubations transfer angular momentum outward.

equation 5.6:

$$\frac{\partial L_z}{\partial t} + \hat{z} \cdot \mathbf{r} \times \nabla \cdot [\underline{\underline{\mathbf{T}}}_{Rey} + \underline{\underline{\mathbf{T}}}_{Max}] = \hat{z} \cdot \mathbf{r} \times [\nu \nabla^2 (\rho \mathbf{U})] \tag{5.16}$$

When we average over θ and z as we did before, we now get:

$$\begin{aligned} \frac{\partial < L_z >_{z,\theta}}{\partial t} + \frac{d}{dr}\Phi_r(r) &= \nu \int\int r\rho \, d\theta \, dz \left\{ \frac{1}{r} \frac{d}{dr} (r \frac{d}{dr} U_\theta) \right\} \\ &= \frac{d}{dr} \frac{\Sigma}{2\pi L} < r\nu \frac{d}{dr} U_\theta >_{z,\theta} \end{aligned} \tag{5.17}$$

The new term on the RHS corresponds to viscous transport of angular momentum, which is especially important near the inner and outer boundaries, where the radial derivatives of U_θ are the largest.

If we integrate equation 5.17 over r, we get the equation for total angular momentum conservation:

$$\int dr \, \frac{\partial}{\partial t} < L_z >_{z,\theta} = S_{source} - S_{sink} \tag{5.18}$$

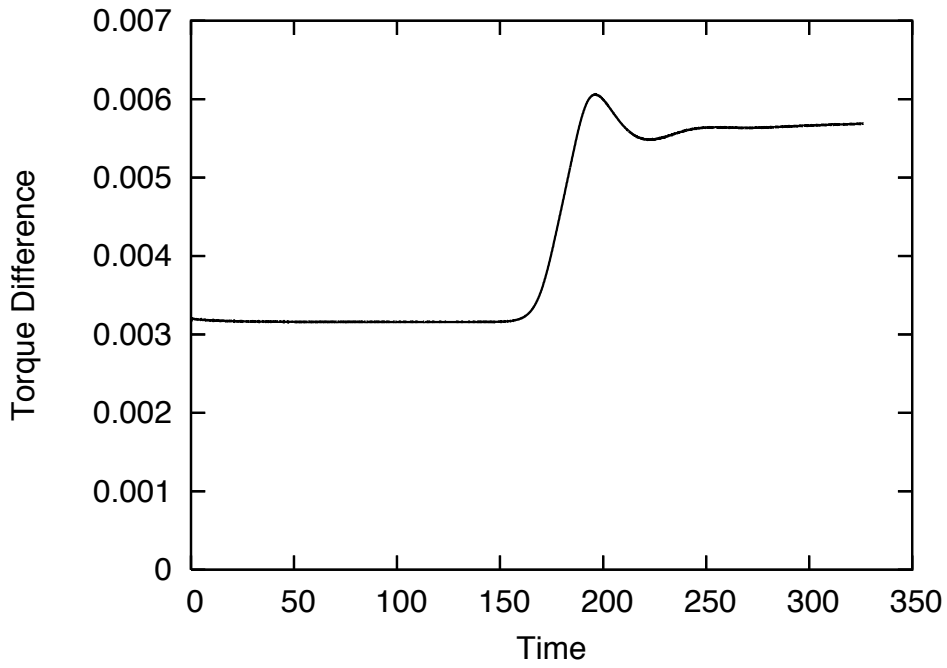

Figure 5.7: Difference in torques at the inner and outer walls, *i.e.*, $\tau_1 - \tau_2$, which is proportional to the rate of angular momentum transfer within the fluid. The MRI causes a dramatic increase in the transport of angular momentum within the fluid.

where S_{source} represents the angular momentum injected by the torque on the fluid by the inner wall, and S_{sink} represents the angular momentum dissipated by the torque on the outer wall by the fluid.

Thus, we can view at the difference in torques on the inner and outer walls by the fluid as a measure of the total angular momentum transported by the fluid! This simple result is useful, and plotted in figure 5.7 clearly demonstrate that the instability is transporting angular momentum to larger radii.

5.4 Nonlinear Results

5.4.1 Magnetic saturation level

One of the more important nonlinear questions of MRI concerns the saturation mechanism, and the level at which the magnetic perturbations become saturated. This is something that is currently not very well understood in either an astrophysical context or a laboratory context. Simulations

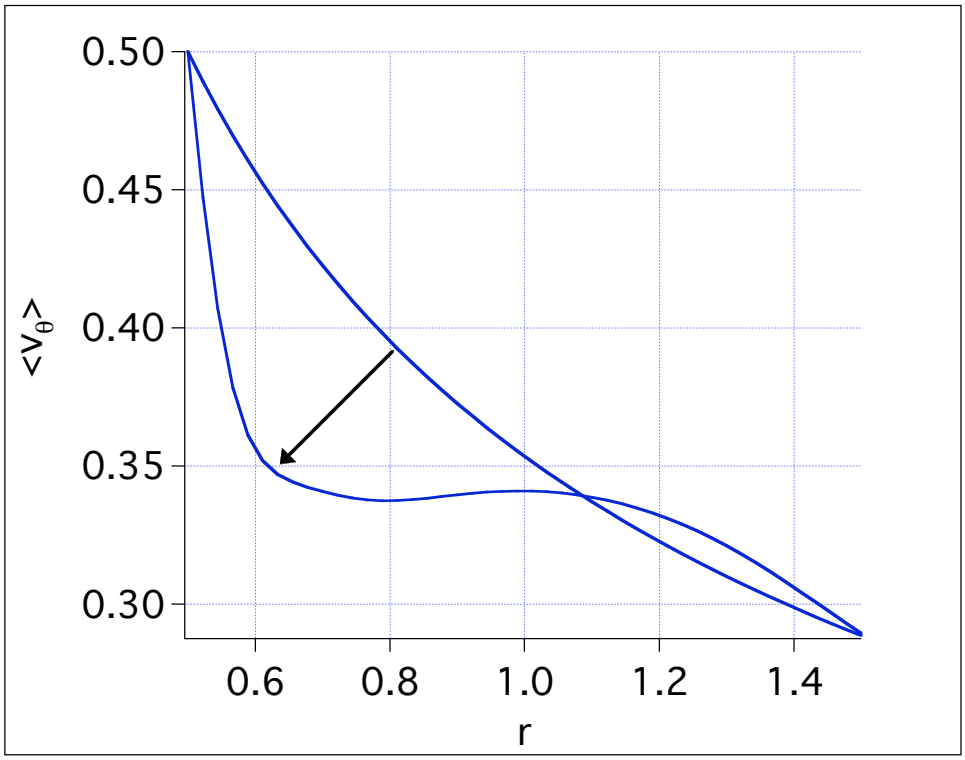

Figure 5.8: Perturbed magnetic fields can only extract so much rotational energy from the system before the profile relaxes and MRI saturates. The total change in rotational energy between this initial Couette and final saturated profile is 10%. This is consistent with laboratory results, where the excited fields saturate at a low level.

indicate that perturbed magnetic fields can only extract so much rotational energy from the system before the flow profile relaxes and the MRI saturates. Figure 5.8 shows such a profile, $V_\theta(r)$, relaxing from Couette flow (initial) to some final nonlinear state (nonlinear FD code computation). A portion of this rotational energy must go into the magnetic field perturbations, so we wish to characterize the energy budget before and after saturation.

To diagnose how much energy is being consumed by the unstable magnetic perturbations (and from where it is coming), it is necessary to keep track of how the total energy in the system is being allocated at each time step. First of all, let's look at a time trace of the total energy in the system, $E_{rot} + E_{mag}$, which is plotted in Figure 5.9. Note that some of the energy in the system is dissipated by viscous drag, particularly around the time of saturation, when the velocity gradients near the boundaries become sharp. We can extract from this Figure the amount of energy lost between the linear phase and just after saturation, E_{diss}. In this run, $E_{diss} = 0.0026$.

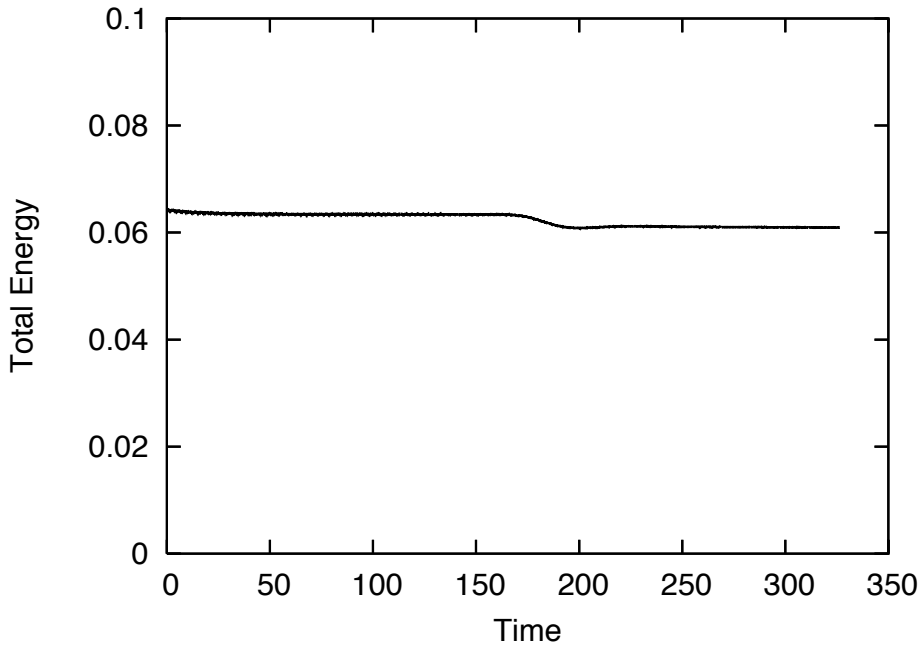

Figure 5.9: Time trace of the total energy in the system, $E_{rot} + E_{mag}$, for an MRI simulation with the following parameters: $a = 0.5, b = 1.5, L = 1, R_m = 100, S = 12$, and $P_m = 0.1$. During this run, a Keplerian profile ($\Omega \propto r^{-3/2}$) was initialized. Note that Energy is not conserved - some is dissipated by viscous drag, particularly around the time of saturation, when the velocity gradients near the boundaries become sharp.

Plotted in Figure 5.10 are time traces of the total rotational energy in the system, $< U_\theta^2 >$, and the total energy contained within the magnetic fields, $< B^2 >$. We can read off from this plot the amount of rotational energy extracted from the system: $E_{rot} = 0.0031$. Similarly, the amount of energy gained by the magnetic fields is $E_{mag} = 0.00066$. This demonstrates that all the energy is properly accounted for, since $E_{rot} - E_{diss} \approx E_{mag}$ (It is actually slighly greater, because the inner wall is a source of rotational energy). The rotational energy lost in the system is therefore passed out to the unstable magnetic fields and the dissipation. However, it should be noted that the magnetic energy in the system never really becomes comparable to the rotational energy.

This prompts a question - How much field amplification can one hope to observe when observing MRI in a laboratory setting? In the ideal case of a cylinder and a perfect non-turbulent initial state, the magnitude of the background axial field component outside the apparatus would be extremely large compared to the infinitesimal perturbed field components. For the sake of

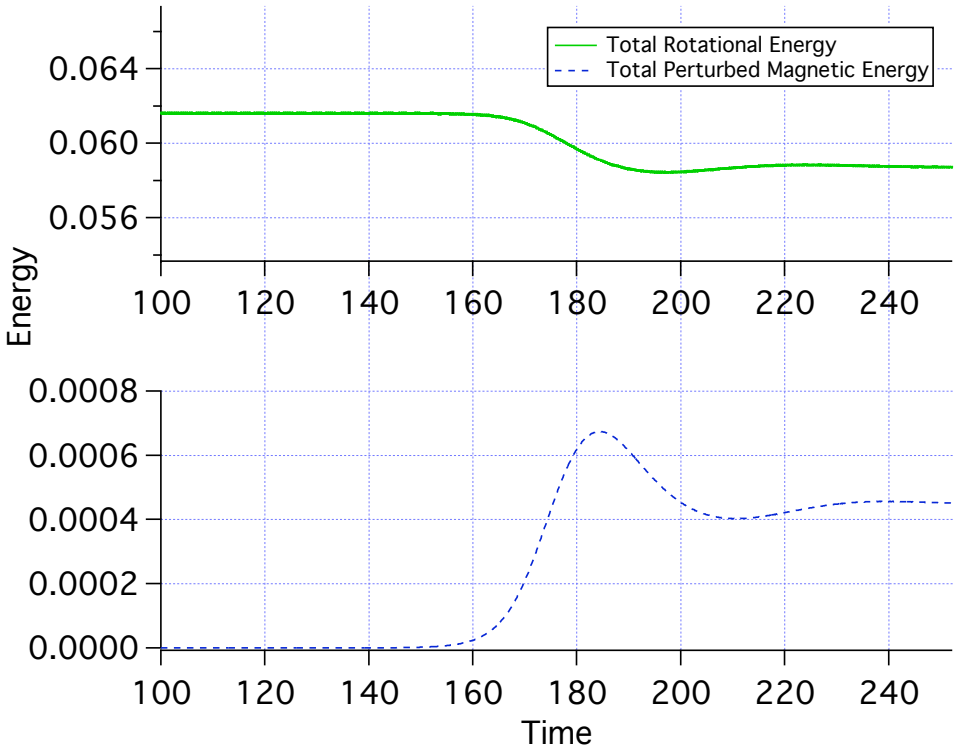

Figure 5.10: Simulations show that $< \delta V_A^2 >$ reaches only a few percent of $< V_\theta^2 >$, although this appears to be a function of R_m, S, P_m and geometry.

argument, let us assume that in the laboratory, it is difficult to observe field fluctuation magnitudes much smaller than the background field. What then kind of amplification of the magnetic field might one then expect to see? If we can roughly measure the amplitude of magnetic field amplification by tracking the magnitude of $< B^2 >^{1/2}$, then we can see from Figure 5.11 that the amplification is only about $M = 1.17$.

In the experiment conducted by Sisan, *et al*, they answer the question by measuring fluctuating field amplitudes and comparing them to the background field strength. The answer seems to be that after the primary instability sets in, the fluctuating fields oscillate at approximately 1 % of the background field (compared to 0.1% with no instability) [9]. In the simulation described above, we measured $< \delta B_r^2 + \delta B_\theta^2 + \delta B_z^2 >^{1/2} / B_z$ after saturation and found that the perturbed fields amplified to about 35% of B_z.

Naturally, the most significant differences between our simulation and experiment is are the geometry and the Prandtl number. The amplification could certainly depend on Prandtl

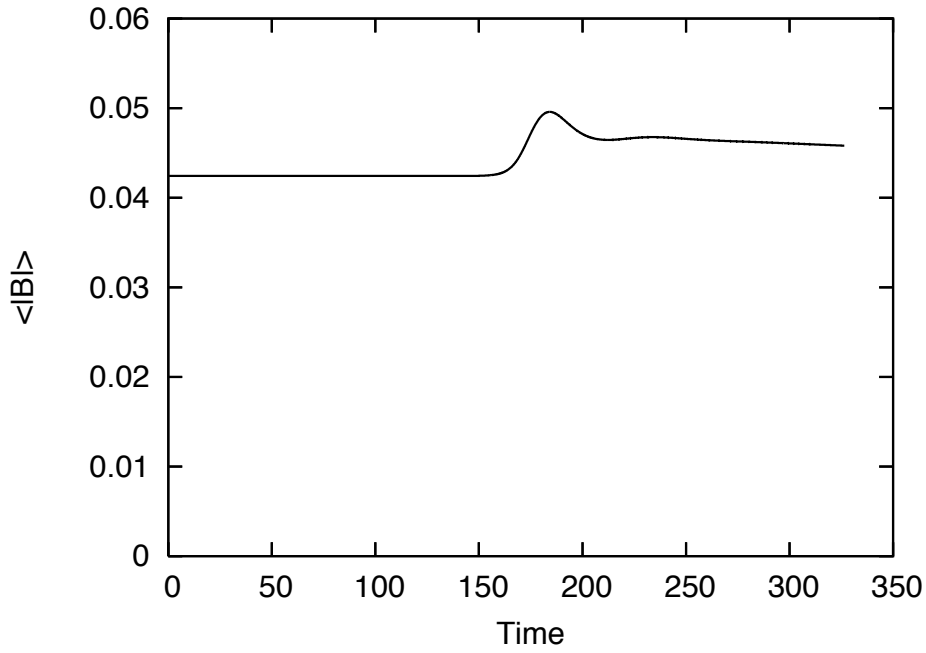

Figure 5.11: The magnitude of $< B^2 >^{1/2}$ as a function of time. The amplification of total field strength in the system is only $M = 1.17$.

number, and indeed, with higher magnetic resistivity, one may expect this percentage to fall (more supression of magnetic fluctuations). To this end, we also employed the Spectral algorithm, which is more suited to higher Reynolds number computations, to measure this saturation amplitude as a function of Prandtl number. Results are plotted in Figure 5.12. Note that at higher P_m viscosity stabilizes MRI, and as P_m decreases, the saturation amplitude decreases, as predicted.

5.4.2 Post-saturation nonlinear behavior

The structural form of the perturbed magnetic field prior to saturation is one we will refer to as magnetically induced taylor vortices. Post saturation, they are slightly warped by nonlinear interactions, but the fundamental structure remains the same. Figure 5.13 is a depiction of this saturated structural form. These results are consistent with nonlinear simulations conducted by Wolfgang Dobler [24].

It has been demonstrated in simulations that the late nonlinear behavior may look very

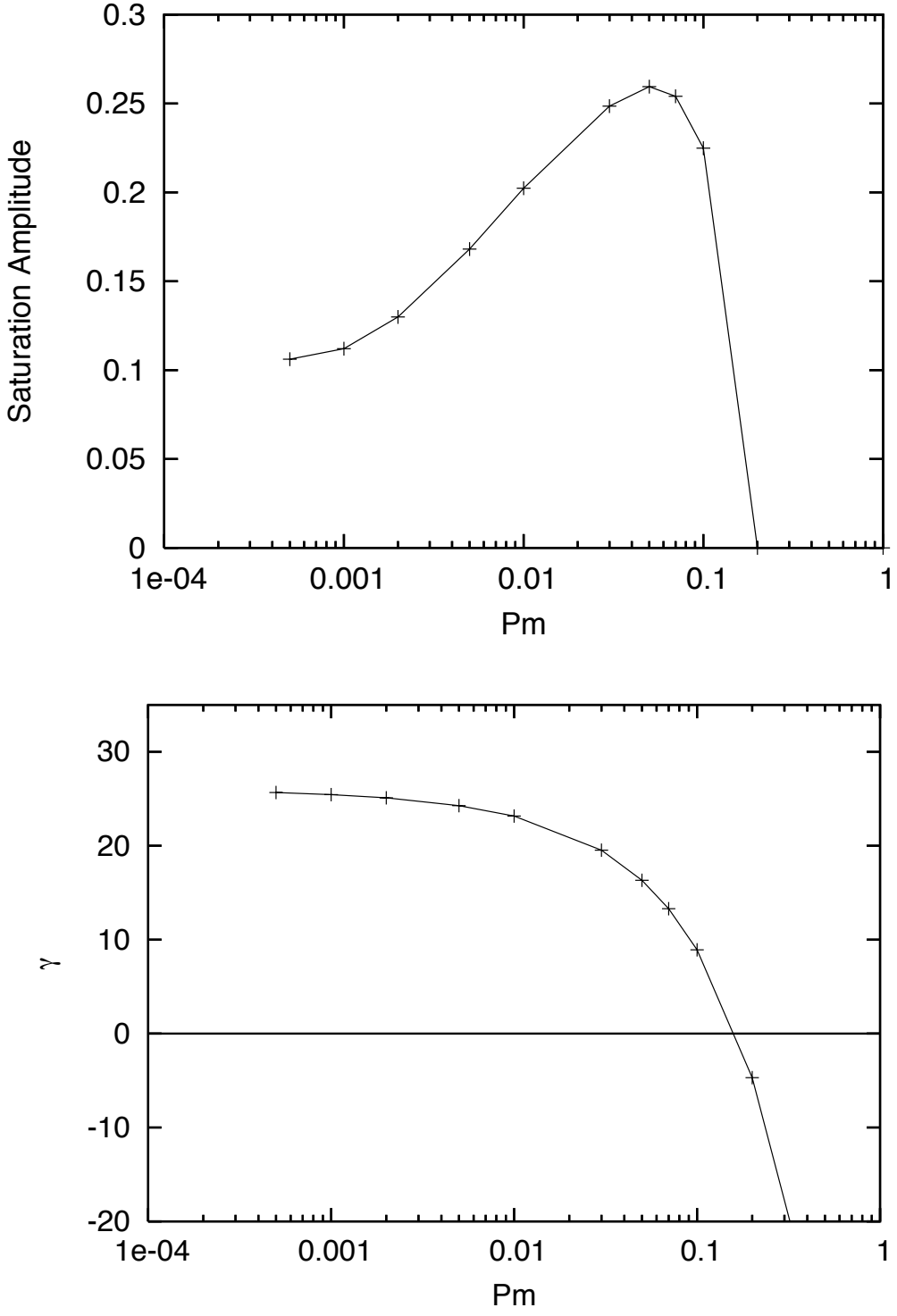

Figure 5.12: *Upper* :$< |\boldsymbol{\delta B}| > /B_z$ vs. time, where $< |\boldsymbol{\delta B}| >$ is the magnitude of the perturbed field strength averaged over the domain. This is a measure of the saturation amplitude of MRI as a function of P_m, keeping η fixed. Note that at higher P_m viscosity stabilizes MRI, and as P_m decreases, the saturation amplitude decreases. Lower: Linear growth rates (normalized to $\omega_d = \eta/L^2$) for the same set of runs. Growth rates are reduced with increasing viscosity.

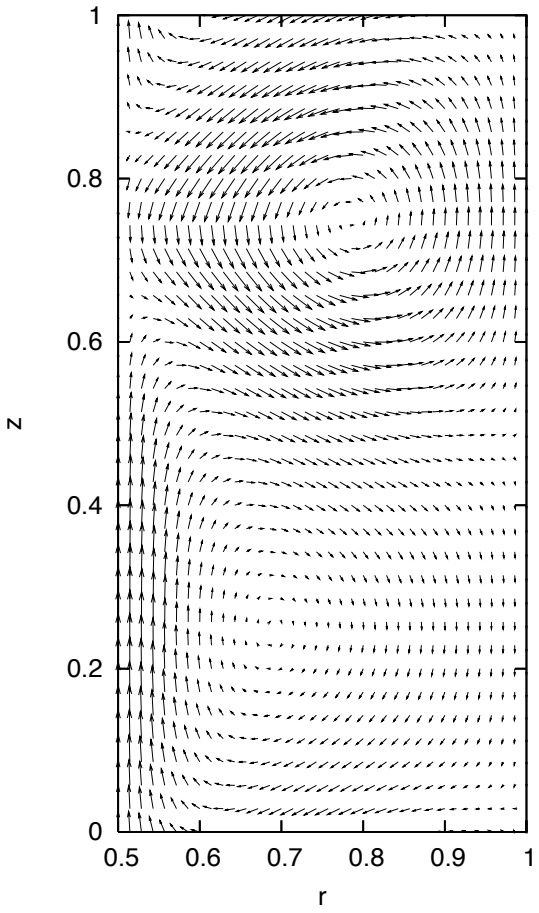

Figure 5.13: Perturbed magnetic vector fields just after MRI saturation for $a = 0.5, b = 1, \Omega_1 = 2, \mu = 0.35, B_0 = 0.2, L = 1, P_m = 1$, and $\nu = 7 \times 10^{-4}$. These structural forms are characteristic of magnetic taylor vortices, although they are slightly warped by nonlinear interactions.

different from the predictions made by linear theory [24]. As an example of this point, see the time traces of the first three the vertical eigenmode amplitudes in Figure 5.14. The initial saturated structure is one clearly dominated by the longest wavelength axial mode, but the system state clearly changes dramatically long after linear saturation. Hypothetically casting this as an actual experiment, the observed state after onset of MRI would likely not be that at $\Omega_1 t \approx 200$, but could be much later. Consequently, MRI in the lab may not "look" like the predictions from linear theory. A more dramatic example of this surprising nonlinear behavior will be presented in section 7.2, where an axisymmetric saturated MRI state itself becomes subject to a secondary nonaxisymmetric instability, and the late nonlinear behavior is drastically altered.

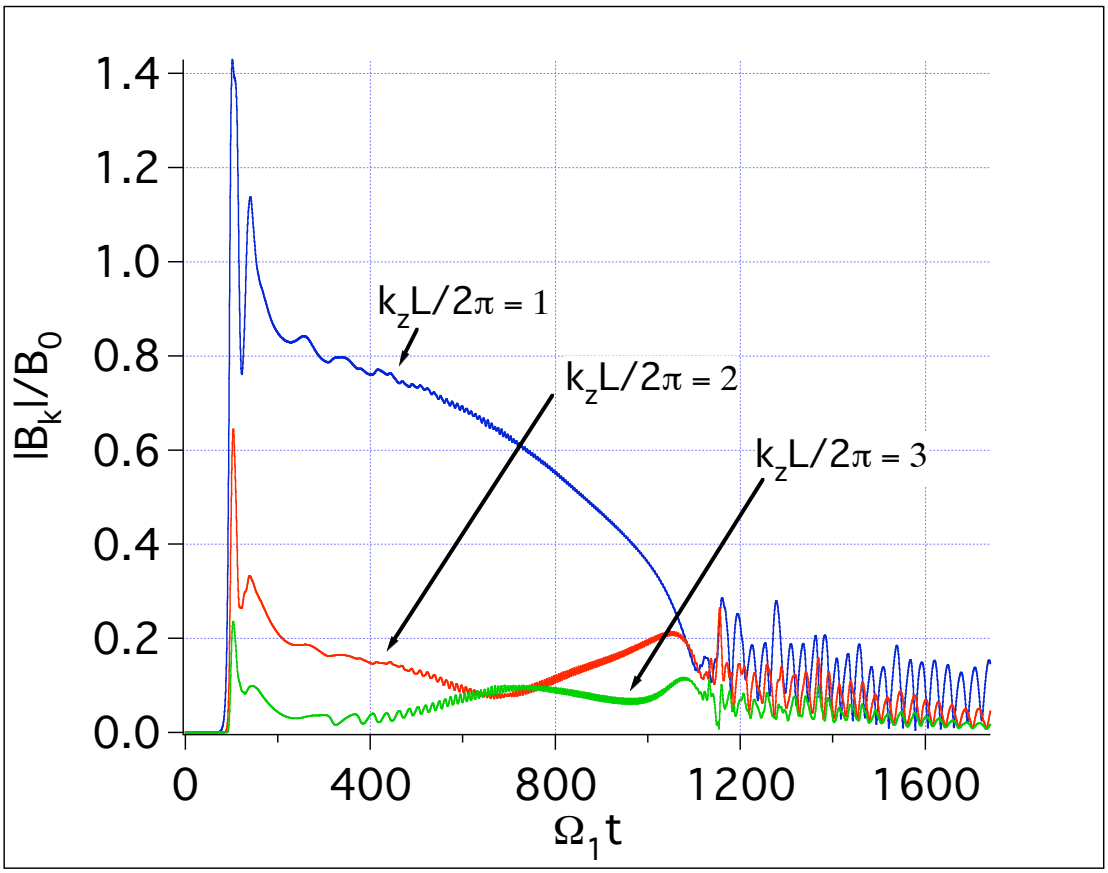

Figure 5.14: Time behavior of the first three vertical eigenmodes - $\frac{kL}{2\pi} = 1$ (blue), 2 (red), and 3 (green). Note how the system state changes dramatically long after linear saturation at $\Omega_1 t \approx 100$.

Chapter 6

MRI with toroidal fields

In the local linear analysis of chapter 2, we assumed that the applied background field was purely axial ($\mathbf{B}_z = B_0\mathbf{e}_z$). In this chapter, we will allow for the possibility of an additional background azimuthal magnetic field of the form:

$$\mathbf{B}_\theta = \beta B_0 \frac{r_0}{r}\mathbf{e}_\theta \tag{6.1}$$

where the relative magnitude of the axial and toroidal components at some characteristic radial value, r_0, is parametrized by β. Hollerbach, *et al* have demonstrated that adding such a background field can dramatically reduce Rm_{crit}, the minimum magnetic Reynolds number required for destabilizing a system to MRI [12], [10]. Such a toroidal field's origin is simple to imagine: an axially oriented current carrying wire placed at $r = 0$ would produce such a field. In this chapter, we will attempt to characterize this effect, and comment on its potential experimental applicability.

6.1 Local Linear DR prediction

In chapter 2, we made a local approximation to the matrix equation 2.15 and came up with an equation for marginal stability in the inviscid limit (equation 2.17). We did this for $\beta = 0$, *ie* no background toroidal magnetic field. If we allow for nonzero values of beta, then the matrix equation, 2.15, becomes:

$$\begin{pmatrix} \gamma - \eta D^2 & 0 & -\omega_A & 0 \\ -\zeta\Omega & \gamma - \eta D^2 & -\frac{2i\omega_A\beta r_0}{kr^2} & -\omega_A \\ (2 + \frac{D^2}{k^2})\omega_A & \frac{2i\omega_A\beta r_0}{kr^2} & \gamma - \nu D^2 - \frac{1}{k^2}(D^2 + k^2)(\gamma + \nu D^2) & -2\Omega \\ 0 & \omega_A & \xi\Omega & \gamma - \nu D^2 \end{pmatrix} \begin{pmatrix} \beta_r \\ \beta_\theta \\ \varphi_r \\ \varphi_\theta \end{pmatrix} = 0 \tag{6.2}$$

The matrix is identical to the case where a purely axial field was applied, except for the addition of the 2 terms involving β, matrix elements (2,3) and (3,2). Note that these terms also contain a factor of $i = \sqrt{-1}$, meaning that they are phase shifted 90° from the others. This phase shift has an important consequence. After the local approximation is applied (section 2.1), one can no longer simply solve for the marginal stability boundary, $Rm(S)$ (equation 2.17), since marginal solutions (zero growth rate) to the equation 3.1 no longer require that $\gamma = 0$, simply that Re[γ] $= 0$. Thus, at marginal stability, it is not a requirement that the real frequency of the MRI mode be zero. In fact, this is a generic consequence of the addition of a toroidal field; the up-down symmetry of the system is destroyed. For $\beta = 0$, neither propagation direction is preferred, but as β increases, there is a region in the (Rm, S) plane where the wave moving in the $+z$ direction is damped while the wave moving in the opposite direction is unstable. This result is consistent with Hollerbach, *et al* [12].

Of more interest, however, is how the critical value of R_m decreases dramatically as β increases. This can be clearly seen in Figure 6.1, where for $\beta = 0$, $Rm_{crit} \approx 10$ and for $\beta = 4$, $Rm_{crit} \approx 10^{-4}$. This is a dramatic shift, and its implications on observing MRI in the laboratory are significant. As discussed in Chapter 1, one of the most significant drawbacks to using liquid metal to observe MRI is the vast separation of the viscous and diffusive timescales. For typical liquid metals, $P_m = \frac{\nu}{\eta} \approx 10^{-6}$, so if the observation of MRI requires $R_m \approx 10 - 100$, the corresponding Reynolds number of the flow is enormous: $R_e \approx 10^7$. However, if one were able to observe MRI at a much lower magnetic Reynolds number, say $R_m \approx 0.01$, the flow would be less likely to suffer the contamination of end effects, boundary layers and other high Reynolds number phenomena.

One may consequently wonder if a toroidal field alone is enough to destabilize axisymmetric MRI (no axial field, *ie* $\beta \to \infty$). It turns out that it is not - an axial field is required. For an analytical proof of this statement, see Herron, *et al* [25].

Figure 6.2 gives a sense of how Rm_{crit} depends on β for a range of Prandtl numbers. In the inviscid limit ($P_m = 0$), the critical magnetic Reynolds number drops to zero at some critical

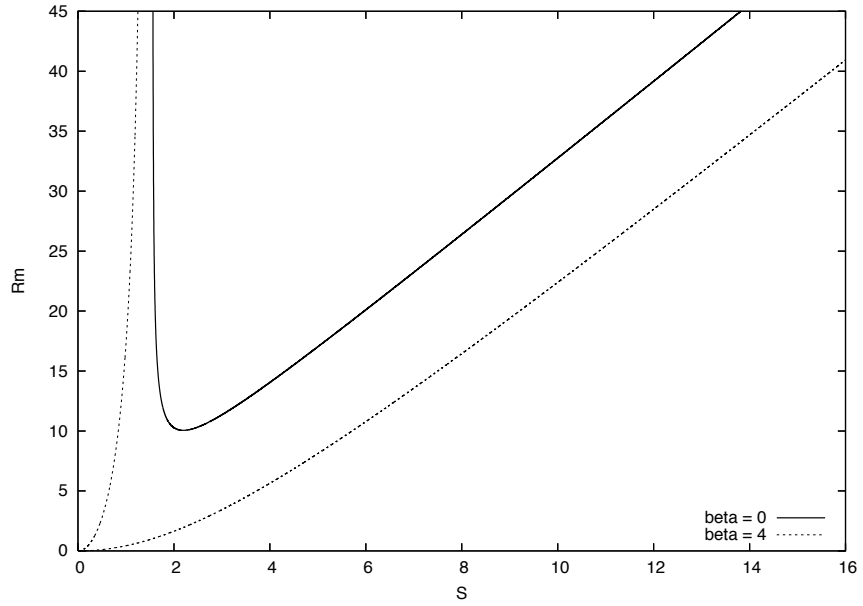

Figure 6.1: Marginal stability curves (derived from a nondimensionalized version of equation 6.2 with Re[γ]= 0), with the following parameters (introduced in Chapter 2): $r_0 = 1.5$, $L = 2.7$, $kL = 2\pi$, $P_m = 10^{-5}$ and $\xi = 0.115$. The two curves represent the 2 cases, $\beta = 0$ and the more unstable $\beta = 4$ root (without and with a toroidal field component, respectively).

.

value of β. For higher Prandtl numbers, there is a sharp drop, but finite viscosity places a limit on how low Rm_{crit} can get.

By what mechanism does this dramatic crash occur? We diagnosed the influence of each term containing β in the matrix equation 2.15 by multiplying them by dummy coefficients, adjusting these coefficients between 0 and 1, and measuring Rm_{crit} in each case. It turns out that the coupling of the radially perturbed velocity field, δu_r, to the background toroidal magnetic field does most of the work in dropping Rm_{crit} orders of magnitude (this comes from the $\nabla \times \mathbf{u} \times \mathbf{B}$ term in the induction equation). The coupling of the perturbed and background toriodal magnetic fields from the $\nabla \times \mathbf{B} \times \mathbf{B}$ term in the momentum equation plays much less of a role.

That the flow profile is important for this effect to emerge should become obvious from Figure 6.3, where critical Reynolds number is plotted against ξ for different values of β. Notice

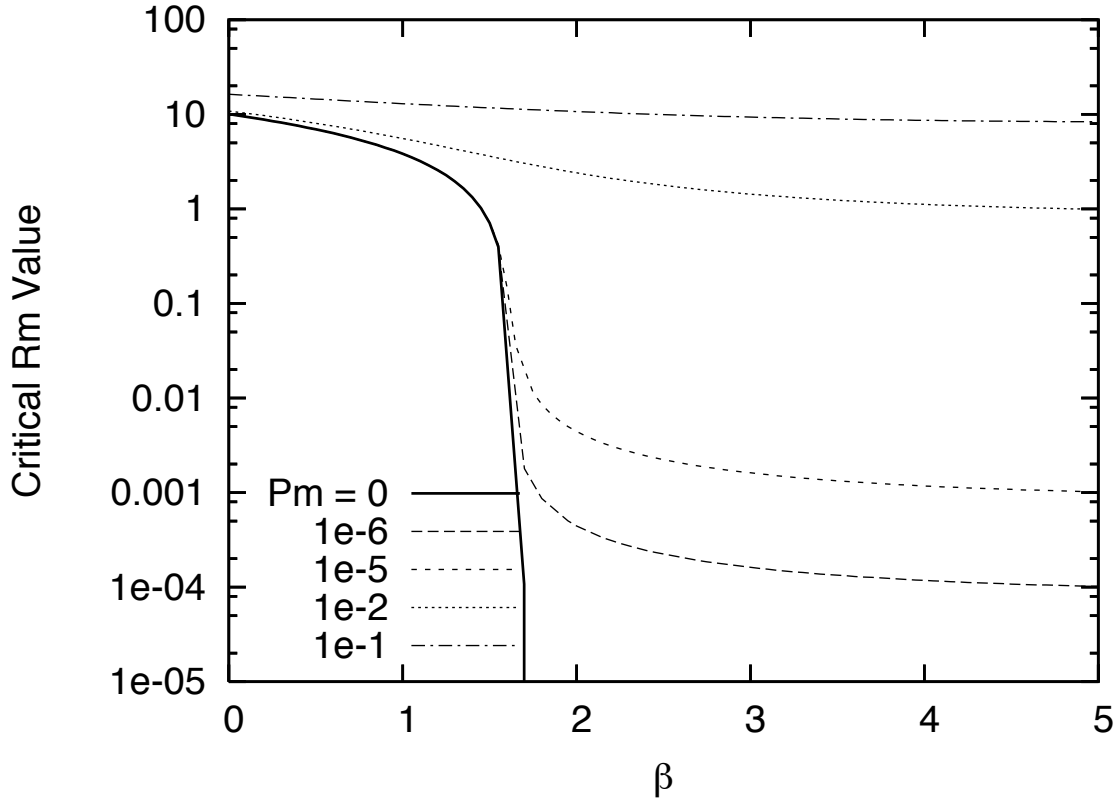

Figure 6.2: Rm_{crit} vs β for multiple Prandtl numbers. This calculation was based on the following parameters in the local dispersion relation: $r_0 = 1.5$, $L = 2.7$, $kL = 2\pi$ and $\xi = 0.115$. For $P_m = 0$, Rm_{crit} goes to zero at some critical value of β. For larger P_m, viscosity places a lower limit on Rm_{crit}.

how as ξ increases, corresponding to a steepening of the local angular momentum profile, Re_{crit} goes up orders of magnitude. Evidently the flow profile places the restriction on the magnetic profiles (β value) for low R_m MRI to emerge. The curves in 6.3 are in good qualitative agreement with Hollerbach, *et al* [12], Figure 1. (In this paper, Rm_{crit} is plotted vs. $\mu = \frac{\Omega_2}{\Omega_1}$, which is a global quantity, but varies directly with our local value of ξ).

We will make one final observation about the local linear prediction of some possible practical import to an experimental realization of MRI. For axisymmetric MRI excited in the presence of an axial background magnetic field alone, the longest wavelength disturbances are the easiest to destabilize. However, because of the addition of a radial length scale in the presence of a toroidal background field component (owing to its radial variation), one may ask if these long wavelength

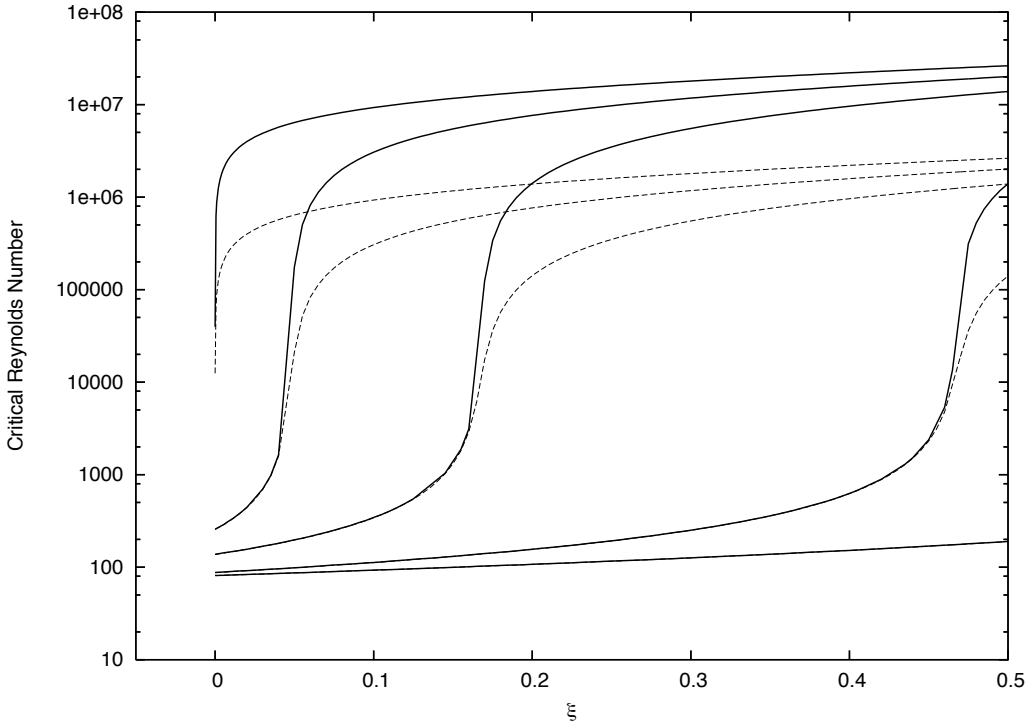

Figure 6.3: Critical hydrodynamic Reynolds number vs. ξ for several different values of β and P_m. The dashed curves are for $P_m = 10^{-5}$ and the solid curves are for $P_m = 10^{-6}$. From top to bottom, the different curves refer to $\beta = 0, 1, 2, 4, 8$.

modes continue to be the most unstable. To answer this, we used the local linear dispersion relation to calculate growth rates of modes over a wide range of k_z, and plotted the results in Figure 6.4. The first thing to notice about this plot is that indeed, for long wavelength perturbations in the $\beta = 0$ case, the growth rate is at a maximum. However, for $\beta = 8$, extremely long wavelength perturbations are not the most unstable. Rather, they are peaked at some value of k_z. Also, for $\beta = 8$, shorter wavelength (high k_z) perturbations are more unstable than when $\beta = 0$. This is a potentially important point, because if one can destabilize short wavelength modes, such that the vertical height of the system is large compared with the vertical size of the perturbation, perhaps the destructive effects of the endcaps could be reduced.

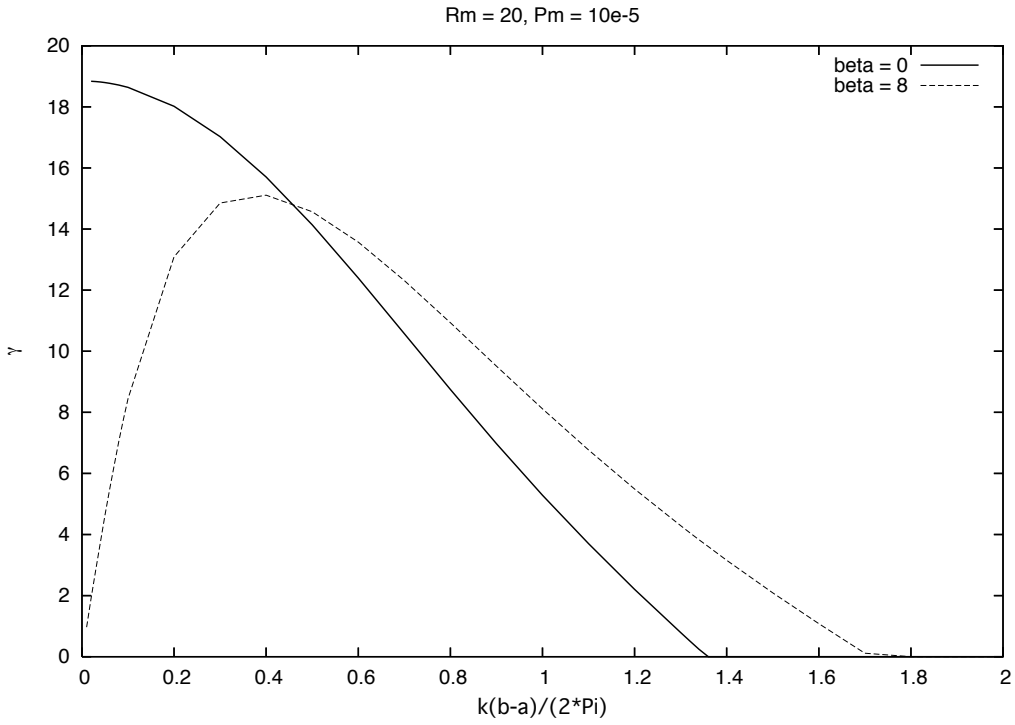

Figure 6.4: Local linear dispersion relation prediction of the maximum growth rate for a range of k_z at a fixed $R_m = 20$. Note that these growth rates did not, however, all come from the same point along the S line - rather, the location of maximum growth rate for increasing values of k_z moved to higher values of S. The abscissa is the ratio of gap width $(b-a)$ to vertical perturbation wavelength, $\frac{2\pi}{k}$.

6.2 Global MRI with a Toroidal background field

While the local linear results presented in the previous section can be qualitatively illuminating, one should not place complete confidence in their characteristics. As we have already seen, boundary layers, non-constant $\xi(r)$, and other features of nonlocality in r can affect the linear behavior of MRI modes. To try and bridge the gap between the results presented in section 6.1 and more realistic MRI behavior, we once again implemented the global algorithms described in Chapter 3.

Figure 6.5 shows boundary data from several scans along the S line, for multiple R_m values and $\beta = 0, 4$. In these calculations, $P_m = 10^{-5}$, $L = 2.7$, $a = 1$ and $b = 2$. The data markers

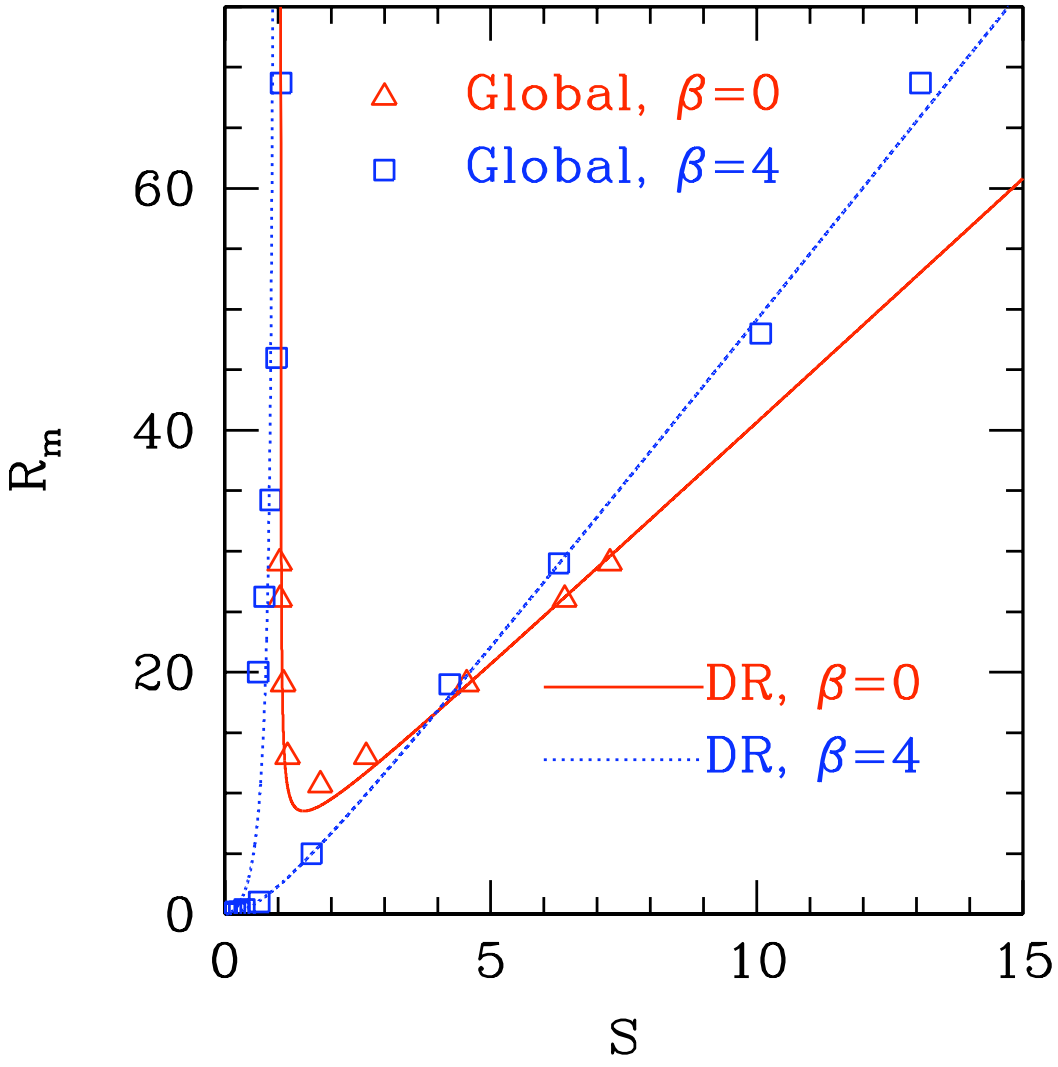

Figure 6.5: Location on the (S, R_m) plane of marginal modes for $\beta = 0$ and $\beta = 4$ as predicted by the global spectral algorithm (markers) and fits to the local linear analysis (solid and dashed curves). For this set of runs, $P_m = 10^{-5}$, $L = 2.7$, $a = 1$ and $b = 2$. For the fit to the $\beta = 0$ curve, parameters $r_0 = 1.9$ and $\xi = 0.34$. For the $\beta = 4$ curve, $r_0 = 1.65$ and $\xi = 0.3$.

represent those points at which $\gamma = 0$ was interpolated. Alongside these data are stability boundary fits using the local linear dispersion relation. As was predicted by the local linear dispersion relation, in the $\beta = 4$ case, we indeed observed the presence of growing modes at far lower values of R_m than for $\beta = 0$.

Plotted in Figure 6.6 are the real frequencies of vertical eigenmode propagation as a function

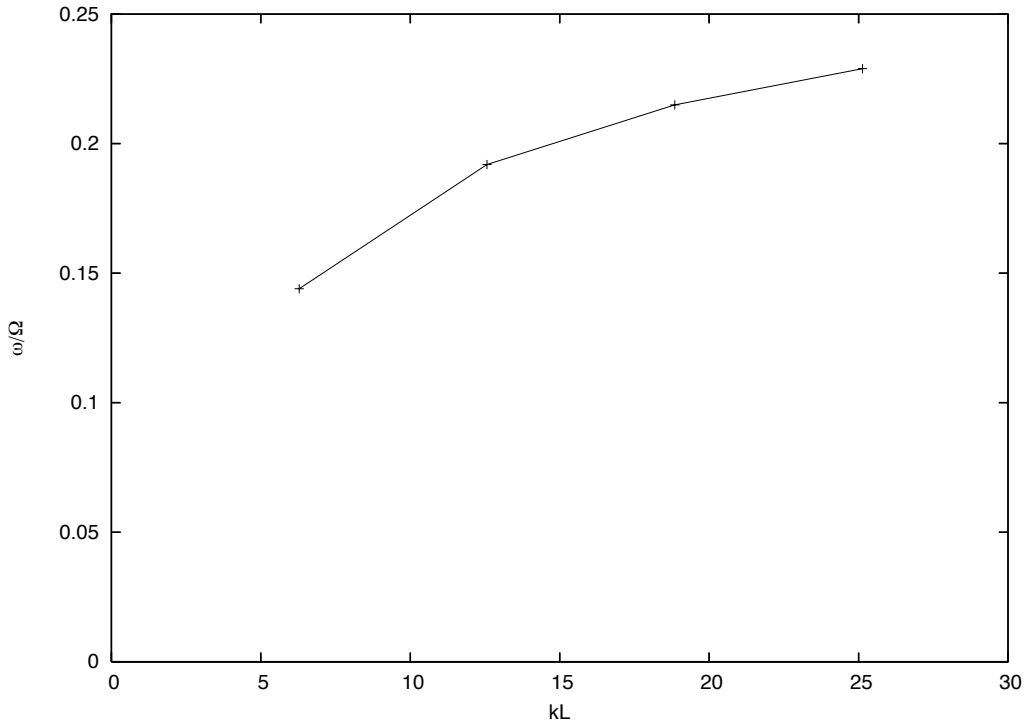

Figure 6.6: Real frequencies of vertical eigenmode propagation as a function of mode wavenumber. These calculations were for $\beta = 4$, $S = 0.5$, $R_m = 4.8$, $\mu = 0.27$ and $P_m = 10^{-5}$. Notice how both the phase velocity, $\frac{\omega}{k}$, and group velocity $\frac{d\omega}{dk}$ decrease with increasing wavenumber.

of mode wavenumber. It is interesting to note that both the phase velocity, $\frac{\omega}{k}$, and group velocity, $\frac{d\omega}{dk}$, decrease with increasing wavenumber. This is a potentially important point, since if one wishes to excite higher wavelength perturbations in an experimental setting, the vertical propagation of the mode could potentially cause complications with endcap effects. Therefore, since the vertical velocity of the perturbed wave decreases as its wavelength decreases, there is even more motivation to try and excite higher wavelength modes. They would be both small compared with the apparatus height and less likely to interact with the ends due to their slower propagation.

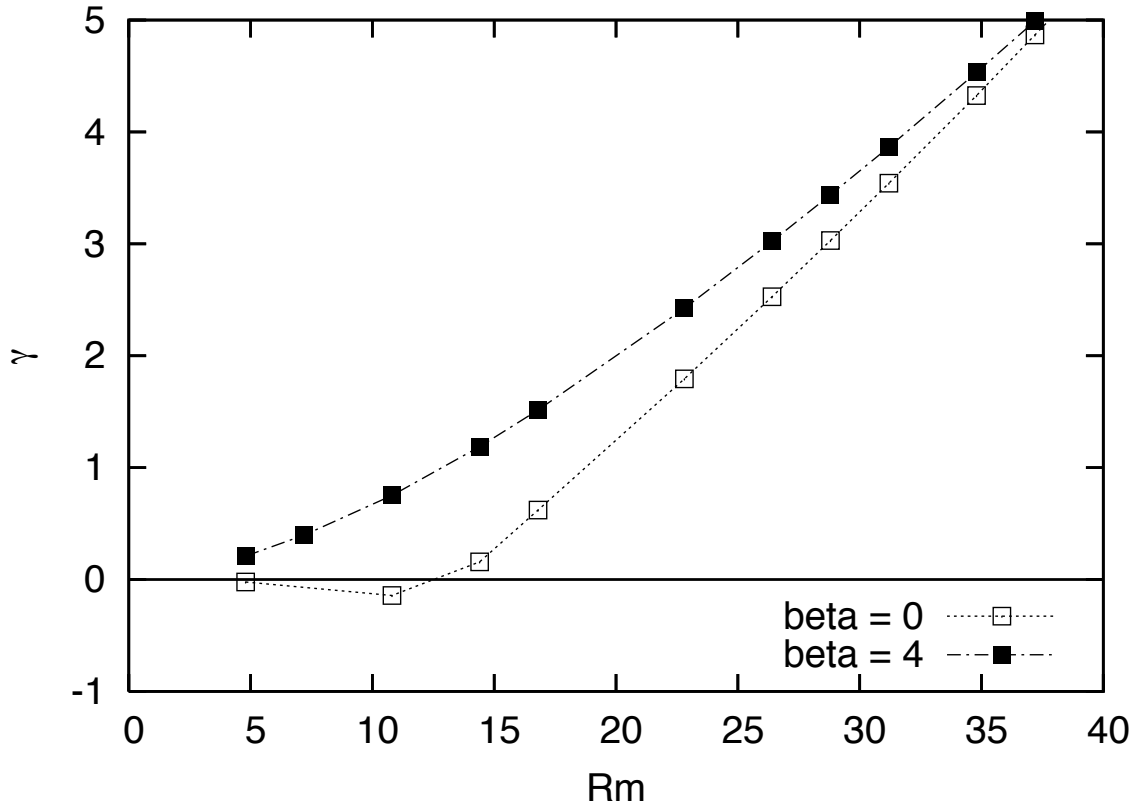

Figure 6.7: Growth rates along line $R_m = 12(S - 0.1)$ for the same parameters as Figure 6.5. For lower R_m values, when $\beta = 4$, MRI is emergent, unlike $\beta = 0$. For higher R_m values, the $\beta = 4$ growth rates are less than $\beta = 0$.

Chapter 7

3-Dimensional MRI

7.1 Linear Characteristics

A topic that has been investigated in a number of different contexts is the presence of nonaxisymmetric linear modes which are unstable to MRI. Shalybkov, *et al* presented a global analysis in which they investigated the presence of nonaxisymmetric ($m = 0, 1, 2$) in cylindrical geometry. They found characteristic magnetic field strengths beyond which the MRI forms a set of nonaxisymmetric spirals, despite the fact that the tendency of differential rotation is to favor axisymmetric modes. They also found the drift frequencies associated with these nonaxisymmetric modes [26]. Kitchatinov and Rüdiger studied both axisymmetric and nonaxisymmetric MRI in spherical geometry, and they found the parameter regimes in which nonaxisymmetric perturbations are preferred [27]. The study of these modes is relevant to the emergence of dynamos, as Cowling's anti-dynamo theorem states that dynamos can not emerge in systems with no toroidal variation [28], [29].

We examined the linear evolution of an $m = 1$ MRI disturbance using the 3 dimensional finite difference initial value code (see Chapter 3) to find out how the perturbations precess in the presence of the differential rotation. Figure 7.1 shows a time trace of the first two azimuthal mode amplitudes, and for a clear duration, the $m = 1$ has the highest amplitude (despite the fact that the $m = 0$ mode was the fastest growing). A single sinusoidal $m = 1$ perturbation was initialized at all radii. The system was allowed to evolve, and we examined the evolution of the perturbation at various radial values to figure out how much the perturbation was becoming "smeared" by the differential flow.

Figure 7.2 shows a cross section of B_r along the θ direction at various radii at $t \approx 110$. They are no longer synchronized in the θ direction, but have settled into a new orientation. It is interest-

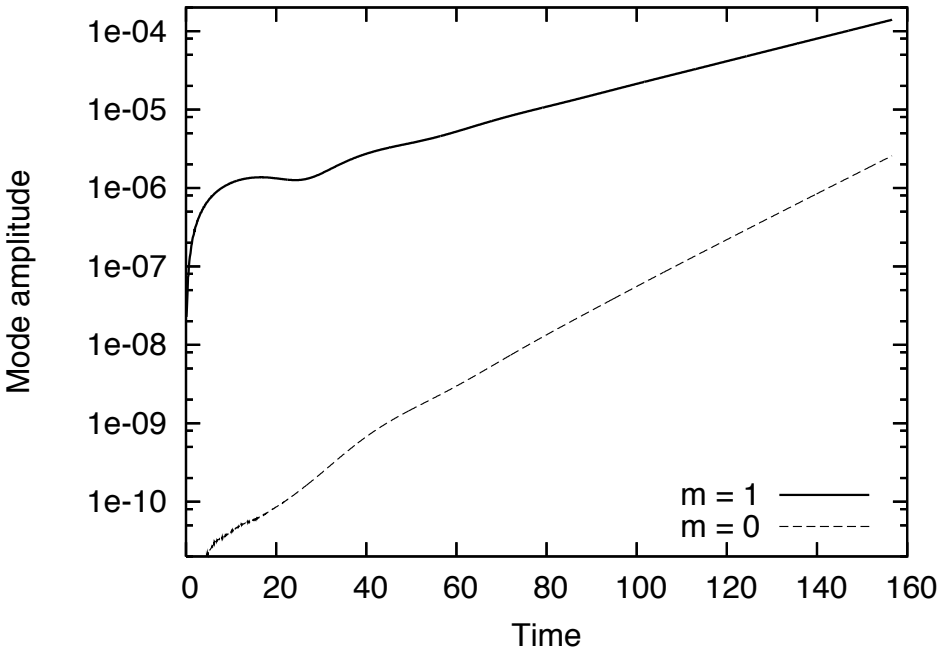

Figure 7.1: Time trace of the first two azimuthal mode amplitudes. Due to the initialization, between $t = 0$ and $t = 300$, the $m = 1$ disturbance has the largest amplitude, despite not being the fastest growing. For this run, $P_m = 0.1, R_m = 360, S = 51, a = 0.5, b = 1.5, L = 1$, and $\mu = 0.175$.

ing to note that after this orientation sets in, it is relatively time independent, as demonstrated in Figure 7.3, which shows the precession frequency of this nonaxisymmetric mode at different radii. After some transient period ($t < 60$), they all precess with roughly the same frequency, which is approximately 25% of the inner cylinder angular frequency (roughly the value of Ω halfway between the cylinders).

Plotted in Figure 7.4 are contours of B_r in the (r, θ) plane during the linear phase. During this linear stage, there is a phase shift of π of the $m = 1$ mode between the inner and outer radii, and this configuration is time independent. This suggests that a local linear analysis may actually prove fruitful in investigating 3D MRI, since the shear in the radial direction does not significantly affect the precession frequency of the unstable mode. While we will not explore this linear MRI behavior for $m \neq 0$ in this document, we have included the derivation of the nonaxisymmetric local linear analysis in Appendix B.

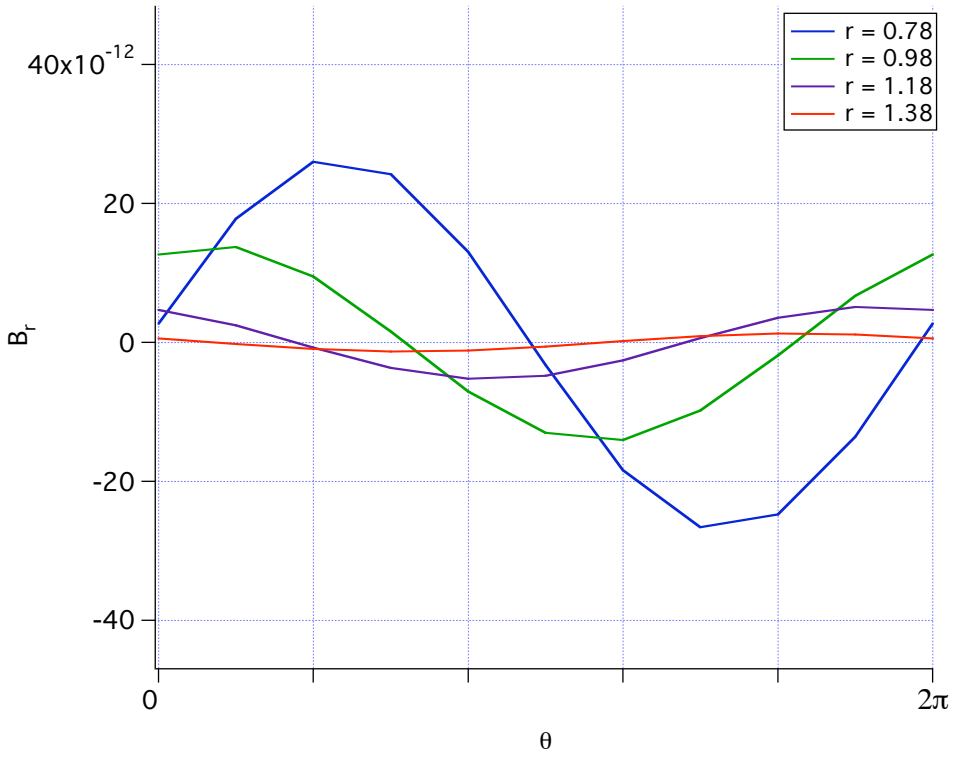

Figure 7.2: cross section of B_r along the θ direction at various radii at $t \approx 110$. They are no longer synchronized in the θ direction, but have settled into a new, time-independent orientation.

7.2 Destabilization of a saturated MRI mode

Relying on an axisymmetric analysis to capture the nonlinear characteristics of MRI can be dangerous. Many numerical simulations have demonstrated that far more interesting and rich behavior emerges in full 3D, and in some cases, 2D simulations can be misleading.

One such example is presented in this section, based on parameters suggested by Wolfgang Dobler [24] in his nonlinear 3D simulations. We used the fully 3D finite difference algorithm using the following initial conditions: $a = 0.5, b = 1, \Omega_1 = 2, \mu = 0.35, B_0 = 0.2, L = 1, P_m = 1$, and $\nu = 7 \times 10^{-4}$. At each timestep, we decomposed B_r into it's azimuthal and axial components along the lines $(r = 0.6, z = 0.8)$ and $(r = 0.6, \theta = 0)$, respectively. The results are plotted in Figures 7.5 and 7.6. Note how after the primary axisymmetric $(m = 0)$ mode saturates around $t = 25$, nonaxisymmetric modes begin to grow exponentially. These modes are no longer growing atop the laminar base state described earlier ($\mathbf{B} = B_0 \mathbf{e}_z$, $\mathbf{v} = r\Omega(r)\mathbf{e}_\theta$), but rather a new base

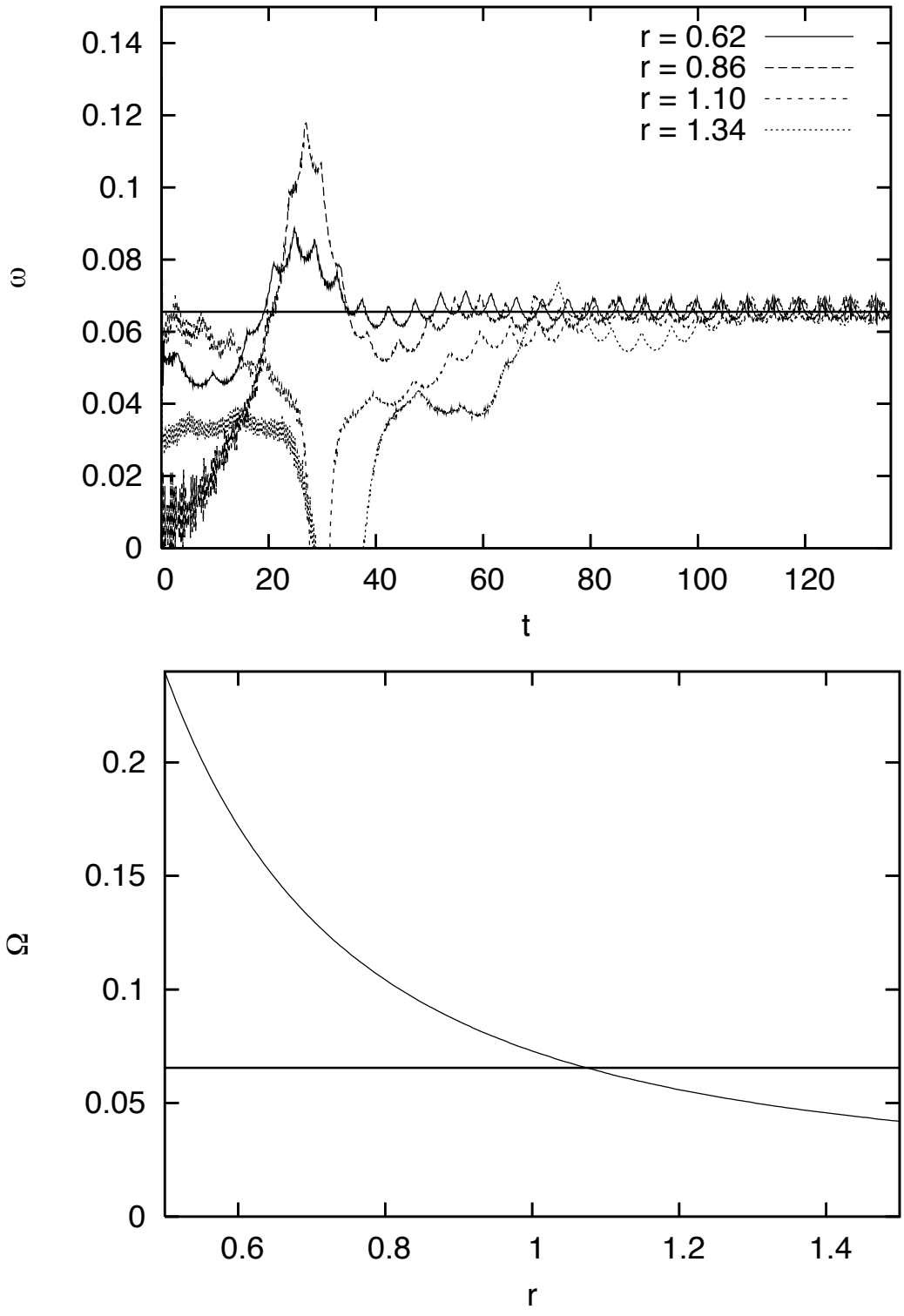

Figure 7.3: Top: Precession frequency of the $m = 1$ mode at different radii. After an initial transient phase, the precession of the mode becomes approximately $\omega = 0.065$ at all radii. This value is marked by the solid horizontal line. Bottom: $\Omega(r)$, the Couette profile. The precession frequency is again shown by the solid horizontal line.

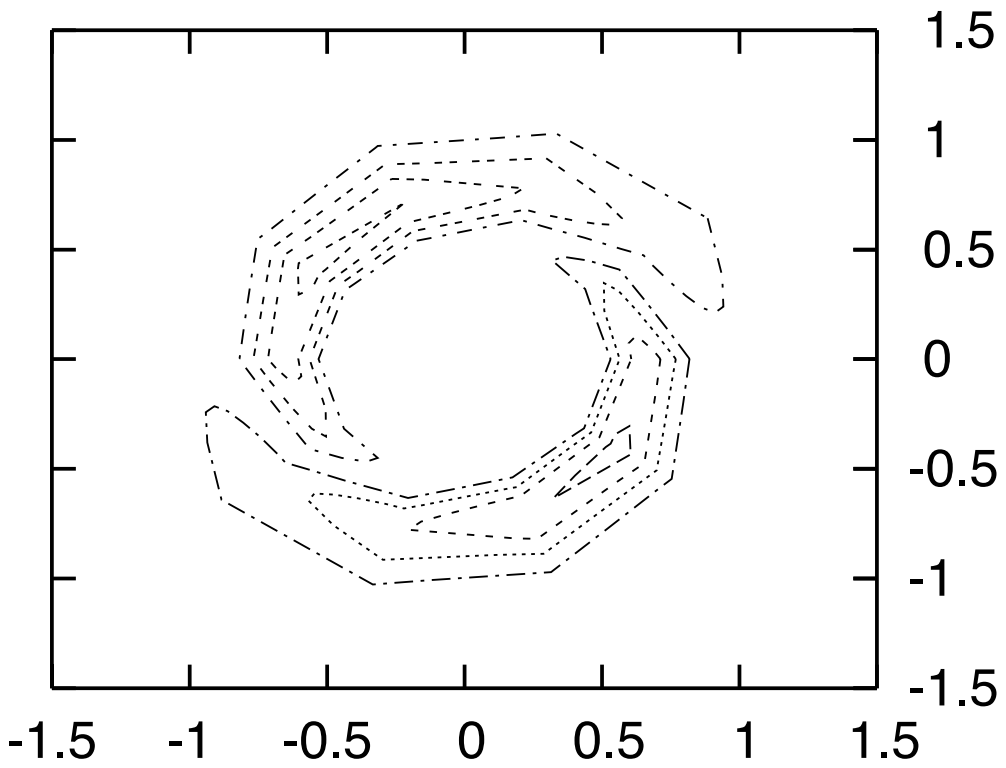

Figure 7.4: Contours of B_r in the $r-\theta$ plane during the linear phase of an $m=1$ dominated MRI mode. There is precisely a phase difference of π of this mode from the inner radius to the outer radius, and this phase difference is time independent during the linear phase.

state corresponding to the saturated axisymmetric MRI mode. Therefore, to characterize these new nonaxisymmetric modes, we need to first understand this saturated MRI state.

Cuts and cross sections of the saturated MRI magnetic and velocity fields are plotted in Figures 7.7 - 7.15. The first thing to notice in Figure 7.7 (a) is how the originally purely axially oriented magnetic field becomes warped in the nonlinear stage. Especially interesting is below $z \approx 0.75$, the field is oriented in the outwardly radial direction, while above this line, the field is oriented inward. This is a reverse field configuration (RFC), a configuration known to be particularly unstable to tearing modes [30], [31]. A similar RFC can be seen in the (r,z) cross section of B_θ (Figure 7.7, b), where from below to above the $z \approx 0.75$ line, the field orientation goes from negative to positive in the $\hat{\theta}$ direction. Thus the complete picture of the RFC is one in which the individual field lines are kinked back upon themselves and tilted at a forward $\hat{\theta}$ pitch

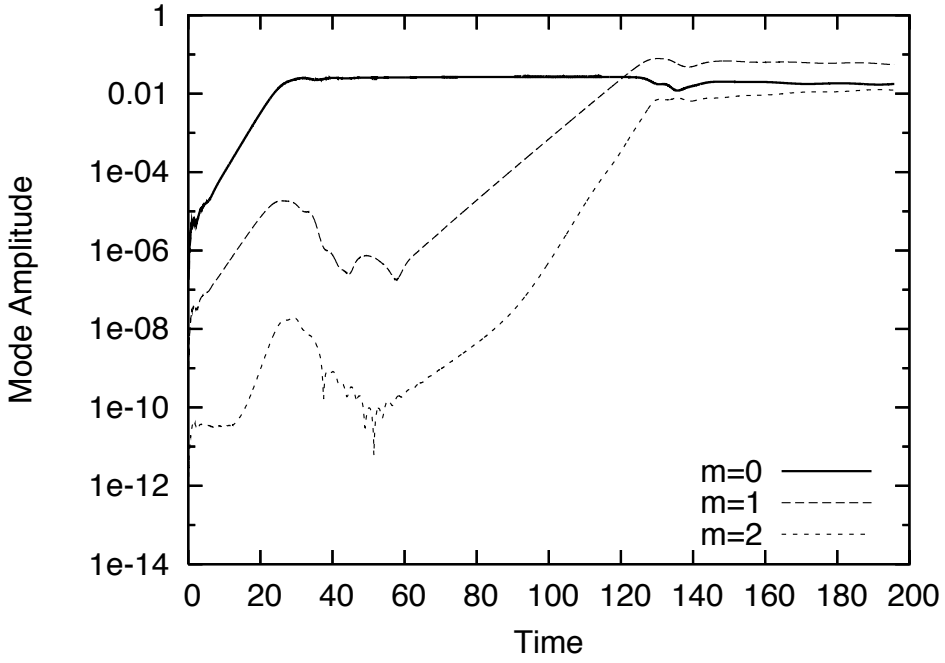

Figure 7.5: The 1st three azimuthal mode amplitudes measured at $(r = 0.6, z = 0.8)$.

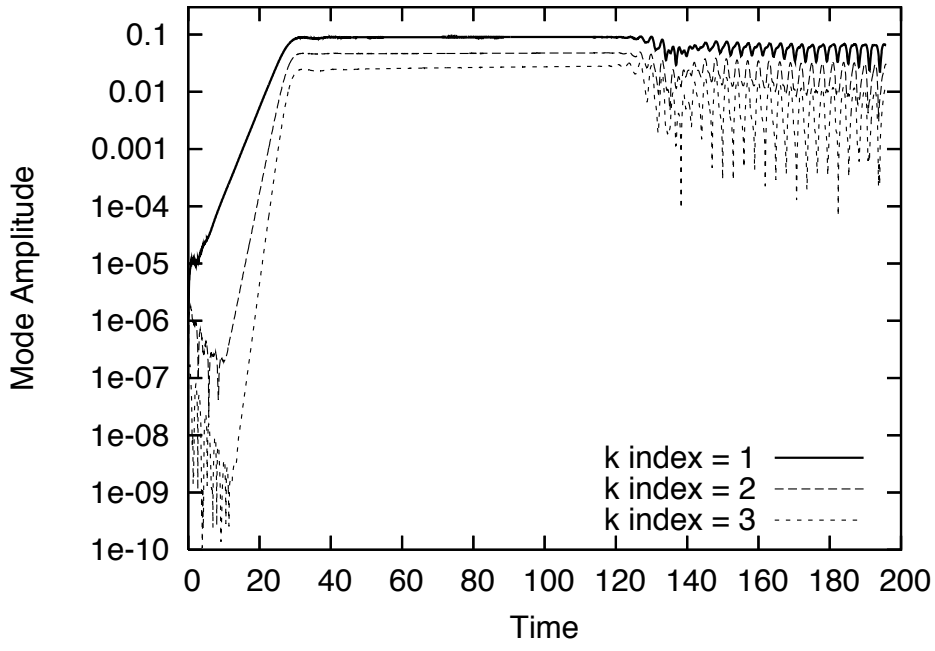

Figure 7.6: The 1st three axial mode amplitudes measured at $(r = 0.6, \theta = 0)$.

from $+\hat{r}$.

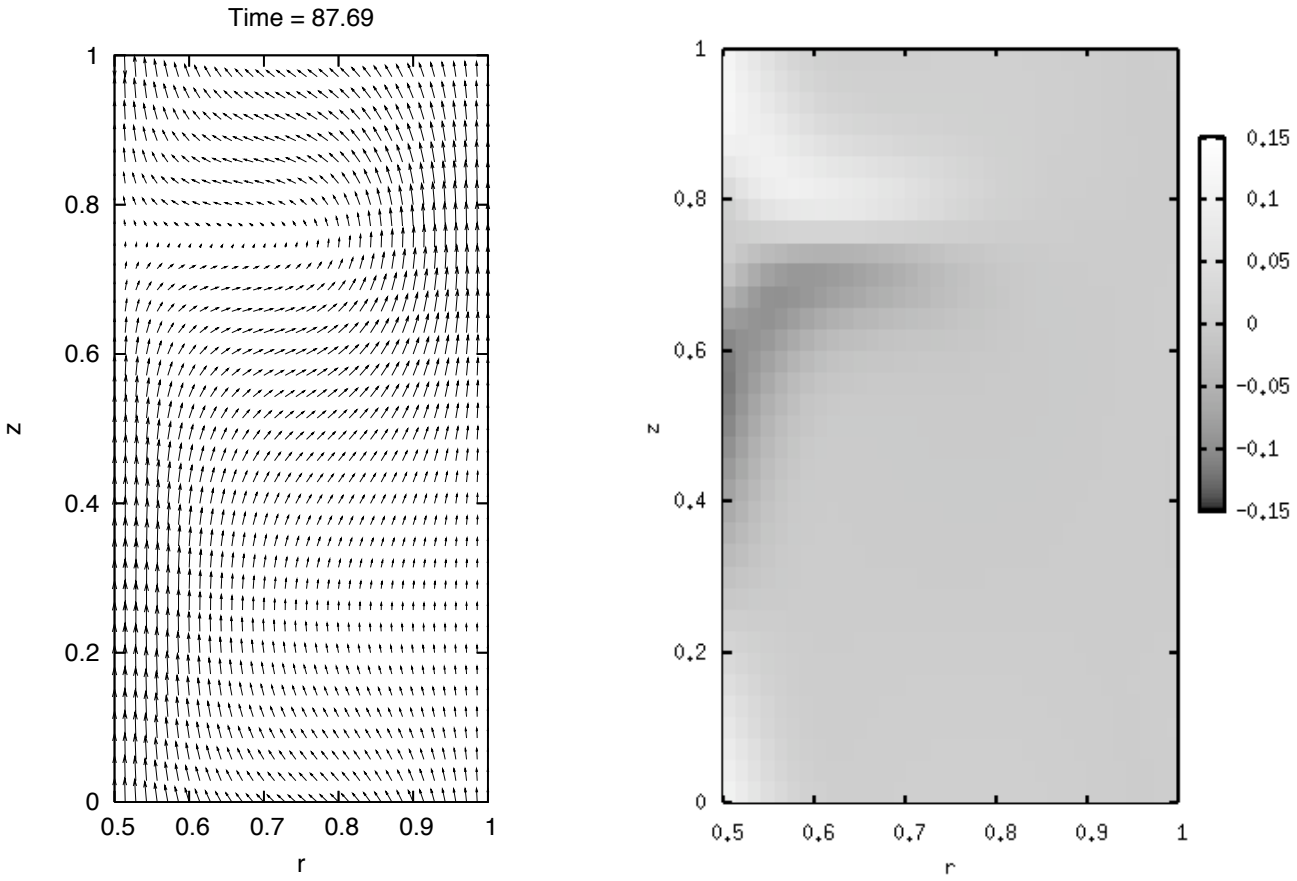

(a) (b)

Figure 7.7: (a) rz cut of the total B field. (b) rz cut of the B_θ field.

The saturated velocity field is mainly characterized by a strong radial outflow concentrated around the RFC line, $z \approx 0.75$, shown in Figure 7.8 (a). This jet is most likely the mechanism that bends the originally straight axial magnetic field lines outward. Plotted in Figure 7.8 (b) is the cross section of V_θ in the (r, z) plane, minus the average azimuthal profile, $< V_\theta(r) >$. It is clear that the azimuthal flow profile has been altered in the saturated state. Figure 7.10 makes this more apparent, as radial cuts along three lines, $(\theta = 0, z = 0.2, 0.5, 0.8)$, all demonstrate very different behavior than the original Taylor-Couette profile. In all cases, the $\Omega(r)$ profile has been flattened in the bulk, which is characteristic of MRI, as the instability ultimately tries to synchronize Ω (see

chapter 5). However, $\Omega(r)$ along the line $z = 0.8$ (near the RFC line), the average V_θ increased by almost 50% compared with the original Couette flow. Thus, the fluid jet concentrated along the RFC line is also tilted at a forward $\hat{\theta}$ angle from $+\hat{r}$.

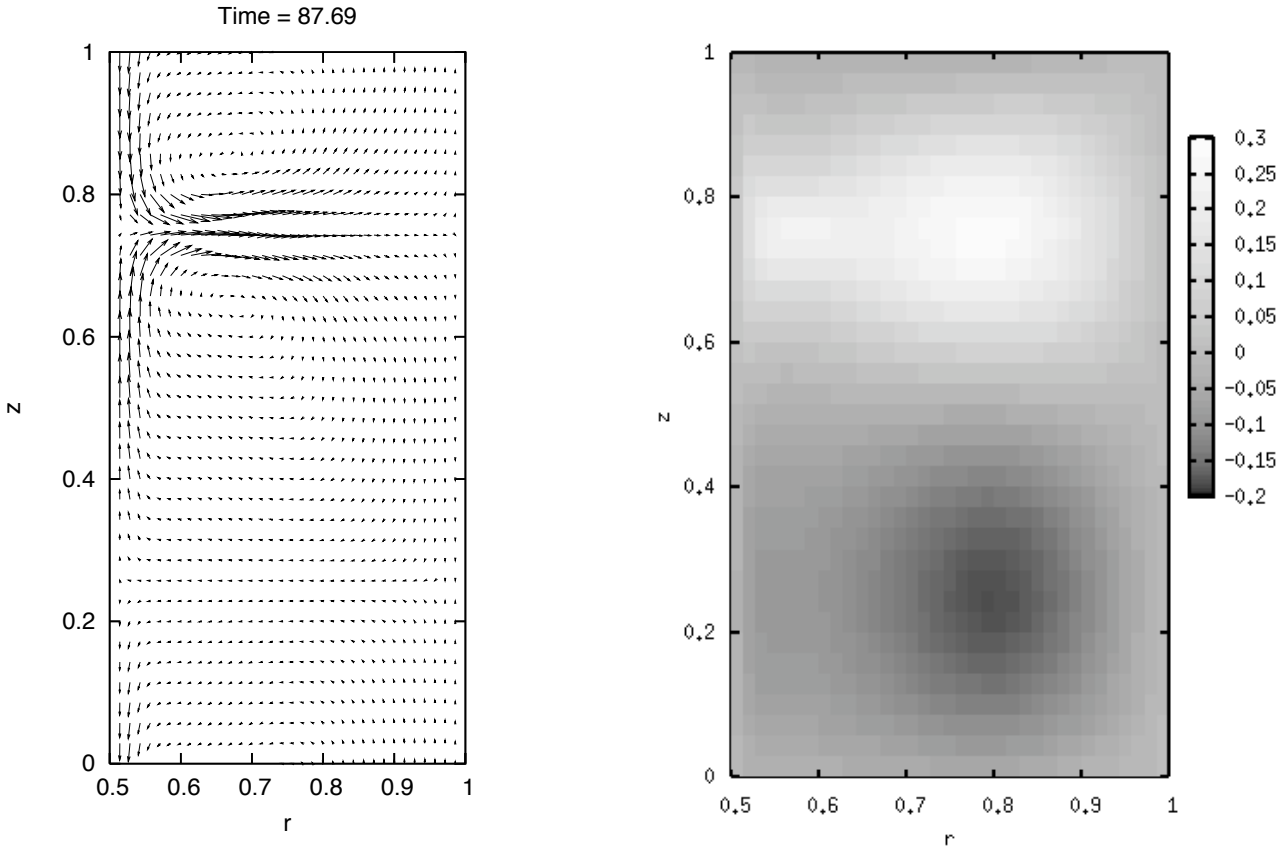

(a) (b)

Figure 7.8: (a) rz cut of the V field. (b) rz cut of the perturbed V_θ field.

We will now compare and contrast the linearly unstable $m = 1$ mode with the post-MRI saturated nonlinearly unstable $m = 1$ mode. Figures 7.11 and 7.12 are cross sections of the Velocity field in the $(R\theta, z)$ plane, where $R = 0.6$ is a constant value and θ ranges from 0 to 2π. To single out only the nonaxisymmetric components, we subtracted out the constant portion of the field along each z grid value. During the linear MRI phase, the dominant nonaxisymmetric component consists of four counterrotating vortices, similar to the Taylor vortices emergent in

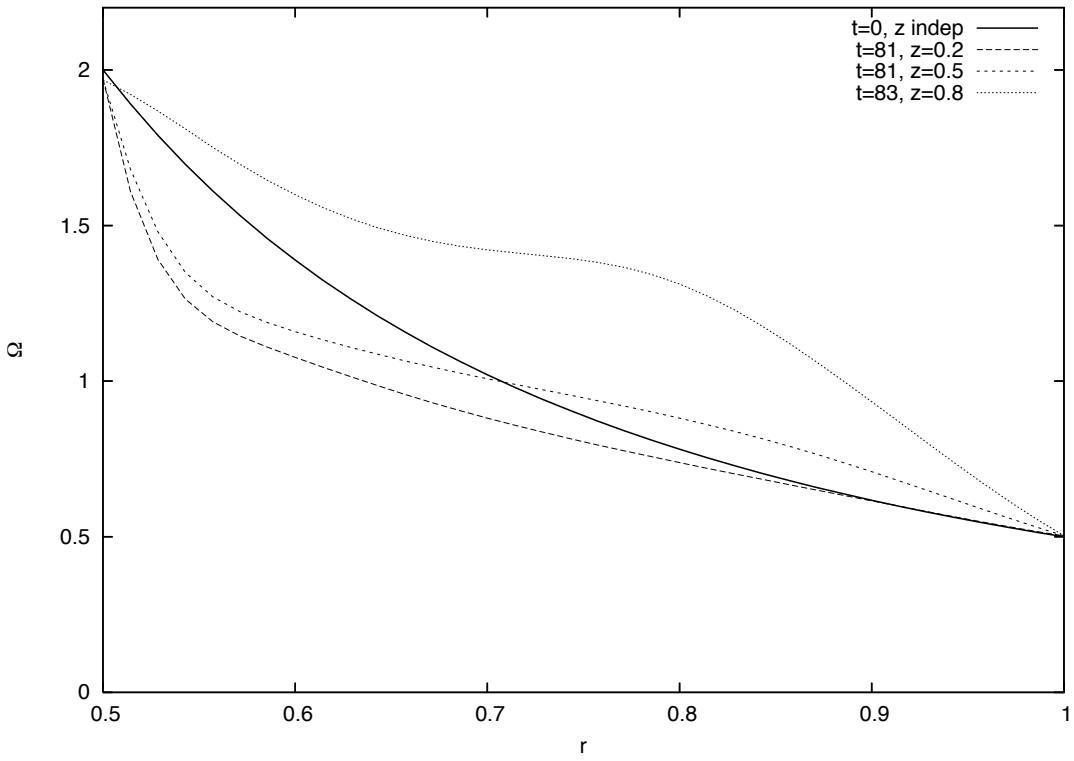

Figure 7.9: Saturated $\Omega(r)$ profiles at three different cuts along the z direction.

the (r, z) plane in axisymmetric MRI. The linearly unstable nonaxisymmetric mode is thus the same as the dominant axisymmetric mode, rotated by $\frac{\pi}{2}$. The $m = 1$ mode that grows after the axisymmetric MRI saturates is different, as can be seen in Figure 7.12. First of all, there are only two counterrotating vortices, and they are highly localized about the RFC line. This is an important point to note, that directly above the RFC line, the perturbed velocity field is moving in the opposite direction compared to below the RFC line.

Now that we have a feel for the general structure of the saturated MRI state and the nonaxisymmetric mode it destabilizes, let us hypothesize the physical process that may then take place. Visualizing a single magnetic field line, as in Figure 7.13, the original axially oriented field is kinked outward radially and forward azimuthally. At the base of the kink, the RFC is formed, where above, the field points inward and below, it points outward. The background nonaxisymmetric velocity perturbation (Figure 7.12) is one in which above the RFC, the field is

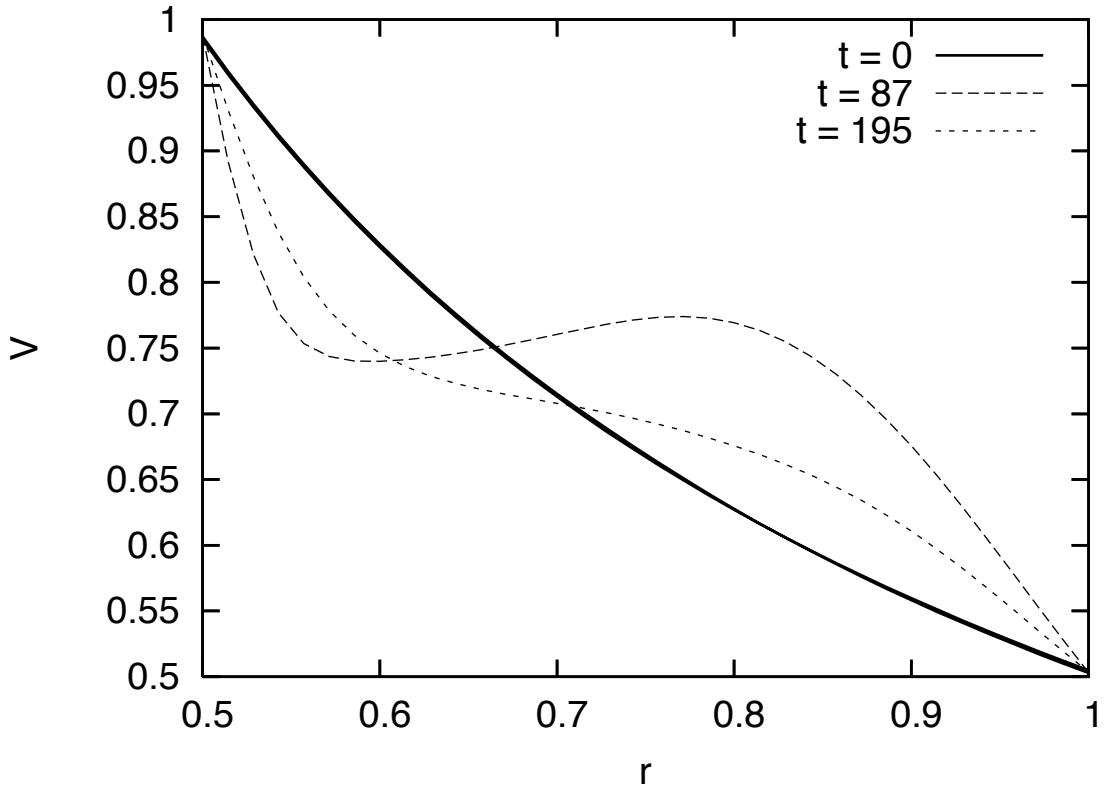

Figure 7.10: Average saturated $V(r)$ profiles at three different times (linear phase, axisymmetric saturated phase, nonaxisymmetric saturated phase).

faster (or slower, depending on θ) than average in the $\hat{\theta}$ direction, and below, it is slower (faster). As the perturbation grows, this structure becomes exponentially more influential, and one can imagine this profile dragging the kinked field along with it. This would cause a twisting of the magnetic field kink into a plane perpendicular to the axial direction. If in addition to this twisting the magnetic field were to reconnect at the RFC location due to the tightening length scale, then the kink would snap off into a magnetic island in this plane. This would leave behind a 2 component magnetic field, with a magnetic island in the (r, θ) plane and a purely axial field. Since the velocity field perturbation in Figure 7.12 is an $m = 1$ structure, one may expect that 2 of these magnetic islands would form in this plane. Note, however, that in Figure 7.5, the $m = 2$ structure also grows exponentially and mixes in with the saturated structure, so whether 2 or more islands form is a nonlinear question and not easily predictable.

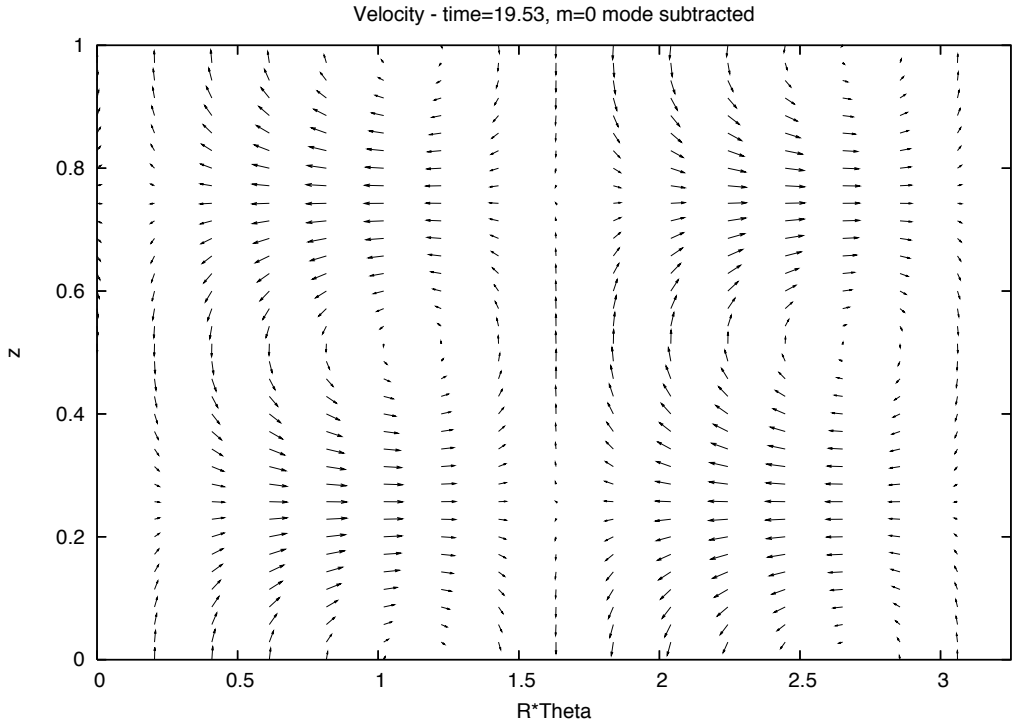

Figure 7.11: Linear nonaxisymmetric unstable MRI mode.

To verify with any certainty the above hypothesis, we must look for signatures in the second saturated state. Notice that in Figure 7.5, the $m = 1$ mode grows and dominates initially in the new nonlinear state, but the $m = 2$ mode winds up with a pronounced presence as well. In Figure 7.14, two time snapshots of contours of B_r in the (r, θ) plane along the RFC line ($z \approx 0.75$) are plotted. At $t = 114.64$, the $m = 1$ mode dominates, and these signatures of B_r suggest that there exist two of these magnetic islands. They would be oriented $\frac{\pi}{2}$ out of phase with these contours, but have the same basic structure (the null B_r contours are those locations where the island field line is purely azimuthal). The second snapshot, taken at $t = 132.23$, is dominated by an $m = 2$ mode, and consequently, we infer the presence of four magnetic islands. All of the structures formed during this phase are nonlinearly interacting, so it is difficult to predict or even measure the timescales over which these islands persist.

In Figure 7.15, the total saturated velocity field is plotted in the $(R\theta, z)$ plane, where again, $R = 0.6$ is a constant value and θ ranges from 0 to 2π. One can see the "wavy" structure of the

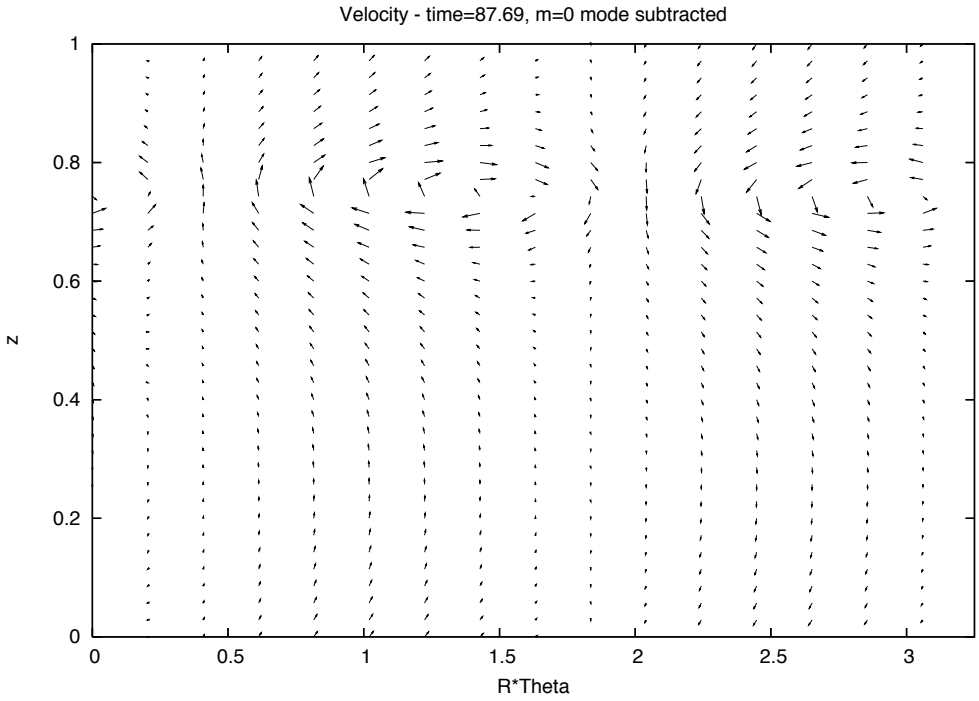

Figure 7.12: Nonlinear nonaxisymmetric unstable mode.

new velocity field. This behavior is consistent with [24].

Finally, given that we have predicted that reconnection has occured in this process, we should look closely at the saturated profile for reconnection signatures. One such signature can be estimated by measuring the fluid's departure from ideal MHD. In ideal MHD, the "frozen in" condition on the magnetic field lines is represented thus:

$$\mathbf{E} + \mathbf{v} \times \mathbf{B} = 0 \tag{7.1}$$

For finite diffusivity, however, the right hand sign deviates from zero (becomes $\eta\mathbf{J}$) when field lines violate the "frozen in" condition. This happens during events such as tearing and magnetic reconnection, since the field lines "break". Dotting $\mathbf{B}$ into equation 7.1 eliminates the second term, and what is left is simply $\mathbf{E}\cdot\mathbf{B}$ on the left hand side. We can therefore interpret $\mathbf{E}\cdot\mathbf{B}$ as a measure of how much the "frozen in" condition is being violated. For the run depicted in Figure 7.5, we

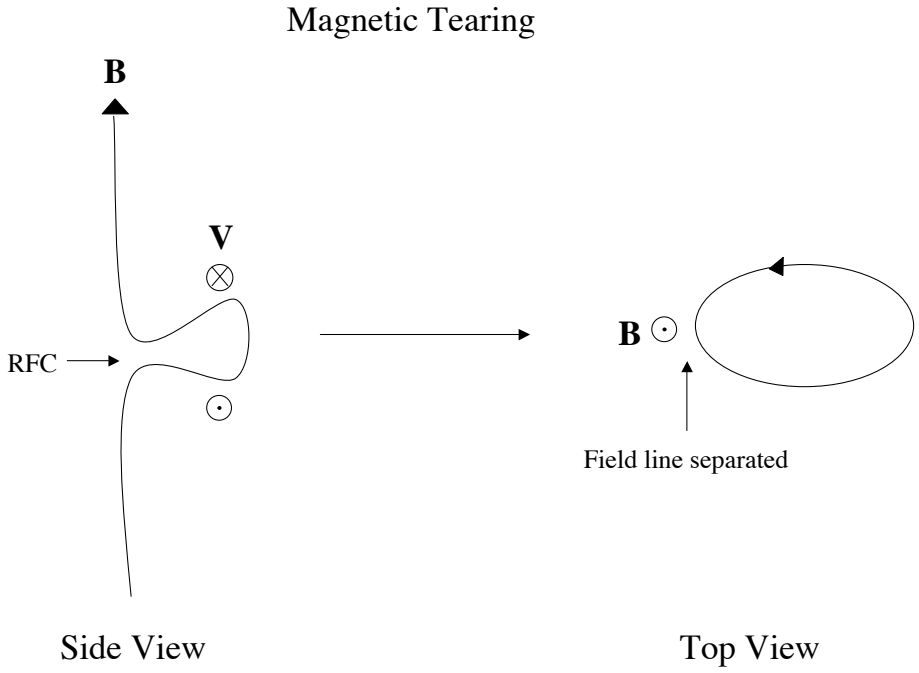

Figure 7.13: Cartoon of a kinked magnetic field being twisted by a velocity field. The reverse field configuration (RFC) set up by the kink in the field line eventually reconnects, and the resulting magnetic field configuration is a vertical (axial) component and an orthogonal magnetic island.

measured the maximum value of $|\mathbf{E} \cdot \mathbf{B}|$ on the (r, z) mesh ($\theta = 0$) at each timestep. We found that around the time that the $m = 1$ mode overtakes the system, which is the time that we believe the kinked magnetic field is being torn, $|\mathbf{E} \cdot \mathbf{B}|$ jumps by approximately 3 orders of magnitude (see Figure 7.16). Plotted in Figure 7.17 is a contour plot of $\mathbf{E} \cdot \mathbf{B}$ in the $(r, \theta = 0, z)$ plane, and it is clear in this plot that the largest departure from ideal MHD occurs along the $z \approx 0.75$ line, where the original RFC was located.

7.3 MRI with endcaps

Our analysis so far has mainly dealt with a system with periodic boundary conditions at $z = 0$ and L. It has proven useful in discovering many features of MRI, both linear and nonlinear. However,

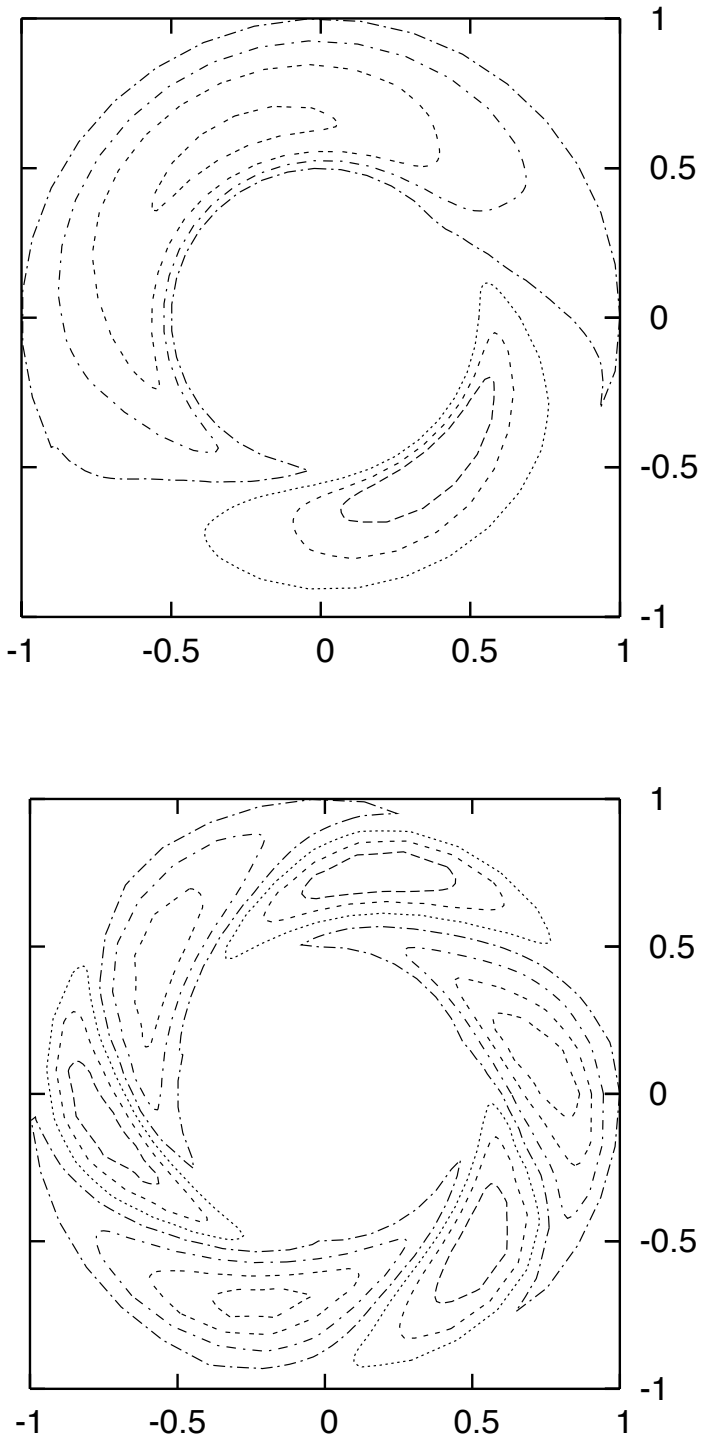

Figure 7.14: Contours of B_r in the (r, θ) plane at $z = 0.8$. Top: Time = 114.64. The $m = 1$ mode is dominant. Bottom: Time = 132.23. The $m = 2$ mode overtakes. This behavior is consistent with the diagnostic in Figure 7.5.

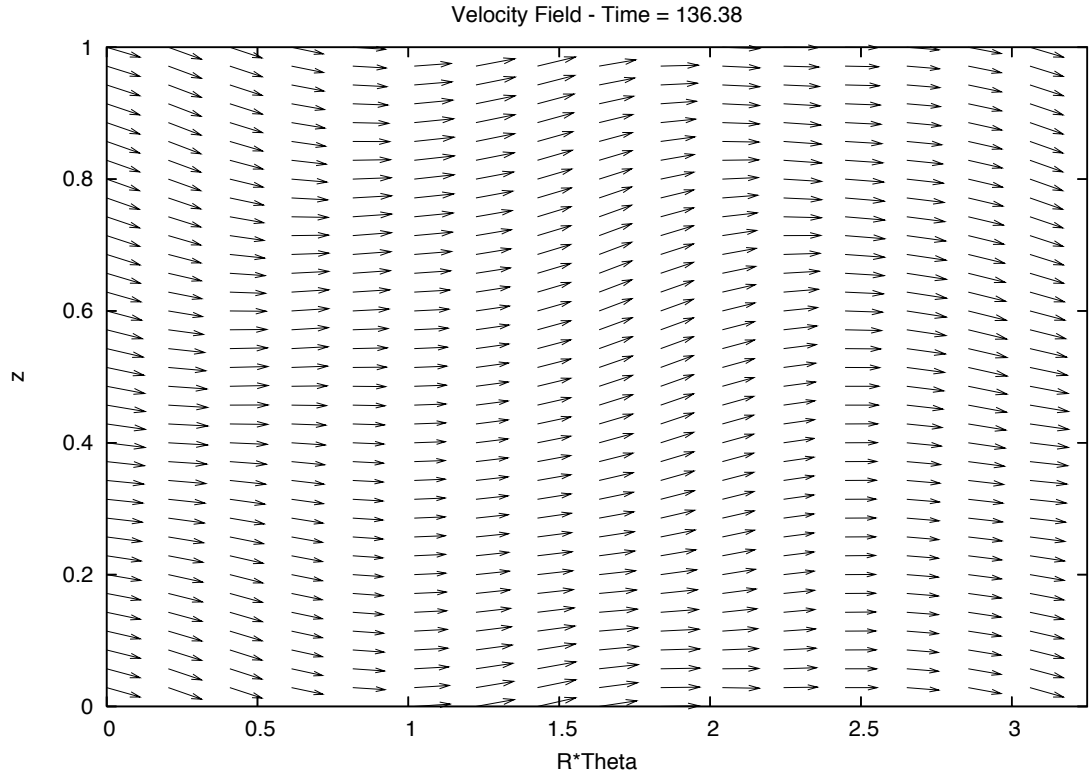

Figure 7.15: θz cut of the V_θ field.

it is simply not possible to build an infinitely long experiment - one must, of course, cap off the top and bottom of the vessel. As stated in chapter 1, this causes many complications with a high Reynolds number flow, including Ekman pumping, increased turbulence leading to the disruption of laminar base state, etc.

Much work has been done computationally by Liu, *et al* to determine the best endcap configuration for maintaining laminar Couette flow and minimizing the end effects [32]. Experimentally, the Princeton experimental MRI group devised a cylindrical experiment with endcaps consisting of 2 differentially rotating rings. They have conducted experiments using water as a fluid medium, and their velocimetry measurements suggest a great deal of promise for achieving the desired laminar base state at high Reynolds number [8], [33].

We attempt here to characterize MRI in the presence of differentially rotating endcaps using the 3 dimensional FD code. The boundary conditions at $z = 0, L$ are perfectly conducting for the

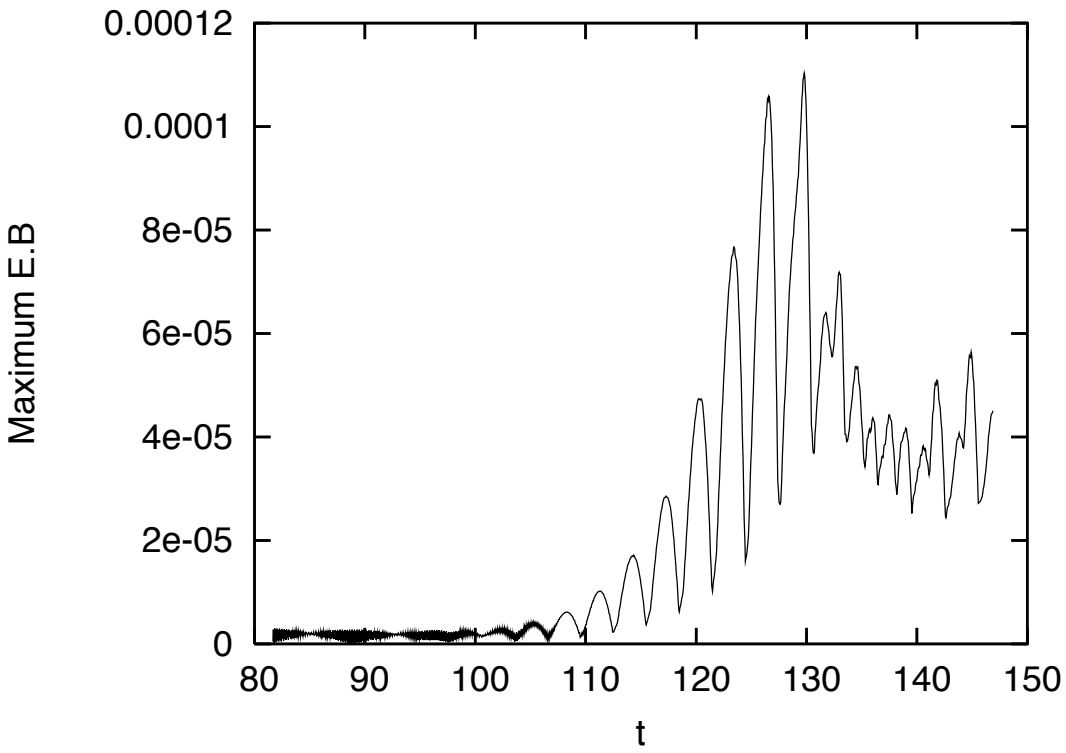

Figure 7.16: Time trace of the maximum gridded value $|\mathbf{E} \cdot \mathbf{B}|$ in the (r, z) plane around the time of tearing.

magnetic field, and no slip for the velocity field. The velocity profile of the endcap itself is the same as laminar Couette flow, equation 4.7.

7.3.1 Emergence of MRI

Plotted in Figure 7.18 are MRI growth rates as a function of S at fixed R_m, with periodic boundary conditions (no endcaps). At approximately $S = 6$, MRI is destabilized. We selected 2 values of S to run simulations with endcaps - one with $S = 2.8$, which should be stable to MRI, and one with $S = 10.8$, which should show signs of MRI. We will label the runs A and B, respectively. The following parameters were the same for both runs: $P_m = 0.07, L = 5.4, a = 1, b = 2, \mu = 0.27$ and $R_m = 1166.4$. Note that the system is much taller than it is wide ($L/(b - a) = 5.4$) - this was intentional to try and minimize the fluids interaction with the endcaps. The resolution for each

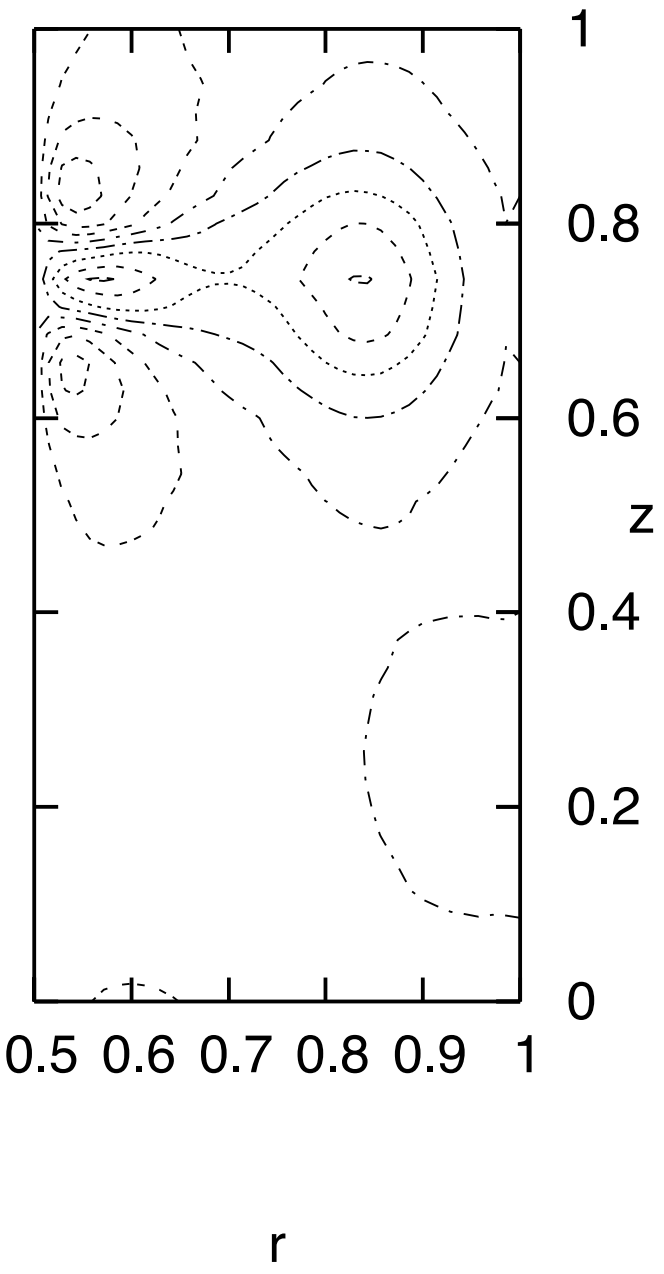

Figure 7.17: Contour plot of $\mathbf{E}\cdot\mathbf{B}$ in the (r, z) plane at the time of tearing ($t = 112.88$). Maximum values of $\mathbf{E}\cdot\mathbf{B}$ are along the RFC line.

run was $35 \times 20 \times 60$, and each run took approximately 2 hours to complete.

Figure 7.19 shows $< |\boldsymbol{\delta B}| > /B_z$ vs. time, where $< |\boldsymbol{\delta B}| >$ is the magnitude of the perturbed field strength averaged over the domain. This image is thus a measure of the amplification of the

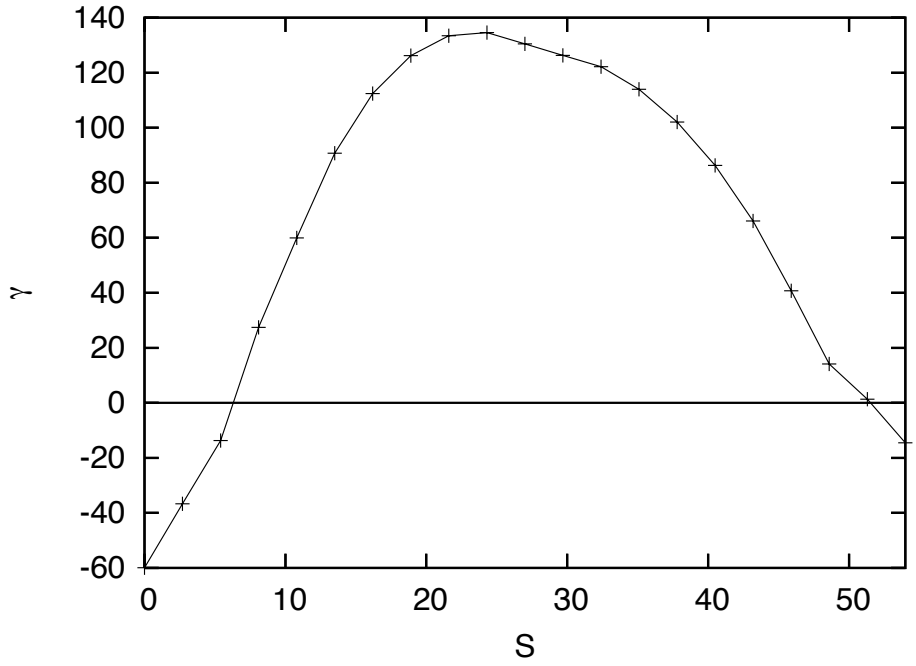

Figure 7.18: Scan using the spectral code along the $S = V_A L/\eta$ line at fixed $R_m = \Omega_1 L^2/\eta = 1166.4$. The growth rates are normalized to diffusive timescale L^2/η. Other parameters for this run are $P_m = 0.07, L = 5.4, a = 1, b = 2, \mu = 0.27$. Two runs with endcaps were executed based on the data in this figure - one at $S = 2.8$ (run A, stable to MRI) and one at $S = 10.8$ (run B, MRI unstable).

magnetic fluctuations normalized to the applied background axial field strength. In run A, there is some amplification, despite the fact that MRI ought not be present. However, in run B, there is significantly more amplification, and the amplification is comparable to the runs described in section 5.4.1. This is a good sign that MRI has emerged in the system despite the presence of endcaps.

Plotted in Figures 7.20 and 7.21 are contours of B_r and V_r at $t = 1000$, after the magnetic growth has saturated. It is clear from these comparisons that a different mechanism is at work. In Run A, both profiles indicate the presence of a sharp Ekman layer near the endcaps. In Run B, the profiles exhibit some of the same MRI characteristics seen in the previous section: reverse field configuration in B, fluid jet oriented radially outward.

For reference, figure 7.22 shows $< |\boldsymbol{\delta B}| > /B_z$ vs. time for both Run B and a run with no endcaps, with all of the other parameters held constant. Note that both the saturation amplitudes

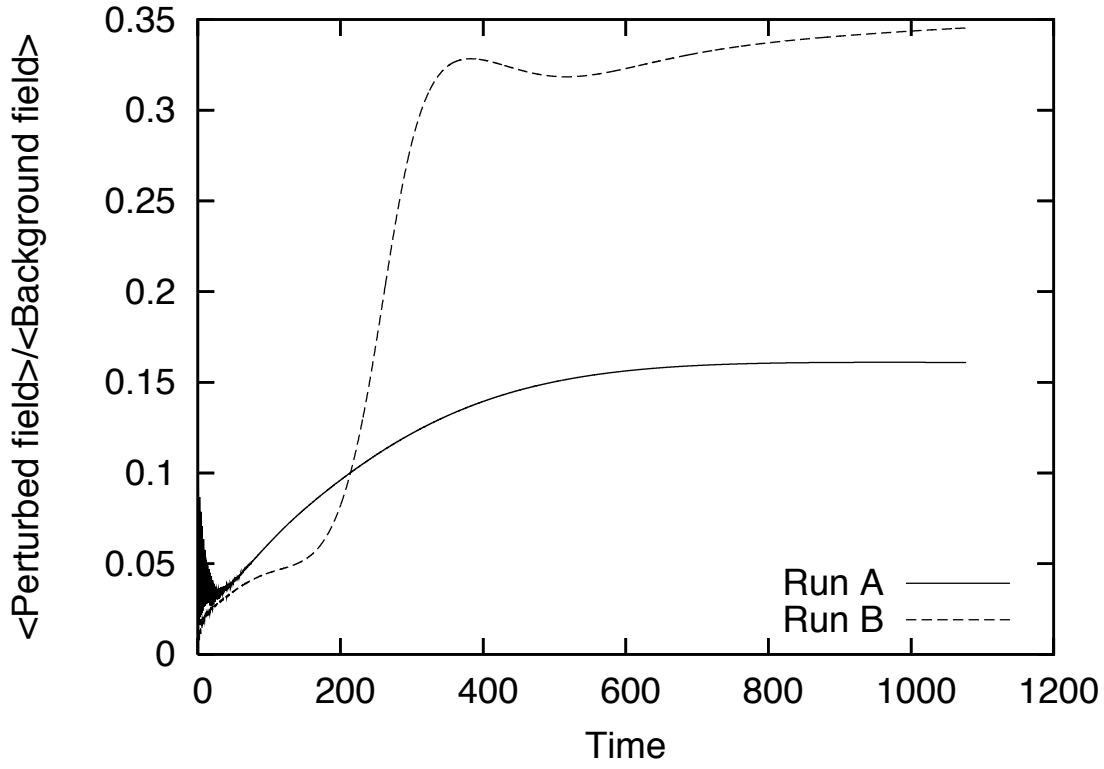

Figure 7.19: $< |\boldsymbol{\delta B}| > /B_z$ vs. time in runs A and B (A is stable to MRI, B is unstable). The perturbed magnetic field amplification in run B is approximately 34%, which is comparable to similar runs without endcaps.

and the MRI growth rates are comparable in these cases.

7.3.2 MRI with endcaps and toroidal field

Figure 7.23 shows a comparison of Run B ($\beta = 0$) and an identical run with an added toroidal field ($\beta = 8$). That the MRI persists under these conditions is promising; the vertical motion of the MRI modes could interact destructively with the Ekman circulation near the endcaps, but these results indicate that it is not enough to prevent the unstable modes from growing to saturation. Since the critical Reynolds number for observing MRI at $\beta = 8$ is so much lower, then these results suggest that it is certainly possible to observe this kind of MRI in the laboratory.

When the bulk of the research for this dissertation was completed, there had still been no such observation, so the experimental application of these ideas were somewhat speculative.

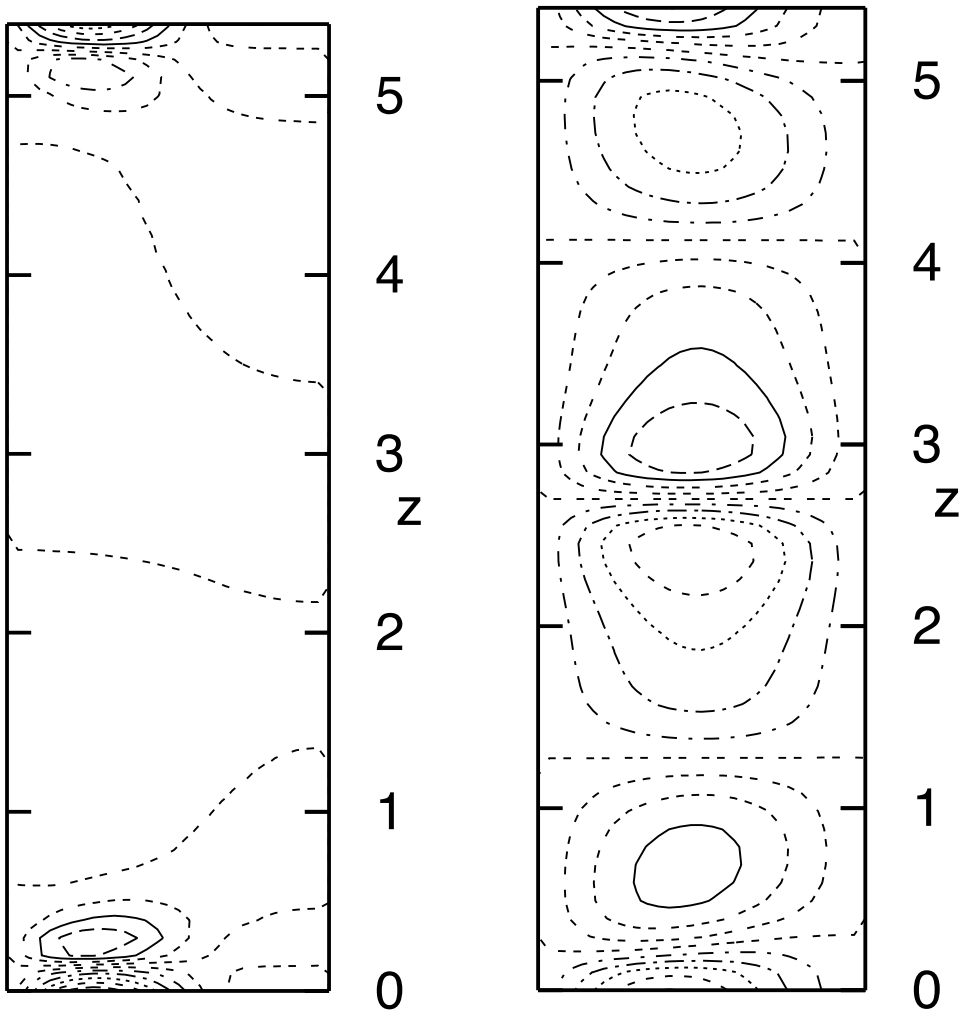

(Run A) (Run B)

Figure 7.20: Contours of B_r at $t = 1000$ in both runs. The saturated magnetic field structures are quite different. Note that in run B, a reverse field configuration has formed at the middle of the apparatus, where below the field is oriented radially inward, and above, radially outward. This saturated state is qualitatively similar to the one found in the previous section.

However, in late 2006, MRI in a Taylor-Couette cylindrical experimental setup involving the flow of a liquid metal Gallium compound showed evidence of MRI with an applied helical magnetic field [10]. This experimental evidence supports the primary conclusions we have presented here, specifically that (1) MRI in the presence of axial and toroidal field components is observable in the laboratory at low Reynolds number ($Re \sim 1800$), (2) Endcaps do not prevent such an

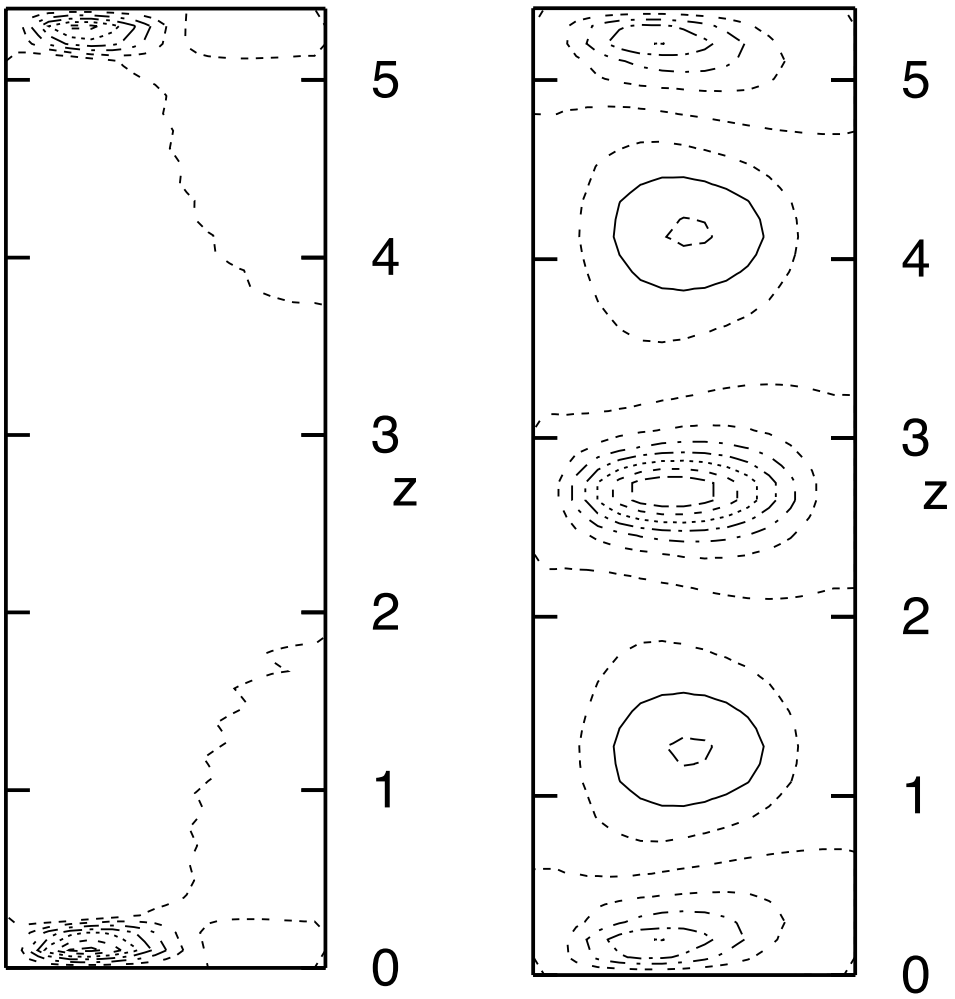

(Run A) (Run B)

Figure 7.21: Contours of V_r at $t = 1000$ in both runs. Note that in Run B, a jet oriented radially outward has formed in the middle of the apparatus.

instability from growing, despite the fact that the MRI waves propagate in the axial direction when a toroidal field is applied, (3) Higher wavelength modes are excitable in the presence of a toroidal field component, (4) angular momentum is transported outward when MRI is excited, and (5) a jet-like radial flow pattern is observed in the saturated state (see figures 7.8 and 7.21).

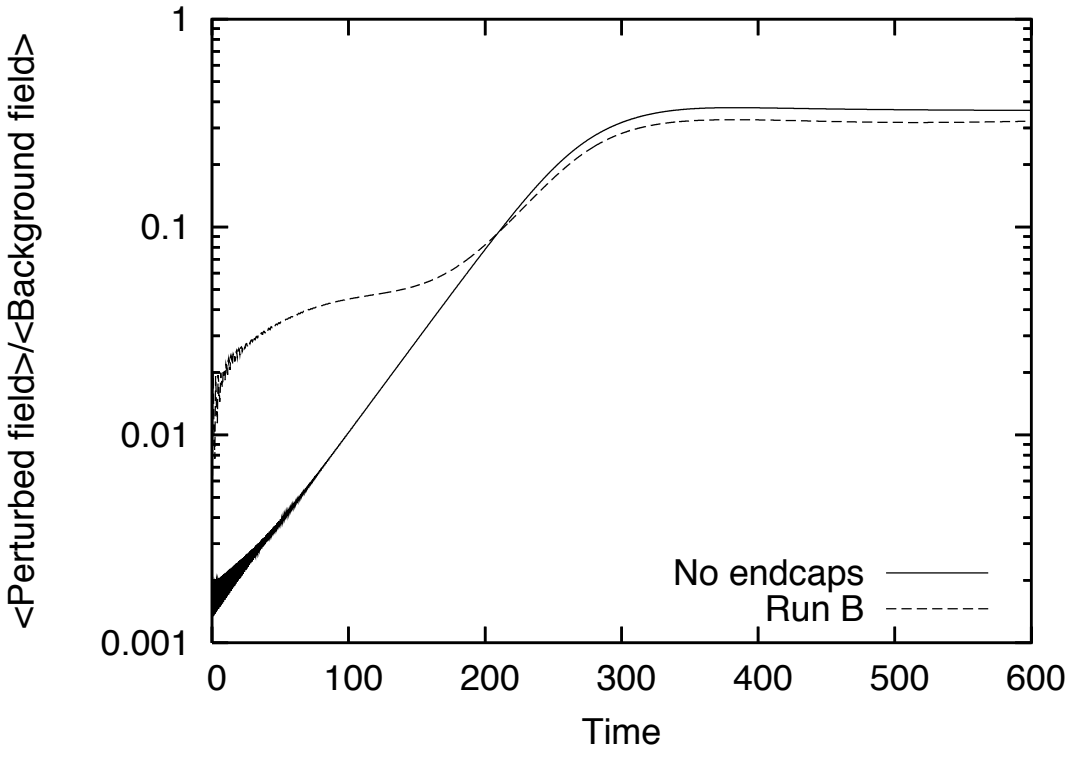

Figure 7.22: $< |\boldsymbol{\delta B}| > /B_z$ vs. time for both Run B and a run with no endcaps, with all of the other parameters held constant.

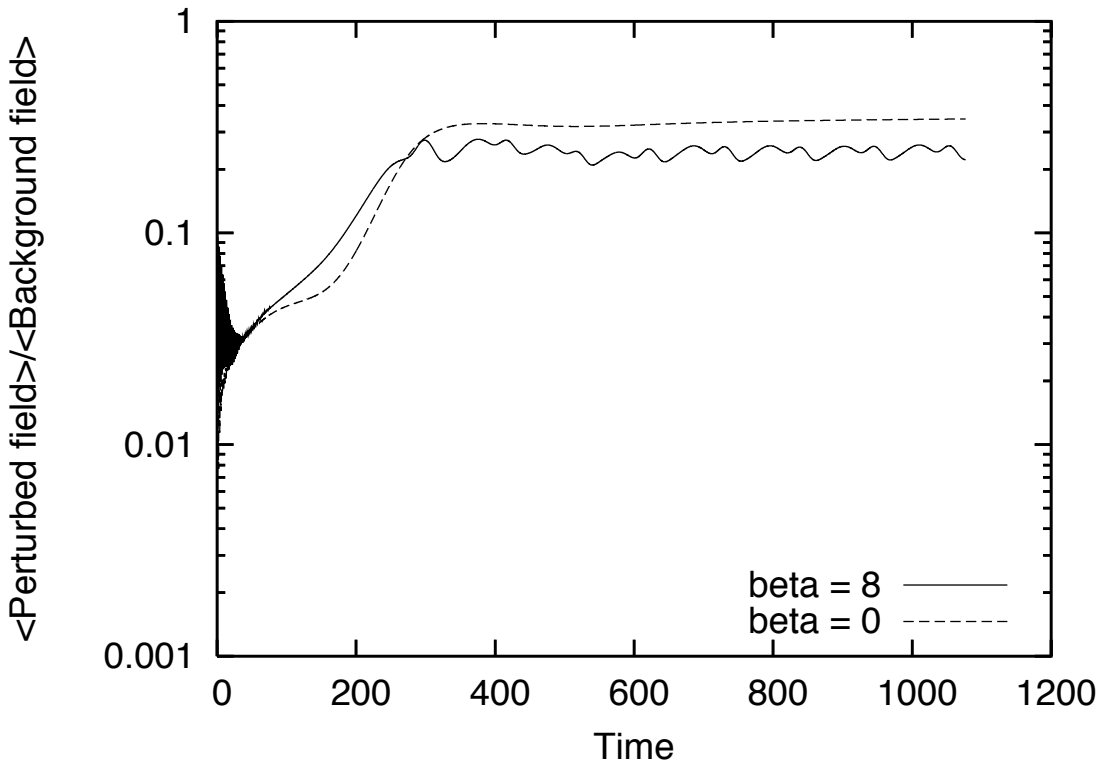

Figure 7.23: $< |\boldsymbol{\delta B}| > /B_z$ vs. time for both Run B and a run with $\beta = 8$, with all of the other parameters held constant.

Chapter 8

Conclusions

In this thesis, we have investigated the magnetorotational instability and its role in the transition to magnetohydrodynamic turbulence in laboratory liquid metal flows. We have developed tools to study the MRI threshold using local linear theory with and without a toroidal magnetic field. We have established that this local linear theory is capable of approximating the transition to magnetic MRI excitations in global simulations and liquid metal experiments. The two global tools we have used, the FD and Spectral codes, have been extensively tested and are available to investigate a range of P_m values. They have been benchmarked, and both reproduce the correct MRI threshold.

Our nonlinear numerical simulations predict the nonlinear saturation amplitude of excited MRI modes for a range of P_m. Our results indicate that in laboratory liquid metal investigations, these magnetic excitations saturate at a low level when compared to the background field strength. The saturation mechanism has been identified as a modification of the differential flow profile, and a portion of this change in rotational energy is given to the magnetic perturbations. The rotational free energy available in a liquid metal experiment is small compared to an accretion flow, and consequently, the saturation mechanism and the saturation amplitude will be very different in these contexts. Our predictions of the saturation amplitude are consistent with the UMD spherical liquid sodium experiment.

Our nonlinear global codes have predicted the characteristics of saturated MRI excitations. These nonlinear results have been benchmarked; the code agreement is excellent in the nonlinear two dimensional regime. We have also used the fully three dimensional FD code to demonstrate that axisymmetric MRI modes may be susceptible to nonaxisymmetric tearing instabilities, suggesting that experimental observations may not be consistent with linear predictions. This achievement helps to explain some of the experimental results that initially appeared inconsistent with the available MRI theory. This characterization of nonlinear MRI physics has opened up a number of

avenues of research that are currently being actively explored.

Finally, our simulations have predicted the phenomenology of MRI near threshold in cylindrical liquid metal experiments. The tools created during this research can be used in designing future experiments to investigate this transition region to magnetic turbulence. Specifically, appropriate parameter ranges can be tested to determine whether the designs of liquid metal experiments will be able to observe the desired phenomena.

Dramatic progress is currently being made in this field, and liquid metal experiments are ideal probes of this transition to magnetic turbulence. Since this transition is connected to the MRI in differentially rotating systems, its role in the development of more complicated magnetic phenomena, such as the spherical dynamo, is an area of active research. Realization of these more strongly driven phenomena are likely to soon be observed in laboratory liquid metal experiments, and the need for numerical simulations to model these flows is critical if the processes are to be unraveled. The interaction of these two communities has been and will continue to be fruitful, and the development of more powerful simulations and better experiments makes this is an exciting time to study MHD turbulence.

Appendix A

Mechanics of the FD and Spectral codes

A.1 FD code

Table A.1 lists all of the available user inputs for the FD code and provides a brief description of each. A sample set of inputs and a description on on how to define them will be discussed in section A.1.3.

Table A.1: `Input Descriptions`

Parameter name	Description	Type
`nrst`	controls the time of a restart	Integer
`nts`	total number of timesteps = nout*nts*mq	Integer
`nout`	2D outputs (`d.lin*`) written nout times	Integer
`n0 - n2`	n0 is the r value for which a z or θ cut is performed	Integer
`nq`	unused	Integer
`mq`	1D outputs written nout*nts times	Integer
`tau`	initial timestep size	Real
`difx`	viscosity = $\frac{\nu t_0}{L}$	Real
`difz`	same as difx	Real
`qpa`	$B_{background}/B_0$	Real
`qpb`	$a\Omega_1/V_{A0}$	Real
`qpc`	unused	Real
`qpd`	amplitude of B field perturbation = qpd*qpa	Real
`qpe - qpq`	free parameters	Real
`beta`	β - magnitude of toroidal background field (Ch. 2)	Real
`mu`	$\mu = \Omega_2/\Omega_1$ (defines Ω_2)	Real
`amp`	amplitude of Veloc. perturbation =amp*qpb	Real
`t0`	baseline temperature	Real
`rset`	if set to 0, time goes to 0 and fields are initialized	Real
`eta`	$1/P_m$ (*ie*, η is normalized to difx or dify)	Real
`kper`	heat conductivity parallel to B	Real
`kpar`	heat conductivity $\perp B$	Real

So, to make physical sense of these parameters, one must select normalizing values of B_0, ρ_0 and L. For example, if one were to choose $B_0 = 1$ T, $L = 10$ cm and $\rho_0 = 0.92$ gm/cm^3, a value of `(12) qpa = 0.00070` implies that a 7 Gauss background field is applied. Since the corresponding Alfvén velocity for such a field would be $V_{A0} = B_0/\sqrt{4\pi\rho_0} \approx 2.05$ cm/s, a selection of `(13) qpb = 0.5` implies that the inner cylinder's velocity is 50 % of V_{A0}, or about 1 cm/s. The rest of the units

can be similarly derived; `(22) t0 = 10` implies that the temperature of the plasma $= 10(\frac{1}{2}\rho_0 V_{A0}^2)$, etc.

A.1.1 Parameter files

Here I will present a section by section breakdown of the code itself. The following files declare parameters, variables, and run preferences: `param,f90, var.f90, vel.f90, def.f90, fread.f90`.

The module `param.f90` defines some basic constants used throughout the problem, such as π. For problem dependent variables included in this parameter file, see Table A.2. The module `param.f90` declares all the field variables to be used (Table A.3). Module `vel.f90` declares the 2D arrays of dimension (`nx`, `nz`) pertaining to the velocity fields (Table A.4). `def.f90` sets a number of flags that control the actions of various elements in the code. `fread.f90` creates the executable, `x.read`, which allows the user to modify the input file, already described.

Table A.2: `param.f90`

Parameter name	Description
`nx`	number of spatial gridpoints in r direction
`ny`	number of spatial gridpoints in θ direction (3D version only)
`nz`	number of spatial gridpoints in z direction
`r0`	r_0 is the radius of the inner cylinder.
`L`	The radius of the outer cylinder is $r_0 + L$.
`elong`	length along z direction
`denmin`	minimum density allowed (for numerical stability)
`gamma`	γ, adiabatic index
`courant`	Standard CFL condition

A.1.2 Main source files

In `prob.f90`, the problem of interest is defined. Fields are initialized (or restarted from a previous run) and boundary conditions are declared on all field variables.

Most of the algorithm's mathematical tools are implemented in `ssub.f90`. These include, but are not limited to, derivatives, integrals, Fourier transforms, noise generators, specific boundary condition implementations, etc.

The main time stepping algorithm is `fb.f90`. This is where the field variables are incre-

Table A.3: `var.f90`

Parameter name	Description
`den, deni`	Density
`pux, puxi`	ρu_r (fluid momentum)
`bbx, bbxi`	Perturbed B_r (this quantity is evolved)
`bbxt, bbxti`	Total B_r - perturbed + background pieces
`bx0`	Background B_r (this quantity is NOT evolved)
`bb2`	Intermediate variable used in `mhd.f90`
`bb3`	Intermediate variable used in `mhd.f90`
`dum`	Intermediate variable used in `mhd.f90`
`tmp, tmpi`	Temperature
`pre, prei`	Pressure
`force`	Source term defined in `source.f90`, used in `mhd.f90`
`flux`	Used in `mhd.f90`
`ex`	Electric field, E_r
`jx`	Current, J_r
`x`†	`x` $= r$ location
`z`†	`z` $= z$ location

† 1-D array with dimension `nx` or `nz`. All other arrays have dimension (`nx`, `nz`).

Table A.4: `vel.f90`

Parameter name	Description
`vx`	`vx` $= v_r$
`xvx`	`xvx` $= r v_r$
`vxmp`	`vxmp(i,k)` $= \lvert v_x(i+1,k) + v_x(i,k)\rvert/2$
`vzmm`	`vzmm(i,k)` $= \lvert v_z(i,k-1) + v_z(i,k)\rvert/2$

mented forward in time, the boundary conditions are imposed, the diagnostics are calculated, and the output files are written. This module interacts heavily with `mhd.f90`, which specifically implements the time stepping algorithm and calculates the nonlinear convections.

A.1.3 Runtime execution, with an example

To access the code, untar the compressed file(s) `2D-FD.tar` (`3D-FD.tar`) to create the FD code MRI simulation folder (to download these files, visit `http://gk.umd.edu/~tillotwa/`). In its current incarnation, the source code files (described in A.1.1 and A.1.2) are located within the `src/` subdirectory. The main directory contains some scripts, gnuplot files (for visualization), some auxiliary files for runtime execution, and a makefile. Compile the code by typing "`make`" on the command line.

After the code is successfully compiled, type "`./x.read`" on the command line. This will bring up a prompt where the user can define all of the input parameters. As an example, match

up your inputs with the ones in Table A.1.3:

(1) nrst= 0	(2) nts = 100	(3) nout= 12
(4) n0 = 10	(5) n1 = 3	(6) n2 = 10
(7) nq = 0	(8) mq = 20	
(9) tau = 0.00272	(10) difx= 0.00070	(11) difz= 0.00070
(12) qpa = 0.20000	(13) qpb = 1.00000	(14) qpc = 0.00000
(15) qpd = 1e-9	(16) qpe = 0.00000	(17) qpf = 0.00000
(18) beta = 0.00000	(19) mu = 0.25000	(20) qpn = 0.00000
(21) amp = 1e-10	(22) t0 = 10.00000	(23) rset= 1.00000
(24) qpp = 0.00000	(25) qpq = 0.00000	(26) eta = 1.00000
(27) kper= 1.00000	(28) kpar= 1.00000	

Table A.5: Note: this input file and the files in the `src/` directory will simulate an MRI unstable system. This particular set of inputs corresponds to the run described in section 7.2, although for the full simulation, the resolution must be increased, `nts` should be changed to at least 300, and the full 3D version must be used.

Now, the code should be ready to run. Type "`./s.r example`" to start the code execution (note that `s.r` is a script which calls multiple executables in series). Unless the source code has been modified, this run should take around 30 seconds to run (exact runtime obviously depends on the compiler, the hardware, etc.). After the code finishes, a new directory should have been created in the main directory, and it should begin with a date/time stamp followed by the word "example." The word "example" could be changed to anything you like simply by changing the argument of the `s.r` script.

Inside this directory (henceforth referred to as the run directory) are all of the output files, a backup of the source directory, a backup of the input files (called `d.nam` and `d.namb`), and a directory containing all of the necessary restart files. The notable output files are `d.fftoutz`, `d.linx`, `d.linz`, `d.stability`, and `d.avg_profile`.

The file `d.fftoutz` should have seven columns. The first is the time, and the second through seventh are amplitudes of the longest 6 vertical wavelength perturbations (the second column is the $k_z L = 0$ component, the third is the $k_z L = 2\pi$ component, etc. If you plot the third through fifth columns vs. time, you should end up with a plot that looks very much like Figure A.1. The number of rows in this file is `nout*nts`.

The files `d.linx` and `d.linz` (and `d.liny` in the 3D version) show linear cuts of all the field variables. In `d.linx`, the cut is along the line (r, `n2`), or (r, `n1`, `n2`) for 3D (`n0`, `n1` and `n2` are

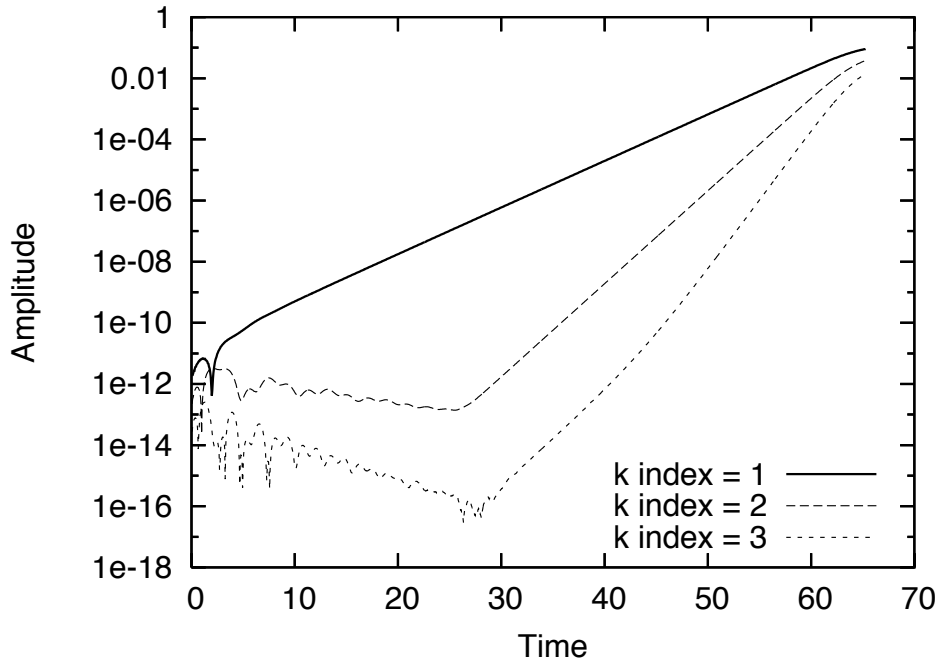

Figure A.1: Plotting the 3rd - 5th columns vs the 1st column in output file `d.fftoutz` after running the FD code using the inputs in Table A.1.3.

fixed values indicating the r, θ or z gridpoint index - they are defined in the input file). Each of these files should contain at least 11 columns (`d.linx` has more). In order of ascending column number, the references are $\rho, \rho u_r, \rho u_\theta, \rho u_z, B_r, B_\theta, B_z, T, P$, the gridpoint index, and r (or θ or z for `d.liny` and `d.linz`). The number of times these cuts are taken is `nout`, and the information is all stored within the same input file. The times of each cut can be found in the `d.times` file.

The output file `d.stability` contains a number of timetraces. In order of increasing column number, they are: time, $< \delta B_r^2 + \delta B_\theta^2 + \delta B_z^2 >, < \delta u_r^2 + \delta u_\theta^2 + \delta u_z^2 >, B_r(11,11), V_r(11,11), \tau_1, \tau_2$, Total E_{mag}, Total $E_{rot}, E_{tot}, < |B_r| >$, and $\sqrt{E_{mag}}$, where τ_1 and τ_2 refer to the total torques at the inner and outer walls. These outputs are by no means set in stone; they can be easily changed by modifying `f.90`. The number of rows in this file is `nout*nts`.

The file `d.avg_profile` shows the averaged V_θ profile `nout` times. The times at which these profiles were taken can be found in the `d.times` file.

Finally, 3D data (cross sections) can be found in the `Visit_files` directory. Since these

files can be large, the number of times they are written is controlled by the `number_of_frames` parameter in `param.f90`. You can also opt not to write them at all, by turning off the movie flag in `def.f90`. Each file contains five columns. They are x_i, x_j, A_r, A_θ, and A_z, where $x_{i,j}$ represents the plane over which the cross section was taken, and $A_{r,\theta,z}$ refer to the 3 vector components. Each file is named according to the following convention: (field variable) + (time of snapshot * 100) + (`.vtk`). In the case of the 3D code, the convention is: (field variable) + (cross section plane - xy, xz, or yz) + (time of snapshot * 100) + (`.vtk`).

A.2 Spectral Code

The Spectral code was developed by Tomo Tatsuno at the University of Maryland. We have only used this algorithm to model magnetized Taylor-Couette flow, so we will restrict our description to this basic usage of the code. A descriptive list of input file parameters for the Spectral code (2 dimensions only) are shown in Table A.6.

After untarring the latest `rmhdsim` archive, all of the source files will be located in a central directory. To compile the code, type "`make rmhd`" on the command line. The result should be a single executable, `rmhd`. To run the simulation, type "`./rmhd` <*filename*>" on the command line, where <*filename*> refers to the input file (*.in) containing all the parameters defined in Table A.6.

After the simulation is complete, the output files conform to the naming convention (input filename) + (resolution) + (file content). For example, the file `mri.100x100.energy.dat` refers to a run with 100^2 gridpoints, and it contains time traces of total energy, magnetic energy, kinetic energy, etc. Line 1 of each output file gives a description of each column's contents.

Figures A.2 and A.3 show the contents of an input file which simulates MRI under the exact same conditions as the example in section A.1.3. Shown in Figure A.4 shows a plot of the lowest 3 vertical wavelength perturbations ($k_z L = 0, 2\pi, 4\pi$). The behavior is comparable to the FD code result shown in Figure A.1, although the amplitudes are different, since instead of transforming B_r to generate the output, the spectral code transforms ψ.

Table A.6: Spectral code input file - `*.in`

Parameter name	Description
`nx`	Number of gridpoints in r direction
`ny`	Number of gridpoints in z direction
`outc1d`	Declares the number of outputs for 1D data
`outc2d`	Declares the number of outputs for 2D data
`vanout1d`	1D animation, in "Vanity" format
`vanout2d`	2D animation, in "Vanity" format
`magneto`	Logical value, if `.true.` magnetic fields evolved
`geometry`	Set '`rz`' for cylindrical (MRI)
`ly`	System height in z direction
`bc_option`	Set '`noslip`' for no-slip velocity boundary conditions
`bc_option_psi`	Set either '`insulator`' or '`ideal'` magnetic boundary conds.
`r_in`	Radius of inner wall
`r_out`	Radius of outer wall
`v_in`	V_θ at inner wall
`v_out`	V_θ at outer wall
`dissipation`	Logical value, if `.false.`, ideal run
`nu`	Viscosity, ν
`eta`	Resistivity, η
`tmax`	Simulation ends at $t =$ `tmax`
`cfl`	Standard CFL condition
`vary_delt`	Logical value, if `.true.`, variable timestep implemented
`delt`	Timestep, or initial timestep if `vary_delt = .true.`
`initial_condition`	Set '`mri`' for initial MRI conditions
`amplitude`	Initial amplitude of perturbation
`noise`	Logical value, if `.true.`, random initialization
`kz_index`	References vertical eigenmode to be amplified
`amplifier`	Amount by which `kz_index` is amplified
`bz`	Axial background field, B_z
`btheta_in`	Toroidal background field at inner wall, $B_\theta(r = r_1)$

```
Input file for rmhd (mri instability)

&grid_points
 nx = 16             ! # of grid points in r
 ny = 16             ! # of grid points in z
/

&output_counts
 outc1d = 500      ! How many times you want to write 1D data
 outc2d = 20         ! How many times                   2D
 vanout1d = .true.   ! 1d animation for vanity (controlled by outc1d)
 vanout2d = .true.  ! 2d                                      outc2d
 finfldout = .false. ! write final field in ascii form
 snap = .false.      ! 2d ascii files for gnuplot (snapshot) governed by outc2d
 hdfout = .false.    ! hdf5 animation data for IDL governed by outc2d
 movie_count = 10
 hdf_pert = .false.

! The followings are for the diagnostics of quasi-linear effect
 qlout = .false.
 qlnorm = .true.     ! normalize it?
! ql_time(1:10) is an integer array
! ql_time(1) = 25
/

!&snap_times
! snap_time(1:10) is a real array
! snap_time(1) = 25.0   ! at what time you want snapshot
!/

&physical_parameters
!! hydrodynamics or magnetohydrodynamics
 magneto = .true.    ! I'm not sure if .false. works in MRI case
/

&simulation_box
 geometry = 'rz'      ! don't change it for MRI
! length in z direction (periodic)
 ly = 1
 bc_option = 'noslip'  ! Other options are available for slab but not for mri
! bc_option_psi = 'insulator'
 bc_option_psi = 'ideal'

 r_in = 0.5           ! radius of inner wall
 r_out = 1.0          ! radius of outer wall
 v_in = 1.0           ! v_theta at inner wall
 v_out = 0.5        ! v_theta at outer wall
/

&dissipation_knobs
 dissipation = .true.  ! make .false. for ideal run
 nu  = 7e-4         ! viscousity
 eta = 7e-4           ! resistivity
/

&tint_knobs
 tmax = 150         ! simulation ends at this normalized time
```

Figure A.2: Sample spectral code input file, page 1.

```
 cfl = 0.1           ! time step restriction as a ratio to CFL condition

 vary_delt = .true. ! I want to make it work, as a first upgrade
! delt = 2.e-3
 delt = 1.e-2        ! delta t (time step)
/

&initial
 initial_condition = 'mri'  ! initial condition: defined in init_cond_defs.f90
 amplitude = 1.e-13       ! initial amplitude of perturbation
 noise = .true.         ! Not sure if this works
 projection = .true.     ! need to be true
 kz_index = 2
 amplifier = 1

!! for mri
 bz = 0.2            ! homogeneous axial field Bz
 btheta_in = 0     ! 1/r toroidal field
! btheta_out = 0.0
/

&source_terms
 andy_alpha = 0.0   ! source a la Andy
/

&computational_flags
 twothirds = .true.      ! true if you use 2/3 rule
 fftw = .true.           ! true if you use FFTW (otherwise Numerical Recipes)
 fftw_measure = .false.  ! may affect on FFT speed
 FC_complex = .true.     ! must be true for MRI runs
 arcII = .false.         ! may affect on speed at arcII
 precond = .true.        ! has to be true at all times
/
```

Figure A.3: Sample spectral code input file, page 2.

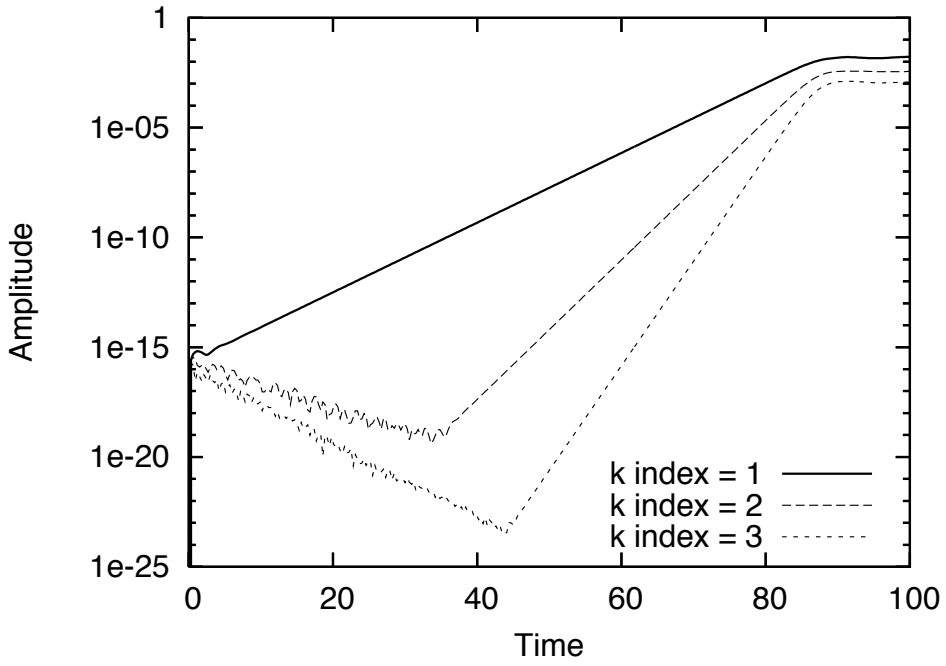

Figure A.4: The lowest 3 vertical wavelength perturbation amplitudes vs time as calculated by the spectral code. Note the qualitative agreement with Figure A.1. The input parameters were the same.

Appendix B

Nonaxisymmetric DR Equations

In Chapter 2, we derived the linear equations corresponding to the evolution of perturbations under the influence of equations 2.1 and 2.2 in cylindrical curvilinear coordinates (r, θ, z). We assumed axisymmetry - $\partial_\theta \propto m = 0$. We will derive the same set of equations in this section allowing for finite m, but disallowing the presence of a toroidal background magnetic field ($\beta = 0$). As before, the background magnetic field is purely axial, and the background velocity field is purely azimuthal with an as yet undetermined radial structure, $\Omega(r)$:

$$\mathbf{B} = B_0 \mathbf{e}_z + \delta\mathbf{B}, \quad \mathbf{v} = r\Omega(r)\mathbf{e}_\theta + \delta\mathbf{v} \tag{B.1}$$

We assume the following structural dependence of the perturbations:

$$\delta V_{Ar} = \beta_r(r) e^{im\theta} \cos(kz) e^{\gamma t}, \quad \delta v_r = \varphi_r(r) e^{im\theta} \sin(kz) e^{\gamma t} \tag{B.2}$$

$$\delta V_{A\theta} = \beta_\theta(r) e^{im\theta} \cos(kz) e^{\gamma t}, \quad \delta v_\theta = \varphi_\theta(r) e^{im\theta} \sin(kz) e^{\gamma t} \tag{B.3}$$

$$\delta V_{Az} = \beta_z(r) e^{im\theta} \sin(kz) e^{\gamma t}, \quad \delta v_r = \varphi_z(r) e^{im\theta} \cos(kz) e^{\gamma t} \tag{B.4}$$

Applying these perturbations to equations 2.1 and 2.2, and eliminating pressure via the divergence free conditions, we derive, after a great deal of algebra, the linearized equations for $\beta_r, \beta_\theta, \varphi_r$ and

φ_θ:

$$\widehat{\gamma}\beta_r - \omega_A\phi_r = \eta[\nabla^2 - \frac{1}{r^2}(1+2im)]\beta_r \tag{B.5}$$

$$\widehat{\gamma}\beta_\theta - \beta_r(r\Omega') - \omega_A\phi_\theta = \eta[\nabla^2 - \frac{1}{r^2}(1-2im)]\beta_\theta \tag{B.6}$$

$$\begin{aligned}
&\Big\{\widehat{\gamma}(1-\frac{1}{k^2}\partial_r\partial_r^\dagger) - \frac{im\Omega'}{k^2}\partial_r^\dagger + \frac{\nu}{k^2}\partial_r\nabla^2\partial_r^\dagger\Big\}\phi_r + \\
&\quad\Big\{-\frac{im\widehat{\gamma}}{k^2}\partial_r\frac{1}{r} + \frac{\Omega' m^2}{k^2}\frac{1}{r} + \frac{\nu im}{k^2}\partial_r\nabla^2\frac{1}{r} - 2\Omega\Big\}\phi_\theta - \\
&\quad\omega_A\Big\{\frac{1}{k^2}\partial_r\partial_r^\dagger - 1\Big\}\beta_r - \omega_A\Big\{\frac{im}{k^2}\partial_r\frac{1}{r}\Big\}\beta_\theta = \nu[\nabla^2 - \frac{1}{r^2}(1+2im)]\phi_r
\end{aligned} \tag{B.7}$$

$$\begin{aligned}
&\Big\{\widehat{\gamma}(1+\frac{m^2}{r^2k^2}) - \frac{\nu m^2}{rk^2}\nabla^2\frac{1}{r}\Big\}\phi_\theta + \Big\{-\frac{im\widehat{\gamma}}{rk^2}\partial_r^\dagger + \frac{\nu im}{rk^2}\nabla^2\partial_r^\dagger + [\partial_r^\dagger(r\Omega)]\Big\}\phi_r - \\
&\quad\Big\{\frac{\omega_A im}{rk^2}\partial_r^\dagger\Big\}\beta_r + \omega_A\Big\{\frac{m^2}{r^2k^2} + 1\Big\}\beta_\theta = \nu[\nabla^2 - \frac{1}{r^2}(1-2im)]\phi_\theta
\end{aligned} \tag{B.8}$$

where $\widehat{\gamma} = \gamma + im\Omega$ ($m\Omega$ is an oscillatory component of the frequency coming from the convective portion of the total time derivative).

Appendix C

Angular Momentum

C.1 Derivation of Angular Momentum Equation

For completeness, we derive the equation describing the evolution of the z component of the angular momentum for a conventional incompressible MHD system in cylindrical coordinates, beginning from the equations that are actually solved in the FD simulation code. These equations are:

$$\frac{\partial \rho}{\partial t} + \nabla \cdot (\rho \mathbf{u}) = 0 \tag{C.1}$$

$$\rho \frac{\partial \mathbf{u}}{\partial t} + \rho \mathbf{u} \cdot \nabla \mathbf{u} + \nabla P = \frac{1}{\mu_0} \nabla \times \mathbf{B} \times \mathbf{B} + \rho \nu \nabla^2 \mathbf{u} \tag{C.2}$$

We may use the identity

$$\nabla \times \mathbf{B} \times \mathbf{B} = \mathbf{B} \cdot \nabla \mathbf{B} - \frac{1}{2} \nabla B^2.$$

to rewrite Eq. (C.1) as

$$\rho \frac{\partial \mathbf{u}}{\partial t} + \rho \mathbf{u} \cdot \nabla \mathbf{u} + \nabla \left(P + \frac{B^2}{2\mu_0} \right) = \frac{1}{\mu_0} \mathbf{B} \cdot \nabla \mathbf{B} + \rho \nu \nabla^2 \mathbf{u} \tag{C.3}$$

The most direct derivation of the radial flux of the z-component of the angular momentum is to multiply Eq. (C.1) by $\mathbf{u}$ and to add the result to Eq. (C.3), yielding

$$\frac{\partial \rho \mathbf{u}}{\partial t} + \nabla \cdot \rho \mathbf{u} \mathbf{u} + \nabla \left(P + \frac{B^2}{2\mu_0} \right) = \frac{1}{\mu_0} \mathbf{B} \cdot \nabla \mathbf{B} + \rho \nu \nabla^2 \mathbf{u}. \tag{C.4}$$

Here, we have used the identity

$$\nabla \cdot (\mathbf{A}\mathbf{B}) = (\nabla \cdot \mathbf{A})\mathbf{B} + (\mathbf{A} \cdot \nabla)\mathbf{B}$$

for any two vectors $\mathbf{A}$ and $\mathbf{B}$. Note that one may use the fact that $\nabla \cdot \mathbf{B} = 0$ to write

$$\mathbf{B} \cdot \nabla \mathbf{B} = \nabla \cdot \mathbf{B}\mathbf{B}.$$

With this identity, Eq. (C.4) can be written as

$$\frac{\partial \rho \mathbf{u}}{\partial t} + \nabla \cdot \rho \mathbf{u}\mathbf{u} + \nabla \left(P + \frac{B^2}{2\mu_0} \right) = \frac{1}{\mu_0} \nabla \cdot \mathbf{B}\mathbf{B} + \rho \nu \nabla^2 \mathbf{u}. \tag{C.5}$$

Operate on Eq. (C.5) with $(\hat{\mathbf{z}} \cdot \mathbf{r}\times)$ to find

$$\frac{\partial}{\partial t} r \rho u_\theta + r \left[\frac{1}{r} \frac{\partial}{\partial r} (r \rho u_r u_\theta) + \frac{1}{r} \frac{\partial}{\partial \theta} \rho u_\theta u_\theta + \frac{\partial}{\partial z} \rho u_z u_\theta + \frac{\rho u_\theta u_r}{r} \right] + \frac{\partial}{\partial \theta} \left(P + \frac{B^2}{2\mu_0} \right) =$$

$$\frac{r}{\mu_0} \left[\frac{1}{r} \frac{\partial}{\partial r} (r B_r B_\theta) + \frac{1}{r} \frac{\partial}{\partial \theta} B_\theta B_\theta + \frac{\partial}{\partial z} B_z B_\theta + \frac{B_\theta B_r}{r} \right] + r \rho \nu \left(\nabla^2 \mathbf{u} \right)_\theta . \tag{C.6}$$

It is straightforward to verify that

$$\nabla \cdot (r \rho u_\theta \mathbf{u}) = 2 \rho u_\theta u_r + r \frac{\partial}{\partial r} \rho u_\theta u_r + \frac{\partial}{\partial \theta} \rho u_\theta u_\theta + \frac{\partial}{\partial z} r \rho u_\theta u_z$$

and use this result to simplify Eq. (C.6),

$$\frac{\partial}{\partial t} r \rho u_\theta + \nabla \cdot (r \rho u_\theta \mathbf{u}) + \frac{\partial}{\partial \theta} \left(P + \frac{B^2}{2\mu_0} \right) = \frac{1}{\mu_0} \nabla \cdot (r B_\theta \mathbf{B}) + r \rho \nu \left(\nabla^2 \mathbf{u} \right)_\theta . \tag{C.7}$$

Upon recognizing one further identity (which also follows from the identification of the generalized pressure tensor), namely

$$\nabla \cdot \left[r \left(P + \frac{B^2}{2\mu_0} \right) \hat{\theta} \right] = \frac{\partial}{\partial \theta} \left(P + \frac{B^2}{2\mu_0} \right)$$

the viscous form of Eq. (5.10) follows. For completeness, this equation reads

$$\frac{\partial}{\partial t} r \rho u_\theta + \nabla \cdot \left\{ r \left[\rho u_\theta \mathbf{u} - \frac{1}{\mu_0} B_\theta \mathbf{B} + \left(P + \frac{B^2}{2\mu_0} \right) \hat{\theta} \right] \right\} = r \rho \nu \left(\nabla^2 \mathbf{u} \right)_\theta . \tag{C.8}$$

The quantity in curly brackets can be recognized as the inviscid flux of the z component of the angular momentum. The radial component of this flux is

$$\Gamma_r = r\left[\rho u_\theta u_r - \frac{1}{\mu_0} B_\theta B_r\right].$$

C.2 Viscous flux of angular momentum

The right hand side of Eq. (C.8) describes the effect of viscosity on the z component of the angular momentum in an incompressible plasma described by magnetohydrodynamics. The viscous flux of angular momentum is generally non-negligible in laboratory experiments, particularly near the walls. One must understand the effect of viscosity to understand the Couette flow equilibrium. For completeness, we review a few basic features of the viscous flux. No new results are presented in this section. Our treatment applies equally to fluid or MHD systems.

When the viscosity is high, Eq. (C.8) reduces to

$$\frac{\partial}{\partial t} r\rho u_\theta = r\rho\nu \left(\nabla^2 \mathbf{u}\right)_\theta .$$

Upon expanding the right hand side in cylindrical coordinates, one finds

$$\frac{\partial}{\partial t} r\rho u_\theta = \rho\nu \left[r u_\theta'' + u_\theta' - \frac{u_\theta}{r} + \frac{1}{r}\frac{\partial^2 u_\theta}{\partial \theta^2} + r\frac{\partial^2 u_\theta}{\partial z^2} + \frac{2}{r}\frac{\partial u_r}{\partial \theta}\right] \tag{C.9}$$

where primes denote derivatives with respect to radius.

Steady-state, axisymmetric solutions with constant ν and $u_\theta = u_\theta(r)$ satisfy

$$r u_\theta'' + u_\theta' - \frac{u_\theta}{r} = 0, \tag{C.10}$$

the solution of which is the Couette flow

$$u_\theta = ar + \frac{b}{r}. \tag{C.11}$$

Since $u_\theta(r) = r\Omega(r)$, one may also write this solution as

$$\Omega = a + \frac{b}{r^2}. \tag{C.12}$$

The z component of the angular momentum is described by

$$\frac{\partial L_z}{\partial t} + \nabla \cdot \mathbf{\Gamma} = 0$$

in the viscous limit. In steady state, $\nabla \cdot \mathbf{\Gamma} = 0$. In cylindrical coordinates, this reads

$$\nabla \cdot \mathbf{\Gamma} = \frac{1}{r}\frac{\partial}{\partial r}\left(r\Gamma_r\right) + \frac{1}{r}\frac{\partial \Gamma_\theta}{\partial \theta} + \frac{\partial \Gamma_z}{\partial z} = -\rho\nu\left(\nabla^2 \mathbf{u}\right)_\theta.$$

For Couette flow, the radial component of the flux satisfies

$$-\frac{1}{r\rho\nu}\frac{\partial}{\partial r}\left(r\Gamma_r\right) = ru_\theta'' + u_\theta' - \frac{u_\theta}{r}, \tag{C.13}$$

so that the radial component of the viscous flux can be identified as

$$\Gamma_r = -\rho\nu r^2 \frac{\partial}{\partial r}\frac{u_\theta}{r} = -\rho\nu r^2 \Omega'(r). \tag{C.14}$$

This flux is not constant with radius, as can be seen by substituting the expression for $\Omega(r)$ from Eq. (C.12),

$$\Gamma_r = \frac{2b\rho\nu}{r}.$$

This result was already clear from Eq. (C.13), since the requirement that $\partial(r\Gamma_r)/\partial r = 0$ in steady state implies $\Gamma_r \propto 1/r$. Although all of these equations are consistent with the literature (See, *e.g.,* [1, 34]) our interpretation differs slightly from the interpretation offered in [34].

BIBLIOGRAPHY

[1] S. A. Balbus and J. F. Hawley, Reviews of Modern Physics **70**, 1 (1998).

[2] N. I. Shakura and R. A. Sunyaev, A & A **24** (1973).

[3] E. Velikhov, Sov. Phys. JETP **36**, 995998 (1959).

[4] S. Chandrasekhar, Proceedings of the National Academy of Sciences **46** (1960).

[5] A. Schekoshihin, ApJ **612** (2004).

[6] H. Goldstein, *Classical Mechanics*, 2 ed. (Addison-Wesley, 1980).

[7] J. Goodman and H. Ji, J. Fluid Mech. **462**, 365 (2002).

[8] H. Ji *et al.*, AIP Conference Proceedings (2004).

[9] D. R. Sisan *et al.*, Phys. Rev. Letters **93** (2004).

[10] F. Stefani *et al.*, Phys. Rev. Lett. **97** (2006).

[11] K. Noguchi *et al.*, APS 44th DPP (2002).

[12] R. Hollerbach and G. Rüdiger, Phys. Rev. Lett. 95 **95** (2005).

[13] D. Richard and J. Zahn, Astronomy & Astrophysics comments (1999).

[14] R. Hollerbach and A. Fournier, AIP Conf Proc **733**, 114 (2004).

[15] R. Fitzpatrick, Introduction to plasma physics.

[16] P. Sharma, Ap. J. **596**, 1121 (2003).

[17] E. Koschmeider, *Benard cells and Taylor Vortices* (Cambridge Monographs on Mechanics and Applied Mathematics, 1993).

[18] P. Gudzar, D. Drake, D. McCarthy, A. Hassam, and C. Liu, Phys. Fluids B **5**, 3712 (1993).

[19] M. Frigo and S. Johnson, Proceedings of the 1998 IEEE International Conference **3**, 1381 (1998).

[20] J. P. Boyd, *Chebyshev and Fourier Spectral Methods*, 2 ed. (Dover Publications, Inc., 2000).

[21] A. Youd, Taylor–couette flow.

[22] J. Lighthill, *An Informal Introduction to Theoretical Fluid Dynamics* (Oxford University Press, 1988).

[23] P. Snyder, G. Hammett, and W. Dorland, Phys. Plasmas **4**, 3974 (1997).

[24] W. Dobler, MHD Couette Flows, of AIP Conference Proceedings **733**, 142 (2004).

[25] I. Herron and F. Soliman, Applied Mathematics Letters **19**, 1113 (2006).

[26] D. Shalybkov, G. Rüdiger, and M. Schultz, Astronomy and Astrophysics **395**, 339 (2002).

[27] L. Kitchatinov and G. Rüdiger, Mon. Not. R. Astron. Soc. **286**, 757 (1997).

[28] E. Bullard and H. Gellman, Philosophical Transactions of the Royal Society of London. Series A, Mathematical and Physical Sciences **247**, 213 (1954).

[29] H. K. Moffatt, *Magnetic field generation in electrically conducting fluids* (Cambridge, England, Cambridge University Press, 1978).

[30] R. Gatto, P. Terry, and C. Hegna, Nucl. Fusion **42**, 496 (2002).

[31] R. B. White, Rev. Mod. Phys. **58**, 183 (1986).

[32] G. J. Liu, W. and H. Ji, ApJ **643**, 306 (2006).

[33] H. Ji, M. J. Burin, E. Schartman, and J. Goodman, Nature **444** (2006).

[34] H. Ji, J. Goodman, and A. Kageyama, Mon. Not. R. Astron. Soc. **325**, L1 (2001).